Energy Advances

Accepted Manuscript

This article can be cited before page numbers have been issued, to do this please use: A. Mukherjee, M. Abdinejad, S. Sinha Mahapatra and B. C. Ruidas, *Energy Adv.*, 2024, DOI: 10.1039/D4YA00302K.

ROYAL SOCIETY OF CHEMISTRY

rsc.li/energy-advances

View Article Online
DOI: 10.1039/D4EY00302K

Controlled Synthesis of Copper Sulfide-associated Catalysts for Electrochemical Reduction of CO_2 to Formic Acid and Beyond: A Review

Received 00th January 20xx,
Accepted 00th January 20xx

DOI: 10.1039/x0xx00000x

Anirban Mukherjee,[a] Maryam Abdinejad,*[b] Susanta Sinha Mahapatra,[c] and Bidhan Chandra Ruidas*[a]

Converting carbon dioxide (CO_2) into value-added chemicals is considered as a promising strategy to mitigate climate change. Among the various CO_2 reduction techniques, electrochemical CO_2 reduction ($ERCO_2$) using renewable energy sources holds significant potential. Consequently, the design and development of electrocatalysts capable of offering both high performance and cost-effectiveness hold the potential to expedite reaction kinetics and facilitate widespread industrial adoption. In recent years, abundant copper sulfide (Cu/S)-associated nanomaterials among various metal-chalcogenides have been of extensive research interest due to their semiconductor and low toxicity properties, enabling them to be used in widespread applications of the $ERCO_2$ field. This review highlights the progress of engineered Cu/S-associated nanomaterials for $ERCO_2$ reactions and elaborates on the correlations of engineering strategies, catalytic activity, and reaction pathways. The paper also summarises the controllable synthesis methods for fabricating various state-of-the-art Cu/S-associated structures and outlines their possible implementation for CO_2 reduction as an electrocatalyst. Finally, challenges and prospects are presented for the future development and practical application of Cu/S-associated catalysts for ECO_2R to value-added chemicals.

1. Introduction

Since industrialization, the utilization of non-renewable energy, which encompasses fossil fuels, i.e., coal, crude oil, and natural gas, has tremendously increased[1]. Fossil fuels, as non-renewable energy sources, have two vulnerabilities: (1) limited supplies cannot meet increasing demands for energy, resulting in a severe energy crisis, and (2) the consumption of fossil fuels for energy generation releases a substantial amount of CO_2 into the earth's atmosphere, contributing to global ecological issues such as global warming, global sea levels rising, land degradation, and many more.[1–3] With the intention of achieving a sustainable future, reducing CO_2 concentrations in the atmosphere is crucial[4]. In this context, the scientific community has made numerous efforts to reach this goal by incorporating the CO_2 capture, utilization, and storage (CCUS) approach, as depicted in Fig. 1.[5,6] The conversion of CO_2 into C_1 and highly dense C_2 products through chemical routes has been considered a promising technology for reutilizing CO_2.[7,8] It can be achieved by several methods, such as photochemical,[9] electrochemical,[10,11] photo-electrochemical,[12] and biochemical.[13] Among those, the electrochemical reduction of CO_2 ($ERCO_2$) has gained a lot of attention owing to its (a) Controllable process parameters (i.e., potential and temperature), (b) feasibility with reaction environment (e.g., organic and aqueous electrolyte), and (c) ability to scale up.[14,15] Additionally, $ERCO_2$ can be conducted using renewable energy resources such as solar and wind as power sources, allowing for renewable energy storage and redistribution [16]. Therefore, $ERCO_2$ has emerged as a significant research area with an industrial prospect, and in the recent past, much progress has been made in this prospering domain [17,18].

As reported in the scholarly literature and with the progress of research outcomes, the $ERCO_2$ catalysts are classified into metal and metal-free catalysts associated with design, synthesis, and product selectivity.[19] Nonmetal electrocatalysts are mostly made of carbon-associated nanoparticles.[20] On the other hand, metal electrocatalysts include bare metal and their hybrid complexes, such as metal alloys,[19,21,22] metal oxides,[23,24] metal sulfides,[25] and metal complexes[26,27]. The activity and selectivity of the $ERCO_2$ vary with different metal catalysts owing to variations in the activity and adsorption strength of the intermediates.[28] Thus, metal catalysts are further classified into four categories associated with their selectivity for final products: a) Cd, Hg, Tl, Sn, In, Bi, and Pb: produce HCOO- intermediate, resulting in formate as their primary product;[29–34] b) Au, Ag, Zn, and Pd: produce CO as their main reduction product because of the weak CO adsorption capacity;[35–42] and, c) Ni, Fe, Si, V, Pt: produce H_2 owing to the low HER potential;[43–47] d) Cu produces up to sixteen carbon-associated nanomaterials, comprising several highly energy-dense multi–carbon products under different conditions.[48,49] Hori et al.[50] conducted $ERCO_2$ in 0.5 M $KHCO_3$ at 5mA/cm^2 for an hour on various polycrystalline metal electrodes. The outcomes showed that each metal electrode needs a significant overpotential to reach a particular current density (in this case, 5mA/cm^2). Au requires the lowest overpotential (-0.6 V_{RHE}) to obtain CO (87%), but Pb needs the highest overpotential (-1.1V_{RHE}) to produce formate (97%).[50]

Although significant progress has been achieved, some hindrances still exist with the industrial aspects of $ERCO_2$,[51,52] such as (1) high overpotential for $ERCO_2$ as CO_2 is a linear molecule that is thermodynamically stable and

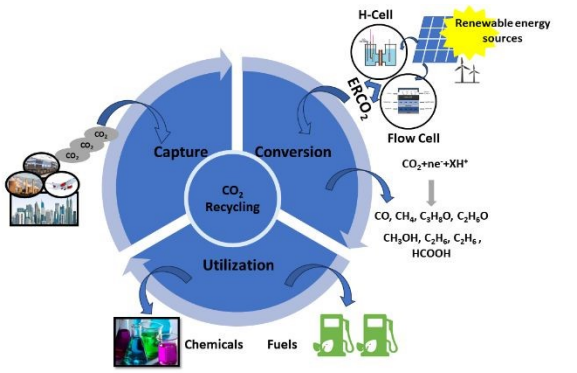

Fig. 1. A graphic illustration of CO_2 capture, utilization, and storage (CCUS).

[a] Department of Chemical Engineering, Birla Institute of Technology, Mesra, Ranchi 835215, India.
[b] Department of Chemical Engineering, Massachusetts Institute of Technology, 77 Massachusetts Avenue, Cambridge, Massachusetts 02139, United States
[c] Department of Chemistry, Birla Institute of Technology, Mesra, Ranchi 835215, India.

chemically inert;[53] (2) sluggish kinetics of CO_2 electro reduction because the complex proton-coupled electron transfer (PCET) steps and kinetics of electron transfer were slowed by the insolubility of CO_2 in the aqueous medium.;[54] (3) low exchange current densities, a majority of CO_2 electrocatalysts reported thus far operate at less than 20 mA/cm^2; however, this is significantly less than the commercial electrolyzers, which generally operate at over 70% efficiency at current densities exceeding 200 mA/cm^2;[55] (4) unsatisfactory selectivity, suggesting expensive separation procedures;[56] (5) catalyst deactivation in less than 100 hr, limiting practical application and industrialization of technology;[57] and (6) competitive hydrogen evolution reaction (HER); the HER surpasses the $ERCO_2$ due to its energy favourable conditions at higher overpotentials, leading in a higher FE_{H2} (Faradaic Efficiency) at the sacrifice for selective $ERCO_2$ products.[58] Recently, much research has concentrated on designing and synthesizing innovative, cost-effective, and robust electrocatalysts that can counter those bottlenecks and reduce CO_2 at high rates with minimal overpotential.[57,58]

As pointed out in an earlier paragraph, Cu can electrochemically reduce CO_2 to highly energy-dense C_{2+} products, which has gained massive attention.[59] However, the critical path of the C-C coupling process required for the C_{2+} product formation introduces a high activation energy barrier, resulting in low activity and poor selectivity.[60,61] In this context, synthesizing Cu-associated electrocatalysts is crucial for overcoming the energy barrier in $ERCO_2$. Researchers exhibited that the CO_2 electroreduction performance (i.e., activity and selectivity) of Cu catalysts is affected by multiple factors. For example, in their work, Hori et al.[62,63] exhibited that Cu with several crystal facets could yield various $ERCO_2$ products. The Cu (111) surface produces methane as a primary product, while C_2 products such as ethylene and ethanol are made over Cu(100) surfaces. Rcskc and colleagues[64] also exhibited that faradaic efficiency and current density of Cu nanoparticles were significant compared to bulk Cu, while Chen et al.[65] demonstrated that the single-atom Cu observed better $ERCO_2$ performance than other reported Cu-associated materials, i.e., bulk metal Cu.

Moreover, using bimetallic Cu-associated electrocatalysts has shown promise in enhancing copper's selectivity and overall catalytic performance. For example, Burdyny's group[58] could electrochemically reduce CO_2 to formate as the primary product using bimetallic Cu-Pd with the Faradaic efficiencies of 93% and a current density of 150 mA/cm^2 at a cell potential of -2.9 V_{RHE} using a zero-gap flow cell, also known as Membrane electrode Assembly cell. They successfully demonstrated how the engineering design of an electrochemical cell, coupled with catalyst structure, achieves the highest overall reported energy efficiency (EE) for formate production at 47%. These efficiencies show the benefit of using non-post-transition metals as a primary strategy for formate production. Another study shows that catalyst morphology is also essential: Chorkendorff et al. [66] found that metallic Cu with varying surface roughness exhibits distinct selective $ERCO_2$ product formation. They discovered that the Cu nanoparticle-coated electrocatalysts have improved hydrocarbon selectivity compared to non-coated electrocatalysts. Motivated by the afore-work, several research groups synthesized different morphologies, such as nanowires,[67,68] films,[69] microcubes,[70,71] core-shell,[72,73], and Cu–associated bimetallic[58] catalysts and studied the catalytic activity during $ERCO_2$. The research showed that the catalytic activity of Cu-associated catalysts towards $ERCO_2$ can be remarkably enhanced by co-relating the catalysts' structure and morphology.

In recent years, Cu/S-associated nanomaterials have gained significant attention as electrocatalysts due to their p-type semiconducting, earth-abundance and nontoxic characteristics. Various phases of copper sulfide are reported in the literature, namely chalcocite (Cu_2S), djurleite ($Cu_{1.97}S$), digenite ($Cu_{1.80}S$), anilite ($Cu_{1.75}S$), geerite ($Cu_{1.60}S$), spionkopite ($Cu_{1.40}S$), yarrowite ($Cu_{1.12}S$) and covellite ($Cu_{1.00}S$) as copper-Figrich systems, while Villamanite (CuS_2) as sulfur-rich system and covellite (CuS) as 1/1 system, regularly denoted as $Cu_{2-x}S$ having minimal values of x [74–77]. Based on their packing of sulfur atoms in the lattice, the afore-crystal structures have been grouped into three categories, as illustrated in Fig. 2, specifically cubic close packing (anilite and digenite), close hexagonal packing (djurleite and chalcocite), and a combination of close hexagonal packing and covalent bonding of the sulfur atoms (covelline)[77]. But the remaining forms, i.e., yarrowite, spionkopite, geerite, and crystal structures, remain unknown. It is to be noted that copper sulfides' electrical conductivity depends on their phases, decreasing from copper-deficient to copper-rich [78,79]. For example, it has been observed that at 1.63K, the naturally occurring covellite phase of CuS exhibits exceptional electrical conductivity [80]. Therefore, owing to their broad, versatile properties, copper sulfides are fascinating nanomaterials for various applications, i.e., optoelectronic devices[81], photocatalysis[82], photovoltaic cells[83], sensors[84], battery electrodes[85], and the biomedical field[86]. Thus, numerous studies have focused on the engineering strategies of these materials for modifying properties, including the electronic modulation effects structure for $ERCO_2$. Notably, developing $ERCO_2$ catalytic systems that can overcome bottlenecks is becoming an essential topic with the increasing use of this electrocatalytic technology. According to the reported literature, a variety of physical[87] as well as chemical[75] methods, such as hydro and solvothermal[88,89], ball-milling[90], electrodeposition[91], microwave irradiation[92], thermolysis[93], or template-assisted[94,95] approaches, have been widely used in constructing different nano-dimensional (i.e., Zero-dimensional, One-dimensional, two-dimensional, and three-dimensional) Cu/S-associated nanomaterials. So far, several synthetic processes have yielded various shapes of Cu/S-associated nanostructures, such as nanoparticles, nanoplates, hollow spheres, nanorods, nanowires, nanotubes, nanosheets, etc. Therefore, research has focused on fabricating unique electrocatalysts with diversified nanostructures due to their strong connections and unique properties.

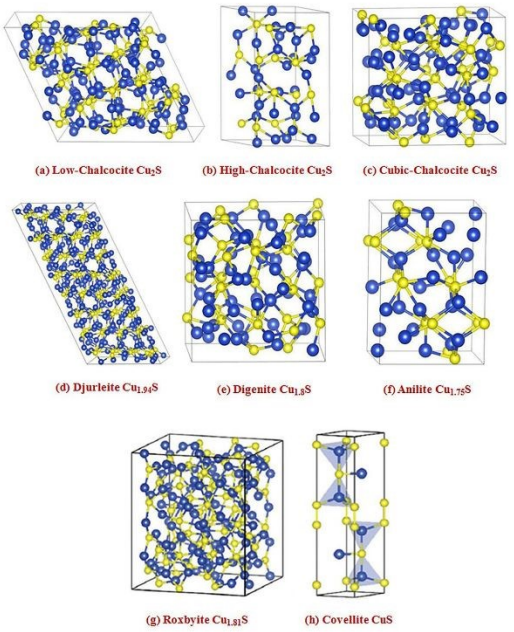

Fig 2. Crystal structures of some representative copper sulfide phases. (Blue spheres - copper atoms and yellow spheres – sulfur atoms, surrounded by black lines showing each

unit cell boundary. (Reproduced on permission (a-f). 95. copyright American Institute of Physics 2012) and (g-h) (Reproduced on permission from 77. Copyright, RSC 2019).

Until recently, many outstanding review articles on Cu/S-associated nanomaterials for several energy applications have been published,[74,79,96] including the preparation, characterization methods, and the effects of modification strategies on catalytic activity. However, an in-depth and systematic investigation of Cu/S-associated electrocatalysts' synthesis strategies and electron modulation effects for $ERCO_2$ is lacking and desired. This review summarizes the most recent advancements in Cu/S-associated catalysts for $ERCO_2$ reactions and outlines the connection between catalytic efficiency and several engineering approaches. The primary section discusses various modification strategies for Cu/S-associated nanomaterials. After that, the effects of these strategies on electron modulation will be summarized. This fundamental understanding can help with the design of high-efficiency $ERCO_2$ catalysts. Finally, this article highlights the research challenges and future prospects of Cu/S-associated nanomaterials with $ERCO_2$.

2. Characteristics for improving the $ERCO_2$ performance of Cu/S-associated catalysts

This section discusses the essential features of Cu/S-associated catalysts to understand their fundamental characteristics, which are mentioned below in each subsection. They were briefly addressed in the following subsections.

2.1 Exposed Facets for improving electrocatalytic performance

As reported by many literatures, tuning the exposed facets of nano-electrocatalysts may alter atomic rearrangements, reaction intermediate affinity, and surface energy, influencing the electrochemical activity.[97,98] Inspired by this, the group presented a simple and effective technique for limiting product distribution using sulfur-modified Cu_2O electrocatalysts.[99] A wet chemical technique was used to synthesize distinct morphologies of Cu_2O effectively with varied exposed facets (Fig. 3a). Surprisingly, they observed that the Faradaic efficiency of formate on sulfur-modified Cu_2O electrocatalysts was significantly sensitive on Cu_2O crystal facets, as shown in Fig. 3b-i, with selectivity in the order of Cu_2O (100) > Cu_2O (100)/ (111) > Cu_2O (111). Among all the sulfur-modified Cu_2O electrocatalysts prepared, the optimized S3-Cu_2O-70 demonstrated FE of 90% at -0.9V_{RHE} and extended stability of more than 80h in an H-type cell. Furthermore, the flow-associated cell system achieved a $j_{formate}$ of 260±16 mA/cm^2, outperforming most formate-producing Cu-associated electrocatalysts. Sulfur can improve water activation for synthesizing unique H_2 species and reduce the activation energy of *OCHO intermediate formation on the surface of sulfur-modified Cu_2O, boosting formate selectivity in $ERCO_2$, according to experimental data and Density functional theory (DFT) calculations. Similarly, He et al.[100] investigated the role of rich high-index facets polycrystalline Cu (Cu-s) nanoparticles successfully derived from $Cu_{2-x}S$ nanocrystals, as illustrated in Fig. 3j. They observed that the formation of high-index facets during surface reconstruction is beneficial in providing surface active sites for C-C coupling, thus boosting C_2H_4 generation. The Cu-S nanocatalysts exhibited high catalytic performance with an FE of 68.6% (j_{C2H4} of 40.8 mA/cm^2) for C_2H_4 because of vicinal facet formation during surface engineering. Furthermore, in-situ studies demonstrated that Cu-S electrocatalysts use the *COCHO intermediates route for producing C_2H_4 via $ERCO_2$. Similarly, Dou et al.[101] investigated the facet-dependent selectivity and activity of CuS nanosheet arrays on brass mesh for $ERCO_2$ prepared via facile and green chemical bath deposition approach (Fig. 3k). Meanwhile, connecting CuS with BM increased overall performance (j = 75 mA/cm^2 at -0.7V_{RHE} and FE_{HCOO^-} = 67.8 ± 1%) for $ERCO_2$. Instead, PTFE-coated CuS/BM achieved more enhanced CO_2 conversion to HCOOH/HCOO- generation (FE = 70.2 ± 1% at 0.7 V$_{RHE}$) than CuS/BM. Their investigations reveal that the reconstruction of CuS/BM resulted in a uniform nanowire framework with abundant active surfaces during the $ERCO_2$, considerably increasing catalytic reactivity. They integrated DFT research with experimental findings. The work attributes the high selectivity for $HCOO^-$ production to the reconstructed formation of the Cu (111)/CuS (102) facets throughout the electrolysis process. According to the theoretical investigation, S under the CuO layer reduces the binding energies of HCOO* and *COOH on Cu(111)/CuS(102) compared to the Cu(111) plane, allowing the development of HCOOH or HCOO*.

2.2 Edge Engineering for improving electrocatalytic performance

Recent research has established that the exposed edges of transition metal chalcogenides are more catalytically active than planar surfaces in electrochemical reactions.[102,103] The more exposed edges to the electrode/electrolyte interfaces can improve the electrochemical performance owing to more active sites. Owing to the sufficiently exposed-edge planes, the hierarchical hollow CuS microcubes (MCs) provided remarkable electrocatalytic properties for CO_2 reduction with a FE_{CO} of 32.7% at a lower onset potential -0.2V_{RHE}. Shao et al.[104] observed engineered novel surface and morphology-enhanced exposed edge sites, offering significantly higher electrocatalytic activities and selectively toward $ERCO_2$. They demonstrated CO_2 electro-reduction with lower overpotential above hollow CuS microcubes (MCs). According to the morphological characterization, it has been shown that as-synthesized h-CuS MCs lead to more significant densely defect edge exposed sites, essential for enhanced Conversion activity and selectivity.

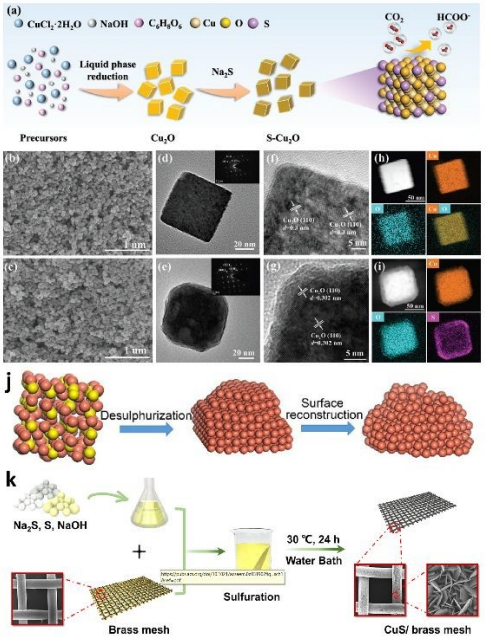

Fig. 3. Synthesis and morphological characterization. a) Schematic illustration of the electrocatalysts preparation process. SEM images of b) S0-Cu_2O-70, c) S3-Cu_2O-70. TEM images of d) S0-Cu_2O-70 and e) S3-Cu_2O-70 (the inset is the selected area electron diffraction (SAED) patterns). HRTEM images of f) S0-Cu_2O-70, g) S3-Cu_2O-70. Corresponding elemental mappings of h) S0-Cu_2O-70, i) S3-Cu_2O-70. (Reproduced on permission from [99]. Copyright, Wiley-VCH GmbH 2023). J) Diagrammatic representation of the conversion from $Cu_{2-x}S$ to Cu-s. (Reproduced on permission from [100]. Copyright,

Springer Nature 2021). k) Diagrammatic representation of the CuS NSs Arrays/BM synthesis method. (Reproduced on permission from [101]. Copyright, ACS 2021)

2.3 Porous effect for improving electrocatalytic performance

Owing to their high specific surface areas, nanoporous structures significantly accelerate surface reactions and facilitate mass transfer by enhancing contact between the electrolyte and the active site.[105] The adsorption and transformation of intermediates, the release and diffusion of gas products, and the lowering of electron transfer resistance are all significantly more accessible by the active sites of the nanoporous structures.[106,107] Inspired by this, Li et al.[108] designed and synthesized hollow-ordered porous copper sulfide cuboctahedra (HOP CuS-CO) with regulated shell thicknesses, as shown in Fig. 4a-h, to produce selective formate from $ERCO_2$. The hollow shells of HOP CuS-CO possess uniformly distributed and interconnected pores. With these advantages and benefits of porous cages, the HOP CuS-CO catalyst exhibited an exceptional $FE_{formate}$ of 70.3% with stability of up to 26 h at a potential of -1.1V_{RHE}. In situ Raman spectroscopy studies showed that the HCOO* intermediates adsorption energy is favourable on the surfaces of HOP CuS-CO by a spatial confinement effect, resulting in highly effective $ERCO_2$ to formate generation. The above studies provided insights into designing novel morphologies for more outstanding formate production using $ERCO_2$. Recently, Yabuki et al.[109] employed the thermal breakdown of sulfur and copper-amine complex ink to create copper sulfide film electrodes. Further, the XRD study confirmed that $Cu_{1.8}S$ and CuS nanoparticles were present in the film. The copper sulfide film possessed variations in the surface area caused by the film's micropores, exhibiting $ERCO_2$ to CO, CH_4, and C_2H_4, with a more significant percentage of C_2H_4 (C_2 product) than a copper electrode.

Zhu et al.[110] synthesized highly porous Cu_2S-decorated copper foam (Cu-foam), an active CO_2 reduction electrocatalyst in an H-cell system. They used anodization followed by a heat treatment process to deposit Cu_2S nanoarrays on Cu foam. Anodization was placed in the first phase in an electrocatalytic cell, employing platinum foil as the cathode and Cu-foam as the anode in an aqueous Na_2S solution. After the anodization, the anodized Cu-foam was washed multiple times with distilled water, followed by thermal treatment. The 3D-shaped Cu_2S/Cu-foam electrode produces much more HCOOH (FE_{co}= 85%with j = 5.3 mA/cm^2 at -2.0$V_{Ag/AgCl}$) than the Cu-foam (FE_{co}= 38.9% at –1.8 $V_{Ag/AgCl}$). Using a simple hydrothermal procedure, Zhao et al.[111] efficiently fabricated economical, robust and highly porous CuS nanosheet arrays successfully decorated on porous nickel foam support, as illustrated in Fig. 4i, for $ERCO_2$ activity. The CuS nanosheet is highly dense and is evenly dispersed over the highly porous Ni foam structure, forming a 3D organized foam CuS/NF, as shown in Fig. 4j-m. The thicknesses of the highly porous CuS/NF framework range from 20 to 25 nm. Their findings revealed that S concentration in the electrodes facilitates CO_2 adsorption and speeds up the rate-limiting step by producing CO_2 to $CO_2^{\bullet-}$ intermediates. Next, the $CO_2^{\bullet-}$ intermediate produces CH_4 by PCET reaction. Thus, the CuS@NF achieved an extraordinary Faradaic Efficiency of 73.5% at -1.1V_{RHE} CH_4 formation and was stable up to 60hr.

3. Emerging regulation for improving the $ERCO_2$ activity

3.1 Phase effect for improving electrocatalytic performance

This section discusses the $ERCO_2$ activity of catalysts, which is determined by the final stage of the active metal's conversion, not the initial phase.[112–114] Notably, Cu/S-associated materials typically act as pre-catalysts for $ERCO_2$ due to their conversion to oxide form during electrolysis. Due to their high oxidation potential, Cu/S-associated materials could be almost totally/partially transformed into their oxide species.[115,116] For example, Chen et al.[117] observed that during the $ERCO_2$, copper sulfide nanoflowers (Fig. 5a and 5b) undergo restructuring to metallic Cu (Fig. 5c), and S^{2-} ions are released

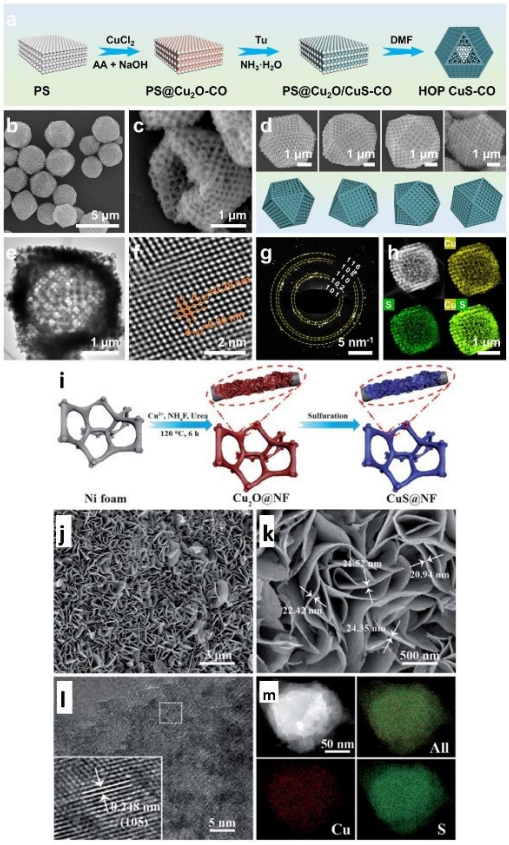

Fig. 4. (a) Schematic illustration for synthesising HOP CuS-CO. (b) SEM image of HOP CuS-CO. (c) SEM images of one individual HOP CuS-CO crystal projected from four different directions. (d) SEM image of partially broken HOP CuS-CO particle. (e) TEM, (f) HRTEM and (g) SAED pattern images of HOP CuS-CO. (h) HAADF-STEM image and corresponding elemental maps of Cu (yellow) and S (green). (Reproduced on permission from [108]. Copyright, Elsevier 2024) (i) Schematic illustration for synthesising CuS@NF samples; (j) SEM images of CuS@NF sample. (Reproduced on permission from [111]. Copyright, RSC 2017).

into the electrolyte and absorbed on the surface of Cu catalysts. This phenomenon suppressed the formation of other hydrocarbon products, resulting in high selectivity towards HCOOH during $ERCO_2$. Copper sulfide pre-catalysts with high S content may absorb more S^{2-} ions on the Cu surface, resulting in higher FE_{HCOOH}. To assess this hypothesis, they used copper foil as the electrode and added varying amounts of K_2S to the $KHCO_3$ electrolyte. Later, they discovered that the FE_{HCOOH} of copper gradually increased with increasing K_2S concentrations. In this context, Phillips et al.[118] used in situ electro-reduction to investigate selective formate production over copper sulfide-derived copper surfaces (S-derived Copper) (Fig. 5d-i). As evidenced by surface-enhanced infrared absorption spectroscopy (SEIRA), the afore-electrocatalyst reduces H_2 and CO formation while enhancing formate selectivity. The authors interpreted this increase in formate selectivity by describing a plausible reaction mechanism in which the active sites are occupied by CO_{ads}, preventing the adsorbed hydrogen molecules (H_{ads}) from combining and producing an H_2 molecule. As a result, H_{ads} could only generate H_2 in solution by making bonds with protons via PCET. Theoretical simulations suggest H_{ads} might create HCOOH by reacting with a solution-phased-CO_2

molecule rather than an H^+-containing solution. As a result, H_{ads} molecules adsorbed on S-derived Cu surfaces and generated HCOOH by interacting with solution-phase CO_2 via PCET.

carbon surface coverage (<4%) for total format selectivity to achieve the highest FE (12%). The efficiency of formate generation in $ERCO_2$ can be increased using sulfur-derived copper with carbon catalysts.

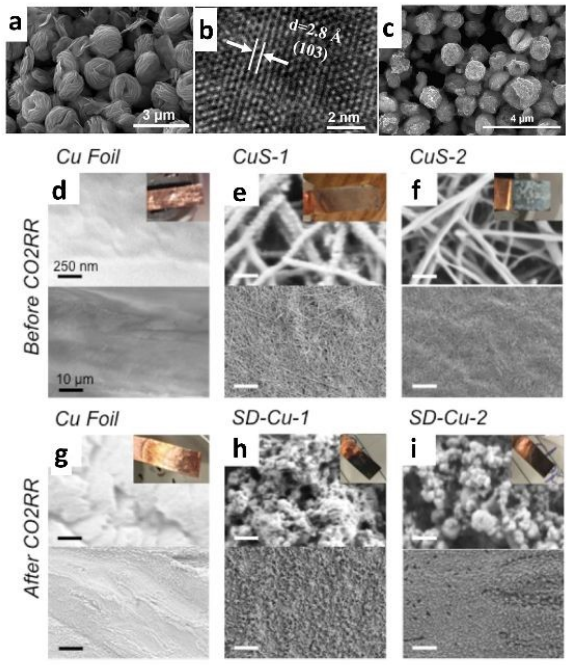

Fig. 5. (a) SEM image and (b) HR-TEM image of CuS nanoflowers before $ERCO_2$; (c) SEM image of CuS nanoflowers after $ERCO_2$. (Reproduced on permission from [117]. Copyright, Elsevier 2024). SEM Imaging of catalyst surfaces (d–f) before and (g–i) after $ERCO_2$. (d, g) Copper foil, (e, h) copper sulfide (CuS) electrodeposited for 30 min (CuS-1), and (f, i) CuS electrodeposited for 2h (CuS-2). The CuS samples convert to SD-Cu after $ERCO_2$ (Top scale bars - 250 nm, and bottom scale bars - 10 μm for each panel). (Reproduced on permission from [118]. Copyright, ACS 2018).

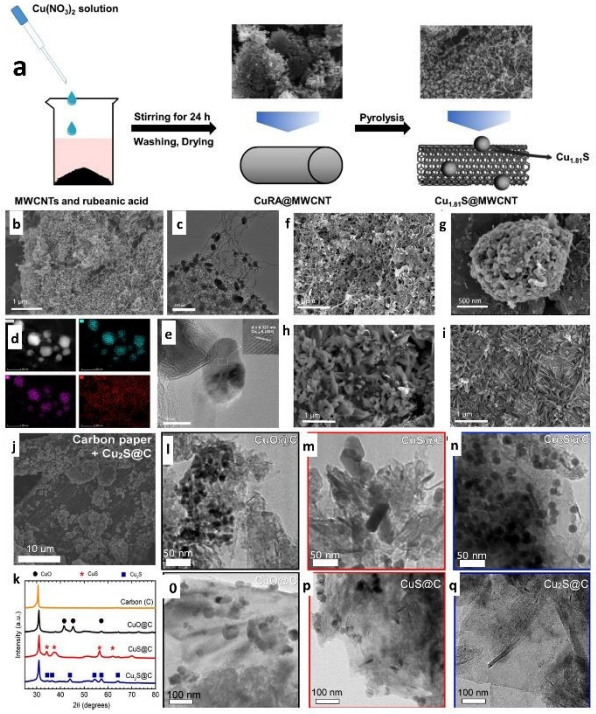

Fig. 6. (a) Schematic illustration of the preparation of $Cu_{1.81}S$@MWCNT. (b) SEM and (c) TEM images of $Cu_{1.81}S$@MWCNT-600, (d) HAADF-STEM image and corresponding EDS maps revealing the uniform distribution of Cu (blue), S (purple) in the $Cu_{1.81}S$ particles, and (e) HRTEM of $Cu_{1.81}S$@MWCNT-600. SEM Images of used $Cu_{1.81}S$@MWCNT-600-OD after (f) 10 min, (g) 20 min, (h) 1 h, and (i) 20 h of $ERCO_2$. (Reproduced on permission from [119]. Copyright, Elsevier 2020). (j) SEM images of the carbon paper substrate with Cu_2S@C deposited on the carbon fibres by spraying. .(k) XRD of the bare GNP-500 carbon support (orange) and of the CuO@C (black), CuS@C (red) and Cu_2S@C (blue) nanoparticles on this carbon support.TEM images of (l) CuO@C, (m) CuS@C and (n) Cu_2S@C nanoparticles before electrolysis; TEM figures of the (o) CuO@C-, (p) CuS@C-, and (q) Cu_2S@C-derived catalysts after 5 h of $ERCO_2$. (Reproduced on permission from [120]. Copyright, Elsevier 2021)

In a different work, through a straightforward two-step coupling procedure via hydrothermal method followed by pyrolysis, as illustrated in Fig. 6a, Zhang et al.[119] created a $Cu_{1.81}S$ catalyst supported by a multi-walled carbon nanotube (MWCNT). Due to the highly active sites of the uniformly dispersed $Cu_{1.81}S$ particles and the effective electron transport and active sites provided by MWCNT, the $Cu_{1.81}S$@MWCNT-600 composite catalyst (Fig. 6b-e) was able to achieve superior $ERCO_2$ performance with 30h stability during continuous operation. Later, they reported that $Cu_{1.81}S$@MWCNT-600 ($Cu_{1.81}S$@MWCNT-600-OD) with oxide modification showed improved catalytic activity and had a high $FE_{Formate}$ of 82%. According to the authors, copper oxide, which changed the phase into a needle-shaped structure during $ERCO_2$, provided more active sites and improved electrocatalytic activity (Fig. 6f-i). In another work, Oversteeg et al.[120] investigate the role of phase engineering via $Cu_{2-x}S$ derived copper sulfide-supported carbon (CuS/C and Cu_2S/C) (Fig. 6j, 6m and 6n), $ERCO_2$ catalyst synthesized using the liquid phase sulfidation of CuO/C nanoparticles (Fig. 6l and 6o). All the prepared phases are confirmed from XRD analysis, as shown in Fig. 6k. According to the electrochemical and in-situ X-ray absorption spectroscopy (XAS) spectroscopy investigations, the metallic Cu reduction occurs in CuS@C and Cu_2S/C nanoparticles during electrochemical CO_2 reduction (Fig. 6p and 6q). Later, their observation revealed that CuS/C- and Cu_2S/C-derived catalysts had higher selectivity towards creating formate at low current densities than the CuO/C-derived electrocatalyst. Surprisingly, the catalyst only needed less

An interesting approach has been reported recently, in which they created a series of CuS using different precursors and examined their relationship with phase restructuring and $ERCO_2$ catalytic activity during electrolysis. First, Guo et al.[121] employed hydrothermal synthesis to create several CuS using different sulfur precursors (i.e., TU=Thiourea, STS=Sodium thiosulfate, TAA=Thioacetamide, and SS=Sodium sulfide). Surprisingly, in $ERCO_2$ activity, CuS-TU outperformed the other electrodes (i.e., CuS-STS, CuS-TAA, and CuS-SS in CO_2-saturated 0.1 M $KHCO_3$ electrolytes, with an FE_{CO} of 72.67% (-0.51 V_{RHE}) and a high CO selectivity. They hypothesized that the thiourea precursor's rapid S decomposition led to a higher concentration of dissolved S^{2-} in the electrolyte, helping quicker nucleation and restructuring of a nanoflower like CuS-Thiourea electrocatalyst for more enhanced mass transfer kinetics and favourable $ERCO_2$.

The phase engineering of a target nanocrystal (NC) can be systematically varied by carefully substituting metal cations in a prefabricated NC template using an emerging electrochemically driven cation exchange (ED-CE) approach. He and coworkers[122] recently designed a Cu_2S catalyst for $ERCO_2$

View Article Online
DOI: 10.1039/D4YA00302K

from the CoS_2 template via the ED-CE approach (Fig. 7a). Employing the ion exchange process, Cu almost entirely replaces Co cations in CoS_x, and the Cu/S atomic ratio is ~2.4. The Cu_2S catalyst produced by converting the predesigned template retains the initial morphology of CoS_2 by preserving its high grain-boundary density, improving CO_2 adsorption. Also, the electronic structure of the nearby Cu sites has changed due to electronegative S heteroatoms, creating positively charged Cu^+ sites. The primary formate intermediate, *OCHO species, is formed when partially positive-charged Cu sites adsorb CO_2 molecules with more electronegative oxygen. The as-prepared 3D-shaped Cu_2S catalysts observed an FE of 87% with a current density of 19 mA/cm^2 at -1.9V_{RHE} in a 0.1 M $NaHCO_3$ medium for the Cu_2S nanocrystal electrode was exhibited for CO_2 conversion to HCOOH. Li et al.[123] utilized copper sulfide nanosheets as a template to develop Ag/Cu electrocatalysts through a straightforward ED-CE process (Fig. 7b and 7c). When the Ag^+ concentration in the exchange solution increased, the crystal structure of $Cu_{2-x}S$ nanosheets with lateral dimensions of 100 nm and a thickness of 14 nm progressively changed from Cu_7S_4 to Ag_2S (CA-nano-x, cation-exchanged nanosheet where x indicates a higher concentration of Ag). The Ag/Cu mass ratio varied between 0.3 and 25. Hence, at an average overpotential (-0.2 V_{RHE}), both C-nano-0 and CA-nano-x exhibited outstanding FE_{HCOOH}. Surprisingly, when the Ag combination increases, formate-producing C-nano-0 can generate C_{2+} products at -1.0 V_{RHE}. Their observation concludes that the nanosheets show shape distortion as the Ag content rises while maintaining their original morphology after the cation exchange process.

In 2024, Goh et al.[124] investigated phase-engineered sulfide-derived Cu-Sb electrodes for electrochemical CO_2 conversion in a gas diffusion electrode (GDE) associated cell. They synthesized several distinct Cu-Sb-S phases, skinnerite (SK; Cu_3SbS_3), tetrahedrite (TH; $Cu_{12}Sb_4S_{13}$), and chalcostibite (CS; $CuSbS_2$) using a heat-up colloidal nanoparticle route, as illustrated in Fig. 8a-f, and each observed a different selectivity for $ERCO_2$ with CO as the main product, which contrasts with the individual CuS_x and SbS_x control samples, which show a preference for the formate product. They also demonstrated that the different elemental compositions caused the different selectivity patterns when the parent phases were reduced using fundamental composition characterization after reduction. Interstingly, lower Cu concentrations reduce phase segregation into harmful S-doped Cu that converts CO_2 to HCOO and H_2, whereas higher sulfur concentrations disrupt crystallinity and promote CO formation. This outstanding performance is attributed to the tetrahedral Cu-Sb-S sample, which has the highest residual sulfur, attributed CO_{FE} of about 80.5% at -1.0V_{RHE}, and a $j_{geometrical}$ of 37.6mA/cm^2. Post-electrocatalysis characterization combined with DFT calculations demonstrated that adding sulfur to Sb sites enhances *COOH binding compared to *CO, rupturing scaling relations and aiding in CO (g) formation afterwards.

Similarly, in 2023, Mai et al.[125] used a facile solvothermal technique to create several cuprous sulfide nanoparticle-modified copper hydroxide nanowire array (S-CNWs) pre-catalysts for elucidating the reaction mechanism in $ERCO_2$ (Fig. 8g-n). They explored the effect of cuprous sulfide nanoparticle modification on formate generation during CO_2 reduction and observed Sulfur modification changes in the intermediate during CO_2 reduction, leading to improved formate selectivity (60% of FE_{co} with j_{HCOO-} = 10 mA/cm^2 at -0.58V_{RHE}). Therefore, the role of trace sulfur alteration in copper surfaces towards selective formate production is investigated using DFT. According to the study, Sulfur modification in copper, as compared to a pure copper surface, can accelerate the synthesis of *OCHO, a critical step along the formate pathway.

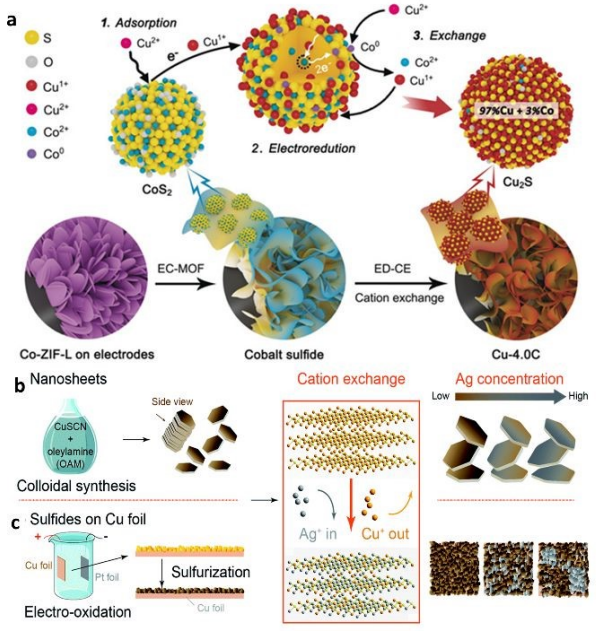

Fig. 7. a) Schematic illustration of the experimental pathways and mechanisms for electrochemically driven cation exchange (ED-CE). Synthetic strategies for Ag/Cu sulfide catalysts. (Reproduced on permission from [122]. Copyright, Wiley-VCH 2020). (b) Cu sulfide nanosheets (C-nano-0, 100 nm lateral dimension, 14 nm thick) were obtained through colloidal synthesis with CuSCN in oleylamine (OAM). (c) Cu sulfides on Cu foil (C-foil-x) were obtained through electrooxidation in 1 M NaOH to produce an oxide layer of a few 10 s of microns thick, followed by sulfurization with 0.1 M Na_2S. After cation exchange where Ag+ replaces the Cu+ in the Cu sulfides, Ag/Cu sulfide nanosheets (CA-nano-x) remain in nanosheet structure with some distortion in shape as the Ag/Cu mass ratio ranges from 0.3 to 25, while for C-foil-x, Ag nucleates at higher Ag concentration, that impedes the uniform distribution of Ag and Cu. (Reproduced on permission from [123]. Copyright, RSC 2021)

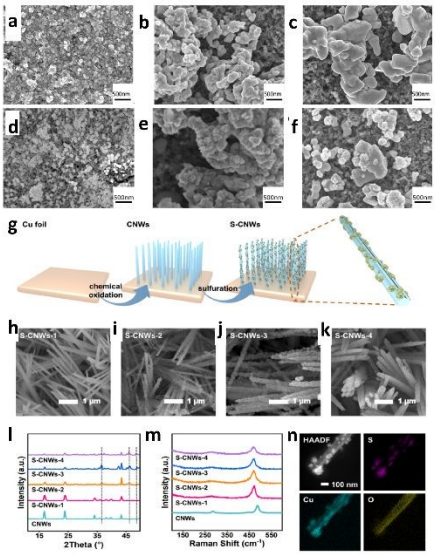

Fig. 8. SEM characterization of the samples before reduction. (a–c) SEM images of the samples SK (a), TH (b) and CS (c) sprayed on carbon paper. SEM characterization of the samples after reduction. (d–f) SEM images of the samples SK (d), TH (e) and CS (f) sprayed on carbon paper. (Reproduced on permission from [124]. Copyright, RSC 2024).

Morphological and structural characterization; (G) Schematic illustration of the of S-CNWs preparation, (h-k) SEM images of S-CNWs with different loadings of TAA at 75OC for 0.75h, (50, 75, 100, and 200 mg per 80 mL for S-CNWs-1, S-CNWs-2, S-CNWs-3, and S-CNWs-4, respectively; (l) XRD patterns of CNWs and S-CNWs with different degrees of vulcanization, (m) Raman spectra of CNWs and S-CNWs with different degrees of vulcanization, (n) HAADF-STEM and corresponding EDS images of S-CNWs. (Reproduced on permission from [125]. Copyright, ACS 2023)

3.2 Size effect for improving electrocatalytic performance

Researchers discover that the surface of tiny nanoparticles is rich in unsaturated atoms and defective sites compared to the bulk, exposing the number of active sites to improve catalytic activity.[126] Reducing nanoparticles even further to nanoclusters (NCs), which are made up of a few hundred or fewer atoms and have an average size of about 2 nm, reveals intriguing electrochemical performance with significant quantum size effects.[127] Shinagawa et al.[128] used a wet chemistry approach to create carbon-supported CuS nanocatalysts by controlling the size. During $ERCO_2$, the experimental investigation demonstrated that the afore nanometric-sized CuS was restructured and reformed to S-modified copper (Cu-S). As a result, at considerable overpotential (-0.8V vs. RHE), Cu-S catalysts produced formate with an FE of > 60% and negligible quantities of CO as a byproduct. They discovered that as the particle size dimension became 3 nm to 20 nm, there was a slight increase in HCOOH production, highlighting the catalytic size-activity relationship. Following that, in a similar article, it was demonstrated that solvothermal-prepared submicron-sized CuS electrodes had better FE_{HCOOH} (80%) for $ERCO_2$ to HCOOH than nanometric CuS (FE_{HCOOH}> 60%), indicating the importance link between particle size-electrochemical activity. Later, Lim et al.[129] studied the impact of size engineering by fabricating a size-controlled CuS_x electrocatalyst in an aqueous medium using Cu foil dipped in an industrial CO_2 that contains H_2S (Fig. 9a-c). As per their observations, the Cu foil and the sulfur interacted properly when the concentration of the sulfur in the solution increased. The simultaneous interactions raised the average particle size and surface sulfur density of CuS_x nanoparticles (NPs) to 133.2±33.1nm and 86.2±3.3%, respectively, as shown in energy dispersive X-ray spectroscopy (EDX) images (Fig. 9c). When the sulfur percentage and sizes of the CuS_x nanoparticles increased steadily, the $FE_{Formate}$ improved from 22.7 to 72.0% at -0.6V_{RHE} (Fig. 9d-g). Although the CuS_x nanocatalysts had a lower current density, the 72-hour stability must be addressed for industrial CO_2 conversion.

3.3 Grain boundaries effect for improving electrocatalytic performance

Grain boundaries (GBs) can be efficient active sites for catalytic processes because they provide an electrodynamically beneficial surface.[130,131] Also, it has been shown that catalytically energized surfaces can be stabilized using grain boundaries (GBs).[132,133] For example, Yang et al.[134] used electrochemical reduction techniques to synthesize S-Cu_2O/Cu hybrid catalysts derived from Cu_7S_4/Cu nanoflowers (Fig. 10a-g). They showed that GBs surface defects in Cu_2O/Cu interfaces were more energized than grain surfaces for $ERCO_2$. They observed that Cu_7S_4/Cu is dynamically restructured in situ to provide an S-Cu_2O/Cu hybrid catalyst for efficient $ERCO_2$ to formate (FE_{HCOOH} up to 70% at -1.0 V_{RHE} with a partial current density of 5mA/cm²) that outperforms Cu_2O/Cu and Cu_7S_4. The authors attributed this performance to (i) thermodynamic and experimental investigations suggesting that the optimized adsorption of the HCOO* intermediate on the S-Cu_2O/Cu surface is modified, and S-doping suppresses the H_2 route (surface H), (ii) GBs at the Cu_2O/Cu interfaces reduce the adsorption energy favoured by S-doping and increased formate efficiency by inhibiting the HER route and CO_2-to-CO conversion. In another work, Wang et al.[135] fabricated S-doped Cu_2O derived from CuS 811 (consisting of CuS and $CuSO_4{\cdot}3H_2O$) using the electrolysis method to study the relationship between the catalytic activity and GBs. This catalyst performed exceptionally well for formate production in $ERCO_2$, reaching an optimal FE of 92% in an H-type cell and an excellent $j_{formate}$ of 321 mA/cm² in a flow cell while retaining an FE of more than 80%. The authors attributed this outstanding performance from two viewpoints. (1) Structural studies showed that $CuSO_4 \cdot 3H_2O$ inhibits CuS growth and vice versa, leading to lesser grain sizes and more primary GBs (Fig.

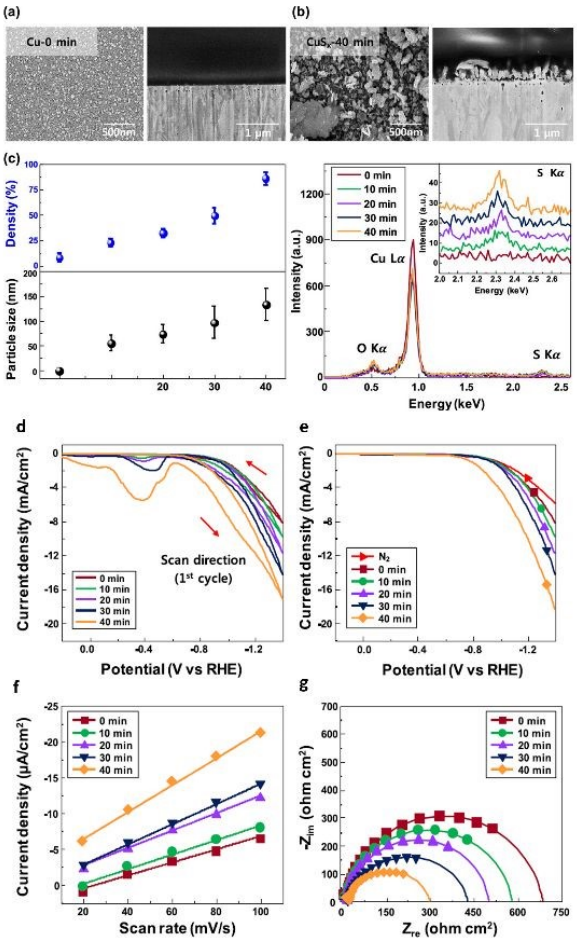

Fig. 9. Top-view and cross-sectional SEM images of (a) Cu-0 min without sulfur species and (b) CuS_x-40 min catalysts. (c) The average particle size and surface density of CuS_x NPs were calculated using a computing-based image analyzer and EDX spectra of Cu and CuS_x catalysts. (d) CV (1st scan) of CuS_x catalysts with different amounts of sulfur species. (e) LSV curves in N_2-purged and industrial CO_2-purged 0.1 M $KHCO_3$ electrolytes at a scan rate of 50 mV/s. (f) Current density plots at various CV scan rates. The current densities were obtained from the double-layer charge/discharge curves at 0.40 V_{RHE} in industrial CO_2-purged 0.1M $KHCO_3$ electrolyte. (g) Nyquist impedance plots of catalysts in industrial CO_2-purged 0.1M $KHCO_3$ electrolyte from 1 MHz to 0.1 Hz with 30 mV amplitude at −0.6 V_{RHE}. (Reproduced on permission from [129]. Copyright, ACS 2020)

10h-k). After electrolysis and electrochemical reduction, these grains break down into smaller ones, resulting in more dense grain boundaries suitable for electrocatalysis (Fig. 10l and 10m). (2) The kinetics of S shedding during electrochemical $ERCO_2$ are comparatively slow because of the initial mixture of multi-crystalline phases; this leads to a higher S content and a relatively complete CuS crystalline phase in CuS 811 post $ERCO_2$. They did DFT calculations and exhibited that retaining Sulfur-Sulfur bonds from covellite may reduce the binding energy, mainly by weakening the binding energies with several reaction intermediates, decreasing the energy barriers and

facilitating the desorption steps, thus increasing formate generation activity. The catalytic impact of the GB was comparable to its dislocation strain field, establishing the way for a more comprehensive application of the GB effects in heterogeneous catalysts. More extensive research is required to understand the fundamental principle of GBs and apply it to developing advanced catalytic schemes for the $ERCO_2$ into valuable products.

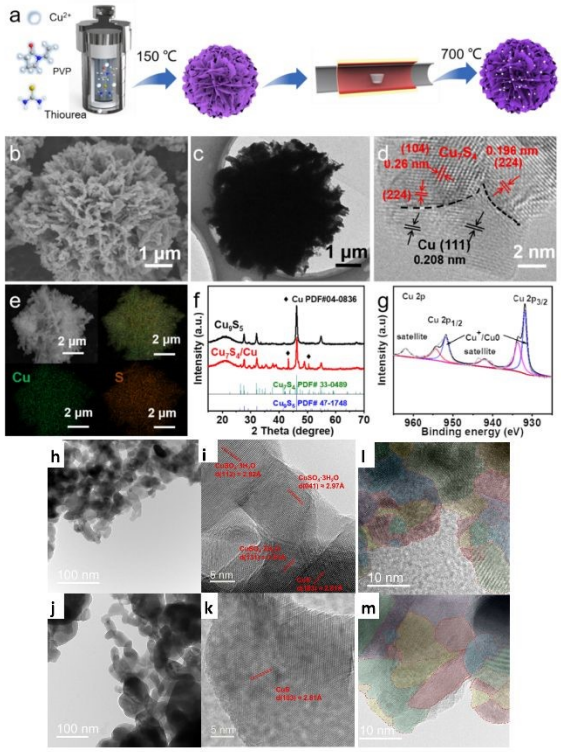

Fig. 10. (a) Schematic illustration of the synthetic process, (b) SEM image, (c) TEM image, (d) HRTEM image, (e) EDS elemental mapping, and (g) XPS pattern of Cu_7S_4/Cu. (f) XRD patterns of Cu_7S_4/Cu and Cu_9S_5. (Reproduced on permission from [134]. Copyright, Wiley-VCH 2024). Morphology and construction investigation of CuS 811 and CuS MKL before $ERCO_2$ by electron imaging. (h, i) Aberration-correction TEM images of (h) CuS 811 and (i) CuS MKL. (j, k) HRTEM images of (j) CuS 811 and (k) CuS MKL. The crystal facets with heterogeneous species are highlighted in (j, k). Construction Investigation of CuS 811 and CuS MKL post $ERCO_2$ by electron images. (l,m) HRTEM images of (l) CuS 811 and (m) CuS MKL. Red dash-dot lines highlight the boundaries of induced grains, and the grains with heterogeneous lattice fringes are marked in various colours (l,m). The marking colours are only used to distinguish every grain, and there is no correlation between the colour and phase. (Reproduced on permission from [135]. Copyright, Wiley-VCH 2024)

3.4 Defect/vacancy creation effect for improving electrocatalytic performance

Defect engineering, such as vacancy creation, edge exposed-site, and heteroatom doping, is essential in electrocatalytic activities because defects are usually rich in active sites.[136,137] Furthermore, defects can modulate the electronic properties of active sites, increasing the density of catalytic active sites. As a result, defect engineering has appeared as a strategy mostly used to increase active sites and improve charge transfer ability to fine-tune electrocatalytic activity.[138,139] Therefore, considering the connection between diverse defects and the specific catalytic properties of various materials is critical for developing advanced catalysts.[140,141]

For example, n-propanol is a problematic product to form during electrolysis because of the complicated C_3 creation mechanism that requires the stabilization of $*C_2$ intermediates and subsequent C_1-C_2 coupling. Zhuang and colleagues[142] synthesized a bifunctional core-shell nanostructure (Fig. 11a) showing that adding sulfur atoms to the catalyst core and copper vacancies to the shell named core-shell vacancy engineered Cu (CSVE-Cu) results in excellent $ERCO_2$ to n-propanol activity. The CSVE-Cu electrocatalyst exhibited satisfactory reduction performance by generating highly energy-dense C_{2+} alcohols (i.e., C_3H_7OH and CH_3CH_2OH) with a FE of 32%±1%. The alcohol-to-ethylene ratio increased sixfold compared to simple copper nanoparticles, indicating an alternative route for producing alcohol instead of alkenes. According to DFT modelling, the incorporated vacancy, as shown in morphology analysis from Fig. 11b-g, on a bifunctional core-shell catalyst raises the activation energy of the C_2H_4 route (1.148eV). Still, it does not affect the CH_3CH_2OH path (0.427eV). Peng et al.[143] created a double-sulfur vacancy (DSV) engineering structure to evaluate enhanced $ERCO_2$ performance. The mechanistic study showed that the DSV-engineered CuS(100) planes facilitated the stabilization of both CO* and OCCO* a $*C_2$ dimer with the following interaction via a third *CO via CO-OCCO (Fig. 11h-k). The DSV-engineered CuS_x exhibited an improved $FE_{n\text{-}PrOH}$ of ~15.4% −1.05 V_{RHE} for n-propanol formation at 0.1M $KHCO_3$ medium in the H-cell set, but in flow cells, $j_{n\text{-}PrOH}$ was increased to 9.9mA/cm^2. This study supports an appealing strategy for using the lithium electrochemical tuning method to create an array of novel frameworks with ion vacancies as active sites for electrochemical reactions.

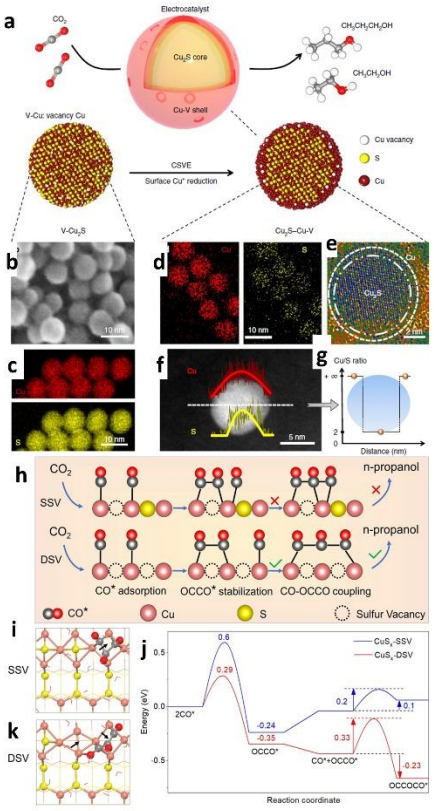

Fig. 11. Catalyst design and structural characterization. a, Schematic illustration of Cu_2S–Cu-V CSVE electrocatalyst design for production of multi-carbon alcohols from CO_2 reduction. b,c, TEM (b) and EDS (c) mapping of the original V-Cu_2S nanoparticles, showing the uniform size and the homogeneous distribution of Cu and S. d–g, EDS mapping (d), high-resolution TEM (e), EDS line scan (f) and the ratio of Cu/S concentration (g) of the reduced CSVE nanocatalysts after electrochemical reduction, showing the removal of S from the nanoparticle surface. V-Cu indicates Cu with surface vacancies. (Reproduced on

View Article Online
DOI: 10.1039/D4YA00302K

permission from [142]. Copyright, NATURE 2018). (h) The mechanism of n-propanol formation on adjacent CuSx-DSV shows the dimerization of CO–CO followed by CO–OCCO coupling. (i,k) Top views of the optimized OCCOCO* intermediate configurations on (100) surface of (i) CuSx-SSV and (k) CuSx-DSV. The arrows indicate the positions of sulfur vacancies. (j) Corresponding energy diagrams for CuSx-SSV (blue curve) and CuSx-DSV (red curve) at 0 V vs. RHE. The pink, yellow, grey, red spheres and red wireframe in (h-k) represent copper, sulfur, carbon, oxygen atoms, and water molecules, respectively. (Reproduced on permission from [143]. Copyright, NATURE 2021)

3.5 Heterostructured effect for improving electrocatalytic performance

The heterostructure commonly comprises more than one component that accomplishes different roles in the electrocatalytic reactions.[144] Modifications in physical and chemical properties will enhance each component's combined advantages. As a result, the various components will produce a synergistic effect, contributing to $ERCO_2$ kinetics.[145,146] Unlike single-component catalysts, the synergistic effects caused by heterogeneous interfaces can significantly improve catalytic activity.[147] Inspired by this, recently, Tao et al.[148] developed a novel Cu_2S/SnO_2@C nanocomposite by solvothermal heating, where SnO_2@C is confined on the snowflake-like Cu_2S surface and has a combined interfacial effect at the Cu_2S sites (Fig. 12a-e). Specifically, the Cu_2S snowflake improves the CO_2 concentration near the surface, and carbon spheres increase the surface electron transport capacity. Afterwards, the as-synthesized Cu_2S/SnO_2@C nanocomposites are used as a working electrode to investigate $ERCO_2$ to HCOOH. They varied the loading amount to examine the impact of the SnO_2@C content on the $ERCO_2$. The prepared $Cu_2S/1\%SnO_2$@C shows good selectivity and activity for $ERCO_2$, which outperformed all the existing Cu-associated electrocatalysts for liquid HCOOH products. The electrochemical study demonstrated a high ECSA, exceptional CO_2 adsorption capacities and a fast electron transport rate at the surface of $Cu_2S/1\%SnO_2$@C. Additionally, DFT calculations revealed the plausible reaction pathways for the enhanced HCOOH production by Cu_2S/SnO_2@C. Notably, through heterostructure construction, this work provides an easy method to fabricate effective Cu-associated catalysts that can improve HCOOH selectivity and activity in the $ERCO_2$ process.

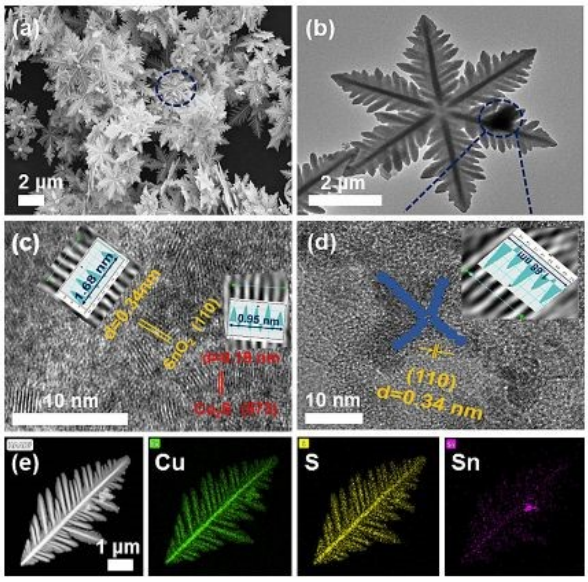

Fig. 12. SEM image (a) and TEM image (b) of Cu_2S/SnO_2@C. HRTEM images of Cu_2S/SnO_2@C (c) and SnO_2@C (d). The HAADF-STEM image and the corresponding elemental mapping of Cu_2S/SnO_2@C (e) reveal the distribution of Cu (green), S (yellow), and Sn (rosy), respectively. (For interpretation of the references to colour in this figure legend, the reader is referred to the web version of this article.) (Reproduced on permission from [148]. Copyright, ELSEVIER 2023).

Another work used a redox process at ambient temperature to create a heterostructure of CuS and S-doped SnO_2 (CuS/ SnO_2-S) for $ERCO_2$, as shown in scheme 1 in Fig. 13.[149] Structure analysis methods revealed the structural regeneration phase that had occurred during the first electrolysis (Fig. 13a-i). The unique restructuring of CuS/SnO_2-S heterostructure to $Cu/Sn/Cu_{6.26}Sn_5$ nanowires reduces CO_2 adsorption energy while increasing *H adsorption, reducing the competing HER. During $ERCO_2$, at -0.8 V_{RHE}, it achieves a formate conversion with FE of 84.9% and a yield of 8860 $\mu molh^{-1}cm^{-2}$ in an H-Cell at a $j_{formate}$ of 18.8 mA/cm^2. This research focused on the structural development of CuSn sulfides from precursor materials's early state as well as the process of formate production.

Wang et al.[150] created an innovative framework of 0D/2D composites of SnO_2 nanoparticles dispersed on CuS nanosheets (SnO_2/CuS) for selective syngas generation (CO/H_2 ratio of 0.11-3.86), as illustrated in scheme 1 in Fig. 14. The electrocatalytic system was highly efficient for syngas selectivity, with a Faradaic Efficiency of nearly 85%, a turnover frequency (TOF) of $96.12h^{-1}$, and stability of 24 hours. They emphasized the increased catalytic activity by two factors: (a) the most active sites are provided by the uniformly distributed ultrasmall SnO_2 nanoparticles on ultrathin CuS nanosheets, enabling a faster electron transfer rate (Fig. 14a-c), and (b) the interfaces between SnO_2 and CuS lower the activation energy of reaction intermediates, enhancing $ERCO_2$ performance to generate high-ratio tunable syngas. Both the SnO_2(110) and CuS(001) facet surfaces, as shown in Fig. 14d and 14e, favoured HCOOH creation. In contrast, the SnO_2/CuS contact considerably lowered the free energy of COOH* intermediate synthesis by 0.52eV and encouraged CO formation.

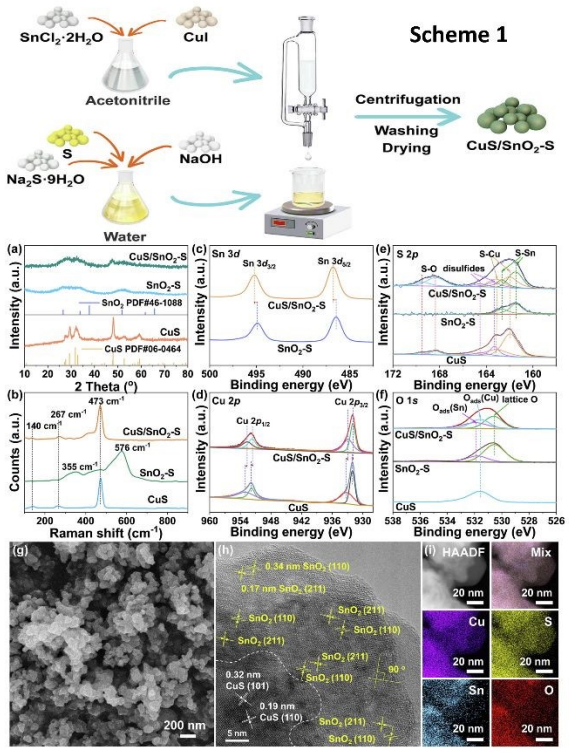

Fig. 13. Scheme 1: The synthetic process of CuS/SnO_2-S. (a) XRD patterns, (b) Raman spectra and (c–f) XPS analyses for Sn 3d, Cu 2p, S 2p and O 1s of CuS/SnO_2-S RCu/Sn high, SnO_2-S and CuS. (g) SEM images and (h) HRTEM and (i) HAADF image and EDS mapping of as-prepared CuS/SnO_2-S RCu/Sn high. (Reproduced on permission from [149]. Copyright, ELSEVIER 2023).

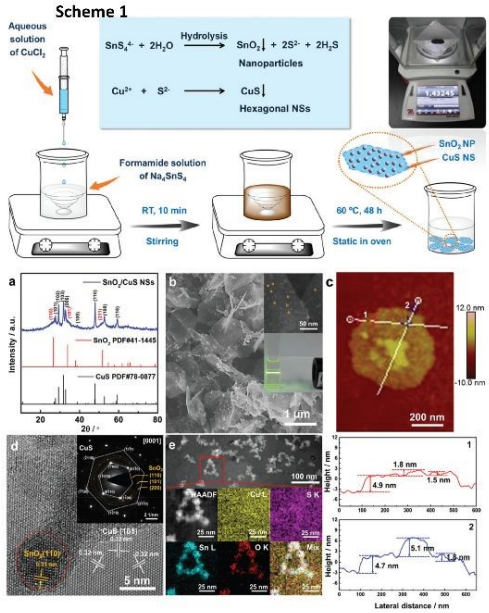

Fig. 14. Scheme 1: Schematic illustration and the proposed reaction mechanism for the one-pot scalable synthesis of hierarchical SnO_2/CuS NSs. Structural characterization of SnO_2/CuS NSs. (a) XRD patterns. (b) SEM and (inset) magnified SEM image of the surface and photograph of the dispersion of SnO_2/CuS NSs in EtOH, demonstrating the Tyndall effect with a laser pointer. (c) AFM image and corresponding height profiles of the as-obtained ultrathin SnO_2/CuS NSs marked by lines in different colours. (d) HRTEM image and corresponding SAED pattern (inset). (e) HAADF-STEM images and corresponding elemental mapping images of SnO_2/CuS NSs. (Reproduced on permission from [150]. Copyright, RSC 2020).

In 2023, Liu and group[151] reported the production of monoclinic-phase colloidal Cu_2SnS_3 nanoplates with precise surfaces (Fig. 15a-h). Their findings revealed that thiocyanate-capped plate-shaped Cu_2SnS_3 nanoparticles exhibit outstanding formate selectivity over a broad spectrum of potentials, observing a formate production with a FE_{max} of 92% with a $j_{formate}$ as high as 181 mA/cm^2 in a GDA-associated flow cell. Compared to prior studies of mono metal- and bimetal-associated Cu- and Sn-sulfide nanoparticles that typically experienced phase separation or the creation of metal-associated domains, whereas the Cu_2SnS_3 demonstrated outstanding structural robustness, as demonstrated by the concurrent retention of nanoplate morphology and crystal phase during $ERCO_2$. In-situ and DFT studies, as shown in Fig. 15i-m, have demonstrated that the Sn sites basal-plane are the multi-active sites for favourable HCOO* adsorption to produce formate in $ERCO_2$. According to DFT studies, thiocyanates also inhibit Cu sites on the surface, and the Sn site's electronic structure modulation is observed, favouring the activation energy barrier of ERCO2, which is reduced to formate.

Also, Xiong et al.[152] used a homogenous mixing approach to create bimetallic $CuInS_2$ hollow nanoparticles. According to the observation, the synergy between metal centres and hollow-shaped nanostructures accelerates the electron transfer kinetics. Consequently, the bimetallic catalyst had a FE_{CO} of 82.3% at -1.0 V_{RHE} and a FE_{HCOOH} of 72.8% at -0.7 V_{RHE}. In-situ studies exhibited faster conversion of rate-limiting step CO_2 to $CO_2^{\bullet-}$ radicals, and afterwards, electron redistribution happened at different potentials, leading to a product distribution shift (CO to HCOOH). Furthermore, Nyquist plots showed that hollow-like $CuInS_2$ nanocomposites have a substantially greater interfacial charge-transfer rate during electrocatalysis than Cu_2In. Because the interfacial charge-transfer impedance (R_{ct}) of Cu_2In is lower than that of $CuInS_2$.

View Article Online
DOI: 10.1039/D4YA00302K

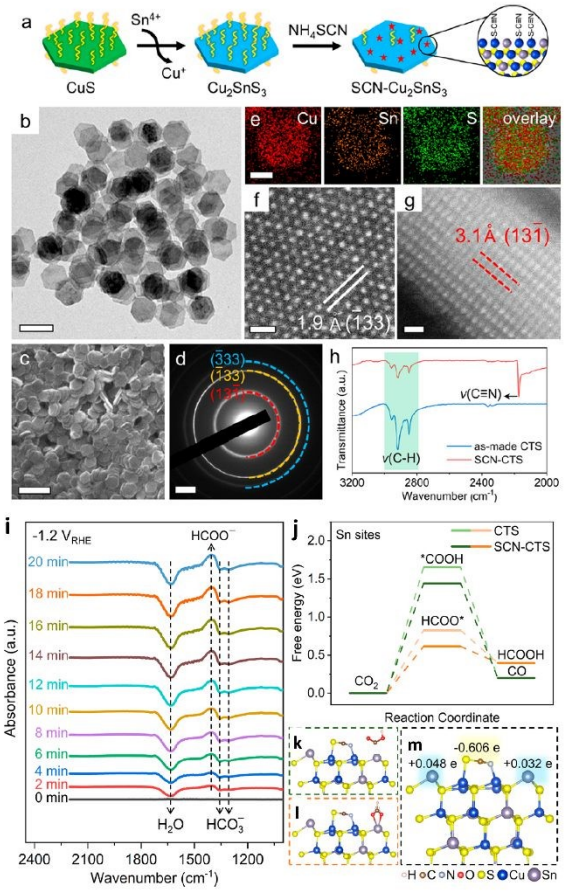

Fig.15. Synthesis and characterization of Cu_2SnS_3 nanoplates. (a) Synthetic scheme of Cu_2SnS_3 nanoplates and ligand exchange with NH_4SCN. (b) TEM and (c) SEM images, (d) SAED pattern, (e) STEM-EDS elemental maps, (f) top-view and (g) side-view ACSTEM images of Cu_2SnS_3 nanoplates. (h) FTIR spectra of Cu_2SnS_3 nanoplates (basal plane edge length: 41.2 ± 2.4 nm) before and after ligand exchange with NH_4SCN. Scale bars: (b) 100 nm, (c) 200 nm, (d) 2 nm−1, (e) 30 nm, (f,g) 0.5 nm. (i) In situ FTIR spectra recorded at different times for CTS-3 at −1.2 V vs RHE. (j) Free energy diagrams of $ERCO_2$ into formate and CO on Cu_2SnS_3 nanoplates. (k-m) Optimized geometric structures of *COOH (j), HCOO* (k), and SCN-modified Cu_2SnS_3 (001) surface (m). Also shown in (m) are charge transfers obtained using Bader charge analysis where e is the elementary charge. (Reproduced on permission from [151]. Copyright, ACS 2023)

Graphdiyne (GDY): a novel 2D all-carbon structure where alkyne bonds (sp-hybridized C) bind each benzene ring (sp^2-hybridized C). GDY's particular sp-/sp^2-hybridized architecture provides numerous distinctive and intriguing qualities that are exceptional to standard carbon materials, i.e., abundant carbon chemical bonds, massive conjugated pi structures, a favourable band gap, etc.[153] More enticingly, the exceptionally variable distribution of surface charges and incomplete charge transfer between GDY and metal centres can offer more active sites, higher intrinsic activity, and efficient control of reaction intermediates' adsorption and desorption behaviour on functional site surfaces.[153] Owing to those advantages, in 2023, Li and colleagues[153] discovered a novel graphdiyne/copper sulfide (GDY/CuS_x) heterostructured electrocatalyst (Fig. 16a) controlling in situ development of GDY over the surface of CuS_x, as illustrated in Fig. 16b-x. The authors attributed that the imperfect charge transfer between GDY and atomic Cu increased catalytic conductivity, providing additional active sites and enhancing the conversion performance. Thus, the heterostructure accomplished an FE of 70% and a j_{total} of 65.6 mA/cm^2 at -0.9 V_{RHE} for $ERCO_2$ to formic acid.

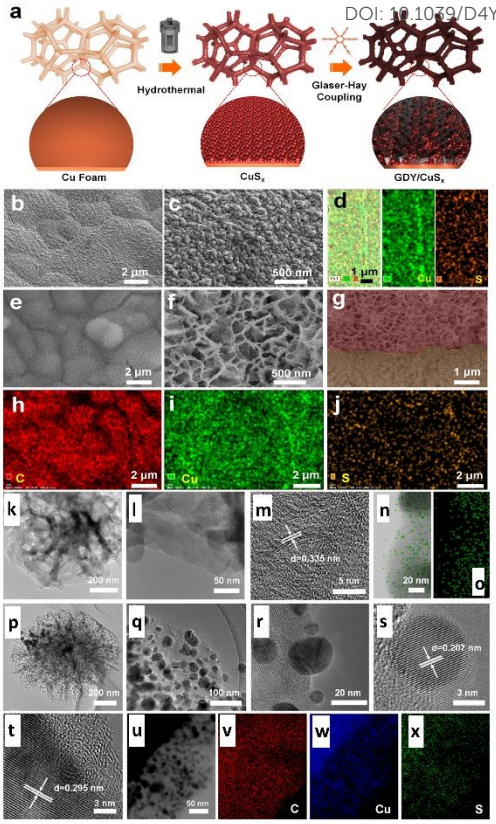

Fig. 16. (a) Schematic representation of the synthesis route of GDY/CuSx; and (b) low- and (c) high-magnification SEM images of CuSx. (d) Energy dispersive spectroscopy mapping of CuSx. (e) Low- and (f) high-magnification SEM images of GDY/CuSx. (g) Cross-section SEM image of GDY/CuSx; and (h, i and j) energy dispersive spectroscopy mapping of GDY/CuSx. (k) TEM and (l and m) HRTEM images of the GDY nanosheet. (n) STEM image (left) and corresponding elemental mapping (right) of the elemental C of GDY. (p-r) TEM and (s and t) HRTEM images of GDY/CuSx, (u) STEM image and corresponding elemental mapping of (v) C, (w) Cu, and (x) S elements of the GDY/CuSx electrode. (Reproduced on permission from [153]. Copyright, RSC 2023)

Heterostructure engineering modulates interfacial charge distribution and promotes CO_2 adsorption: Herein, Wen et al.[154] used a local sulfur doping strategy (SHKUST-1) to properly develop an isolated Cu@S motif on the HKUST-1 pre-catalyst (Fig. 17a). The in-situ reconstruction of S-HKUST-1 results in a Cu(S) array with an array and active biphased copper/ copper sulfide (Cu/Cu_xS_y) interfaces (Fig. 17b), achieving highly selective ethylene (C_2H_4) formation in the H-cell with FE_{max} of 60.0%. In a flow cell configuration, $ERCO_2$ observed a high current density of 400 mA/cm^2 with FE_{C2H4} of approximately 57% and FE_{C2} (FE of C_2H_4, C_2H_5OH and CH_3COOH) of 88.4%. The S motif is stable before and after the $ERCO_2$, as evidenced by the systematic characterizations (Fig. 17c-h). The researchers explain S-HKUST-1's superior selectivity as follows: the approximate distance between Cu^0-$Cu^{\square+}$ favours the *CO dimerization step at the interface of Cu/Cu_2S. Also, a high S-concentrate electrocatalyst (i.e., Cu_2S) showed a significant Cu-Cu distance that practically restricted *CO dimerization. Compared to a pure metallic Cu catalyst, the Cu/Cu_2S interface decreased to *CO species binding energy at the surface and fastened *CO dimerization (Fig. 17i-m). Similarly, in 2023, Yu et al.[155] constructed a Cu_2S nanocrystal on Cu nanosheets (Cu-Cu_2S), as shown in Fig. 18a, for $ERCO_2$ to C_2H_5OH. The author's design focuses on attaining three discrete features: (i) The nanocomposites produce a positive charge locally on Cu ($Cu^{\delta+}$) to offer multi-active sites during $ERCO_2$; (ii) The evenly

View Article Online
DOI: 10.1039/D4YA00302K

dispersed tiny Cu_2S on Cu generate interfaces, as illustrated in Fig. 18b-g, between $Cu^{\delta+}$ and Cu in the zero-valence state Cu^0; and (iii) The uneven and stepped Cu-Cu_2S surface offers a spatially advantageous arrangement for C_2H_5OH production. Due to those structural features, a total FE of 90% to C_{2+} products (FE of 6% for C_2H_5OH and FE of 15% for C_2H_4) with a partial current density of 45 mA/cm^2 at -1.2V_{RHE} was attained in a H-cell configuration. According to the in-situ spectroscopy and DFT investigations, as illustrated in Fig. 18h-l, they attributed that the three characteristics of Cu-Cu_2S work together to improve CO_2 adsorption by enabling high electronic conductivity, (1) facilitate the adsorption of *CO intermediate on the Cu-Cu_2S surface, (2) lower the energy barrier for forming of the *COCO intermediate, and (3) makes the reaction path more thermodynamically viable for C_2H_5OH over C_2H_4. This study emphasizes the potential for commercializing alcohol and related product formation from CO_2 by proposing an effective method and the underlying mechanism for the significant increase of $ERCO_2$ to-C_2H_5OH conversion.

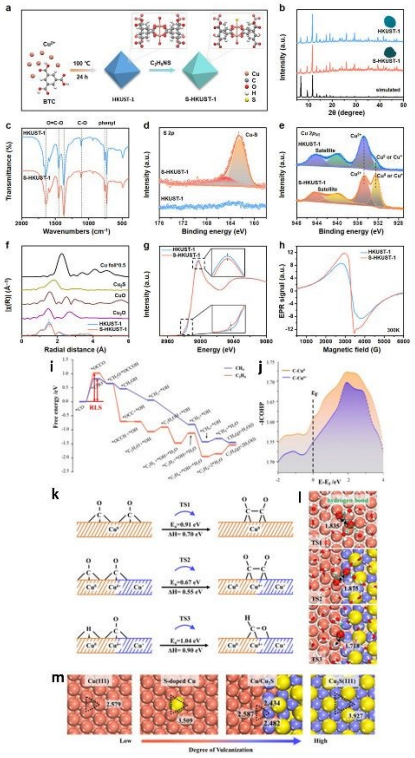

Fig. 17. (a) Schematic diagram of the preparation of S-HKUST-1. (b) XRD patterns of the prepared S-HKUST-1 and HKUST-1 precatalysts are well indexed to the simulated HKUST-1. The insets are digital photos of S-HKUST-1 (dark green) and HKUST-1 (blue). (c) FTIR spectra of S-HKUST-1 and HKUST-1 precatalysts indicate negligible differences. The XRD and FTIR results prove that the long-range ordered structure is not destroyed after S incorporation. d,e) High-resolution XPS spectra of S-HKUST-1 and HKUST-1 precatalysts in the d) S2p region, showing the characteristic Cu@S bonds in the S-HKUST-1 precatalyst and e) Cu2p region, showing the increased content of $Cu^{\delta+}$ or Cu^0 species. (f) FT of the EXAFS spectra and g) Cu K-edge XANES spectra of HKUST-1 and S-HKUST-1 precatalysts. The inset in (g) is the magnified image. The XAFS results in (f, g) prove the successful incorporation of local heteroatoms, which might be bonded to Cu atoms in MOFs. h) EPR spectra of the samples measured at 300 K. (i) Calculated free energy profiles for $ERCO_2$ to CH_4 and C_2H_4 over pure Cu(111) surface, indicating that the initial *CO hydrogenation and dimerization steps determine the CH_4 and C_2H_4 products distribution. (j) Integrated crystal orbital Hamilton populations (-ICOHPs) curves for Cu $Cu^{\delta+}$ –CO and Cu^0–CO bonds. (k) The reaction barriers together with enthalpies and (l) corresponding transition state configurations for *CO dimerization and hydrogenation over Cu(111) and Cu/Cu_2S surfaces, respectively. Yellow, red, grey, white, orange and blue balls refer to S, O, C, H, Cu^0 and $Cu^{\delta+}$ atoms, respectively. (m) Surface configuration (top view) of Cu-associated structures with different degrees of vulcanization. The distances between two neighbouring Cu atoms on different surfaces are given in b. (Reproduced on permission from [154]. Copyright, Wiley-VCH GmbH 2021)

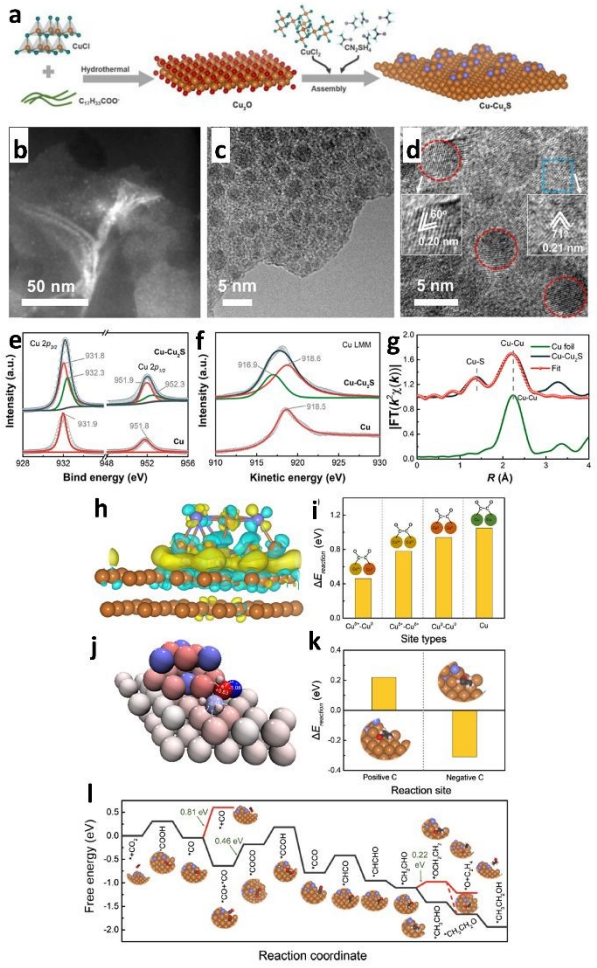

Fig. 18. (a) Schematic illustration for the synthesis of Cu-Cu_2S. Characterization of the Cu–Cu_2S sample. (b, c) TEM, (d) high-resolution TEM (HRTEM), (e) high-resolution Cu 2p XP spectra, (f) Cu LMM Auger spectra, and (g) Cu K-edge K2-weighted χ(k) function of Fourier transform extended X-ray absorption fine structure (EXAFS) spectra of the sample, where pristine Cu and Cu foil are used as controls in panels (e), (f), and (g), revealing that both Cu(0) and Cu(I) states are involved, respectively. Calculated $ERCO_2$ on Cu–Cu_2S. (h) DFT-calculated charge density difference of Cu–Cu_2S (the Cu and S atoms are in brown and violet, respectively; the yellow and cyan colours represent charge accumulation and depletion, respectively; the isosurface value is 0.002 e Å^{-3}). (i) Energy barrier ($\Delta E_{reaction}$) for two *CO forming one *OCCOvia C–C coupling at $Cu^{\delta+}$–Cu^0, $Cu^{\delta+}$–$Cu^{\delta+}$, and Cu^0–Cu^0 sites of Cu–Cu_2S and at the pristine Cu surface, where Cuδ+ and Cu0 of Cu–Cu_2S and Cu of pristine are in brown, red, and green, respectively, showing that the energy barrier at the $Cu^{\delta+}$–Cu^0 site of Cu–Cu_2S is lowest. (j) Bader charge of *CH_2CHO adsorbed on Cu–Cu_2S, where the colour ranging from blue to red indicates the negative to the positive charge of the atoms, respectively. (k) $\Delta E_{reaction}$ for hydrogenation on the positively charged C and negatively charged C of *CH_2CHO converting to CH_2CH_2O* and CH_3CHO*, respectively. (l) Calculated free energy for each step of the reaction pathway converting CO_2 to C_2H_5OH on Cu–Cu_2S. (Reproduced on permission from [155]. Copyright, ACS 2023)

Mosali et al.[156] developed an array of Cu_xZn_yS nanoparticles (Fig. 19a-l) with varying Cu: Zn compositions and electrochemically stabilized, resulting in SD- Cu_xZn_yS catalysts. The catalysts confirmed composition-dependent product selectivity during $ERCO_2$. Operating in an H-cell configuration, it was discovered that SD- Cu_xZn_yS catalysts with a higher copper content exhibited

significantly higher FE_{CH4} than their Zn-rich catalysts. In contrast, Zn-rich counterparts produced CO as the primary $ERCO_2$ product. The best composition of 1:1 Cu: Zn resulted in highly selective CH_4 as the main product, with an FE of 76±3% at -0.98V_{RHE}. The current density increased after switching to a flow cell arrangement for electrolyzing $ERCO_2$ in 1.0 M $KHCO_3$ or 1.0 M KOH electrolyte. However, the selectivity changed to produce syngas, with molar ratios of 2:3 to 3:2 for the formation of H_2/CO. This tendency holds irrespective of the applied potential, particularly in the 1.0 M KOH electrolyte. An ex-situ investigation revealed a significant reduction in CuS in electrocatalysts with higher copper content. In addition, pre-reduction of CuZnS catalysts and time-dependent observations showed the importance of copper's higher oxidation state and the interaction of partially reduced CuS and ZnS presence in the catalysts in attaining methane selectivity. These findings demonstrate that copper's oxidation state is crucial in determining selective product formation in copper-associated catalysts. Likewise, the same research group created S-derived copper-cadmium ($SD\text{-}Cu_xCd_y$) electrocatalysts earlier, where x and y denote the molar ratio of Cu/Cd) to assist in generating vital intermediates.[157] In 0.1 M $KHCO_3$ solution, the $SDCuCd_2$ catalyst observed 32% ethanol selectivity at a low overpotential of -0.89 V_{RHE}. They exhibited selective ethanol production at lower overpotentials with the best-performing SD-$CuCd_2$ electrocatalyst of Cu_3Cd_{10}alloy/Cu_2S/CdS phased composites, as illustrated in Fig. 19m and 19n.

Xi and colleagues[158] recently developed and built CeO_2/CuS (Fig. 20a-k) with a -0.5V_{RHE} overpotential for $ERCO_2$ to ethanol and a FE_{C2+} of 75% at -0.8V_{RHE}. During $ERCO_2$, they investigated catalysts' structural development, interactions, and activity sources, as illustrated in transmission electron microscopy (TEM) and high-resolution transmission electron microscopy (HRTEM) images (Fig. 20b-d). The fast electron movement route provided

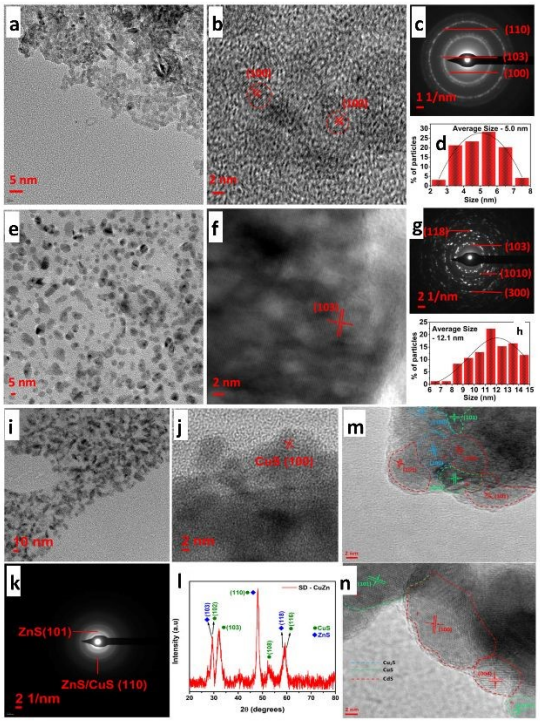

Fig. 19. a, e) TEM images, b, f) HR-TEM images, c, g) SAED pattern and d, h) particle size distribution of a-d) CuS and e–h) ZnS nanoparticles. (i) TEM images (j) HR-TEM images, (k) SAED pattern, (l) XRD powder pattern of SD-CuZn nanoparticles obtained upon pre-reduction at -0.80 V vs RHE in 0.10 M $KHCO_3$ solution saturated with CO_2. (Blue diamond (◆) represent the peaks corresponding to ZnS, and green circles (□) represent the peaks corresponding to CuS). (Reproduced on permission from [156]. Copyright, ELSEVIER 2024). HR-TEM images of (m) $CuCd_2S$; (n) Cu_2CdS showing boundary distributions of CdS, CuS and Cu_2S. (Reproduced on permission from [157]. Copyright, Wiley-VCH GmbH 2023)

by CeO_2 regions in catalysts prevents electron aggregation around Cu^+ sites, preserving Cu^+ sites during $ERCO_2$. The experimental in-situ studies and DFT calculations reveal that altering CeO_2 on CuS thermodynamically reduces the production energy for *COCHO compared to CuS nanoplates. The fast water molecule activation near CeO_2 speeds up the synthesis of *COCHO. As a result, the C-C coupling is accelerated via the *CHO route, providing CeO_2/CuS catalysts with exceptional electrocatalytic efficacy towards C_{2+} products. Wang et al.[159] proved that heterointerfaces of Bi/CeO_2/CuS nanohybids (Fig. 20l-s)can be advantageously employed as a highly efficient and selective catalyst for $ERCO_2$ to produce formate over a wide potential range. The nanohybrid demonstrated excellent activity at -0.9 V_{RHE}, with a formate efficiency of 88% and a current density of -17 mA/cm^2. The morphological analysis observed no change in the structure after a one-hour reaction at -0.9$V_{RHE,}$ and the FE of formate remained stable at that potential. The Bi/CeO_2/CuS heterostructure substantially decreases the formation energy barrier of OCHO* intermediates because, during electrolysis, Ce^{4+} rapidly suffers Ce^{3+} reduction, forming a conductive network of Ce^{4+}/Ce^{3+}, resulting in high activity and selectivity of $ERCO_2$ to formate. Overall, the system increased electron mobilization, stabilized Cu^+ species, and improved CO_2 adsorption and activation over the catalytic surface. Furthermore, sulfur boosts the transformation of OCHO* to formate.

Han et al.[160] employed the simple solution-phase method to synthesize a ternary metal-metal sulfide Bi-Cu_2S heterostructure electrocatalyst (Fig. 21a and 21b). Due to the high synergistic and interfacial effects between Bi and Cu_2S, the heterostructure observed a lower overpotential (240 mV) than Bi with an outstanding $FE_{formate}$ of >98% and 2.4 and 5.2 times higher partial current density than bare Cu_2S and Bi at -1.0V_{RHE}. According to the theoretical study, the HCOOH generation was aided by stabilizing the *OCHO intermediates over *COOH and *H due to the higher electron transfer rate between the Bi and Cu_2S interfaces (Fig. 21c-i).

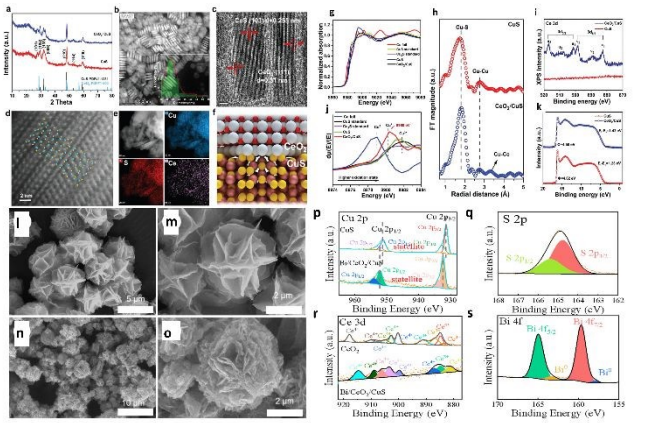

Fig. 20. Crystal structures and composition of CuS and CeO_2/CuS. a) XRD patterns CuS and CeO_2/CuS. b) TEM image of CeO_2/CuS. (inset: size distribution). c) HRTEM image of CeO_2/CuS. d) The HAADF-STEM image of CeO_2/CuS (inset: CuS 9 000 523. cif). e) The HAADF-STEM image and corresponding EDS element mapping of CeO_2/CuS. f) Structural representation of CeO_2/CuS, white: Ce atoms; red: O atoms; yellow: S atoms; gold: Cu atoms. Electronic structures of CuS and CeO_2/CuS. (g-i) X-ray absorption spectra for CeO_2/CuS, CuS catalyst, standard CuS, standard Cu_2S, and Cu foil. (g) Normalized Cu K-edge XANES. (h) the first derivative μ(E)/dE. (i) Fourier-transformed $k^2\chi(k)$ of CeO_2/CuS (lower panel) and CuS (upper panel). (j) Ce 3d XPS spectra. (k) UPS spectra. (Reproduced on permission from [158]. Copyright, Wiley-VCH GmbH 2023). SEM images of (l,m) CuS and (n,o) Bi/CeO_2/CuS. XPS patterns of Bi/CeO_2/CuS (p) Cu 2p, (q) S 2p, (r) Ce 3d, and (s) Bi 4f. (Reproduced on permission from [159]. Copyright, MDPI 2024)

View Article Online DOI: 10.1039/D4YA00412K

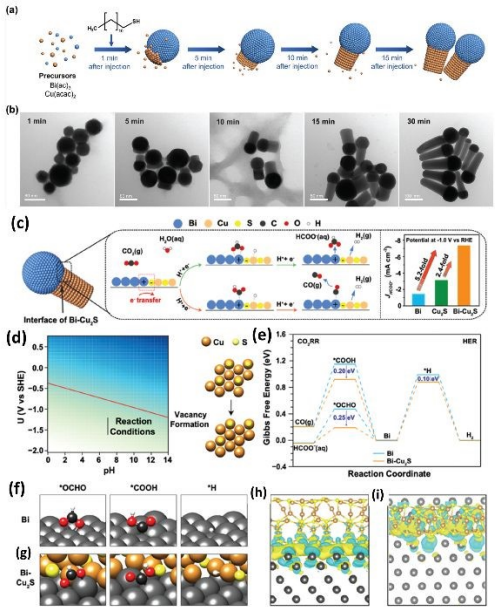

Fig. 21. (a) Schematic illustration of the nucleation and growth of the heterostructured Bi–Cu_2S nanocrystals. (b) TEM images of Bi–Cu_2S at different time intervals after introducing 1-dodecanethiol at 220 1C. (c) Proposed CO_2 reduction mechanism on the Bi–Cu_2S interfacial system. (d) The sulfur vacancy formation Pourbaix diagram. (e) Free energy diagrams of the $ERCO_2$ and HER on Bi (001) and Bi–Cu_2S model systems. Optimized geometry structures of key intermediates (*OCHO, *COOH, and *H) on Bi (001) and Bi–Cu_2S systems are shown in (f and g), respectively. (Dark grey, brown, yellow, black, red, and white spheres denote Bi, Cu, S, C, O, and H atoms, respectively.) (h and i) are the top and front views of the charge density difference for the Bi–Cu_2S interfacial surface, respectively. Cyan corresponds to an isosurface of -0.001 e $Bohr^{-3}$ and yellow to +0.001 e $Bohr^{-3}$. (Reproduced on permission from [160]. Copyright, RSC 2022)

Prasanna et al.[161] designed a rationally created novel heterostructure of CuS decorated NH^{4+} ions incorporated stable 1T-WS_2/WO_3 using simple hydrothermal methods followed by a reflux technique (Fig. 22a). The nanohybrid favoured reaction mechanism through *OCHO routs, which reduces (by obtaining $H^+ + e^-$) to $HCOO^-$ ($HCOO^-$ pathways) as the main product. Thus, CuS@1T-N-WS_2/WO_3 nanohybrids yielded 55.6% ± 0.5 at −1.3 V_{RHE} and a j_{geo} of −125.05 mA/cm^2. Interestingly, from their analysis, the intercalation of NH^{4+} ions with effective surfaces that donate WO_3 and accept protons from WS_2 stabilized the metallic 1T phase. Besides, an effective hydrogen spillover mechanism in the stable heterointerface of 1T-N-WS_2/WO_3 may provide kinetic support for CuS active centres, leading to notable improvements in product efficiency and selectivity (Fig. 22b).

Guo et al.[162] synthesized transition metal sulfides (TMS)-supported CuS catalysts with microflower-shaped frameworks via the facile hydrothermal approach for $ERCO_2$ to CO (Fig. 22c). They investigated the effect of doping TMSs (i.e., ZnS, Bi_2S_3, and MoS_2) with CuS on $ERCO_2$ performance. All the heterostructured catalysts, i.e., ZnS-CuS, Bi_2S_3-CuS and MoS_2-CuS, observed flower-shaped morphology, with the doped TMSs (i.e., ZnS, Bi_2S_3, and MoS_2) attached as microcrystals on the surface of petals. On the other hand, strong Cd^{2+} and Cu^{2+} interactions with S^{2-} caused CdS and CuS to aggregate and expand disorderly, forming incomplete sphere-like cage-shaped microstructures. Electrochemical experiments revealed that TMS-supported CuS catalysts outperformed pristine CuS in $ERCO_2$ activity, but their CO_2 conversion rate was reduced. Decorating CuS with MoS_2 observed a flower-shaped nanomorphology (Fig. 22d and 22e), enhancing the catalyst's CO selectivity from 72.67% to 83.20% at -0.6 V_{RHE}. With the increase in applied potential from -0.2 to -1.0 V_{RHE}, CO selectivity initially improved and then decreased, but the CO_2 conversion rate increased considerably from 0.2% to 21.9%. It has been observed that, during a 300-minute electrolysis at -0.6 V_{RHE}, the targeted MoS_2-CuS catalyst exhibited constant $ERCO_2$ activity, with CO selectivity improving in a limited range of 73.6% ~ 88.5% and j_{CO} stabilizing about 3.6 mA/cm^2. The authors attributed the increased selective CO formation linked to the synergistic effect of the generated GBs, undercoordinated S-vacancy, and edge-exposed Mo sites in boosting CO_2 activation, stabilizing *COOH adsorption, facilitating * CO desorption, and reducing the energy barrier of the potential-limiting step.

3.6 Heteroatom doping effect for improving electrocatalytic performance

Doping is widely regarded as an effective method for modulating the electronic structure of a catalyst through charge redistribution.[163,164] Doping different elements into the lattice of the pristine material can effectively modulate the electronic and physiochemical properties to fine-tune its electrocatalytic activity.[165,166] Also, heteroatom doping has little impact on crystal structure disruption, so the catalyst's main composition remains unchanged. It has been observed that the doping approach can increase the adsorption/desorption energy of the reaction intermediates.[167,168] The doping strategies are divided into metal and nonmetal doping, described below.

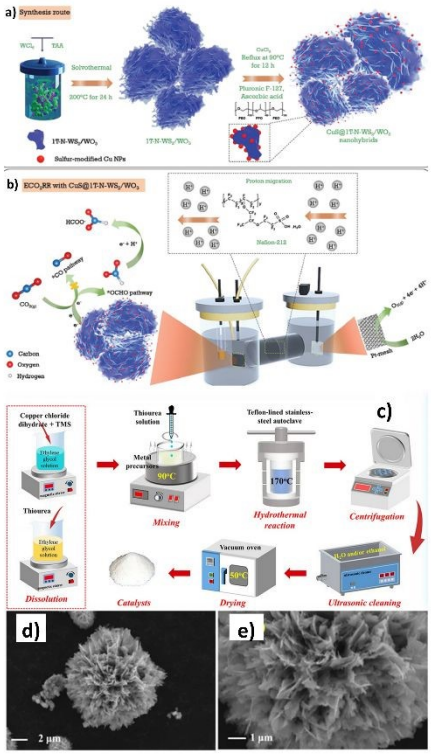

Fig. 22. (a) Schematic illustration of the synthetic process of 1T-N-WS_2/WO_3 and CuS@1T-N-WS_2/WO_3 nanohybrids using a simple solvothermal process and reflux method. b) Proposed schematic illustration of the $ERCO_2$ in an H-type cell. (Reproduced on permission from [161]. Copyright, Wiley-VCH GmbH 2023). (c) Schematic diagram of the synthesis procedures and formation of the pristine CuS and TMS-decorated CuS microflower-like structures; SEM images of the MoS_2-CuS catalysts (d) at a low magnification; (e) at a high magnification. (Reproduced on permission from [162]. Copyright, Springer Nature 2024).

3.6.1 Metal doping

Metal doping can significantly catalyze the C-C coupling during $ERCO_2$: Very Recently, Hu et al.[169] constructed Mo^{4+}-doped CuS nanosheet-assembled hollow spheres for $ERCO_2$ to ethanol in flow cell configuration. They revealed that doped with Mo^{4+} ion makes the mobility of the electron faster from Cu to S, optimizing the surrounding electrical conductivity and broadening the CuS binding sites, resulting in increased coverage of linear $*CO_L$ on the Cu site away from the Mo site and produces bridge $*CO_B$ on the Cu site near Mo site and activates asymmetric C–C coupling of $*CO_L$–$*CO_H$ for ethanol generation. Additionally, the highly electron-dense Cu site away from the Mo site favours the cleavage of Cu–O, promoting the hydrogenation of CH_3CH_2O* to ethanol. Moreover, the nanosheet-assembled hollow sphere structure and hydrophobicity of the Mo^{4+}-doped CuS-prepared GDE assisted the flow-cell procedure. The best $Mo_{9.0\%}$-CuS achieved the ethanol FE of 67.5% and $j_{Ethanol}$ of 186.5 mA/cm^2 at −0.6 V_{RHE} in a flow cell, with good stability for 26 h continuous operation. In this work, high valence transition metal ions are doped into Cu-associated sulfides to modify the coverage and configuration of related intermediates for ethanol production in a flow cell, thereby developing Cu-associated materials for converting $ERCO_2$ to ethanol. In another work, a Cu-doped Bi (CDB) nanosheet was created by reconstructing a CuS-Bi_2S_3 heterojunction precursor in situ (Fig. 23a).[170] The in-situ restructured of the as-synthesized CuS-Bi_2S_3 heterojunction precursor, as shown in Fig. 23b-g, resulted in one enhanced CDB catalyst with an industrially acceptable ampere-level current density and remarkable stability for the formate production (Fig. 23h-m). The CDB surface with a high concentration of electrons resulting from an increase in the Fermi level not only helped to stabilize the *OCHO intermediate but also successfully lowered the rate-determining step's reaction kinetic barrier, leading to the exceptional electrocatalytic activity of the CDB catalyst. At the same time, the more excellent selectivity to formate can be due to the reduced ΔG_{OCHO*} on the CDB surface relative to ΔG_{COOH*} and ΔG_{H*}. Furthermore, the effective antioxidation capability of CDB electrocatalyst allows it to exhibit outstanding stability beyond 100 hours at a high current density of 400 mA/cm^2 in MEA cells (Fig. 22n).

3.6.2 Nonmetal doping

Many studies have also focused on using nonmetal doping to tune the electronic structure of the electrocatalysts. Nonmetals such as N and S have significantly increased $ERCO_2$ catalytic activity. For example, Liang et al.[171] developed theoretical and experimental studies to investigate catalytic reactivity effects on N-doped Cu sulfides using the generalized morphology engineering principle of asymmetric metal pair sites, which promotes C-C coupling on electrode surfaces. First, a computational N-doped Cu_2S model layer featured electronically asymmetric $Cu^{\delta 1+}$-$Cu^{\delta 2+}$ ($0 < \boldsymbol{\delta}_1^+ < \boldsymbol{\delta}_2^+ < 1$) metal pairs evidenced by considering their non-uniform charge distribution. The asymmetric electronic structure led to distinct CO adsorption energies and the associated self-adjusting structures, which significantly lowered C–C coupling energy barriers. Later, they experimentally validated the computational hypotheses using XPS of Cu-N moieties within N-doped Cu_2S layers. In-situ FTIR spectroscopy confirmed linear *CO and *CO-CO adsorption configurations from the ≈2080 and 1920 cm^{-1} broad peaks, respectively. After N-doping, the catalytically C_2 faradaic efficiency can significantly be elevated to 14.72% due to the promotion of C–C coupling (Fig. 24a).

In another work, Li et al.[172] demonstrated the effective modulation of $ERCO_2$ pathways by designing and synthesizing three kinds of copper sulfide (Fig. 24b). Among all, they observed that SNC@Cu_2S (Cu_2S coated sulfur, nitrogen-co-doped carbon) without Cu vacancies displays a high FE for formate production. In contrast, the other two catalysts, SNC@Cu_xS and SNC@$Cu_{1.96}S$, with Cu vacancies, generated CO as the primary product (Fig. 24c-i). Firstly, the Cu vacancies present in $Cu_{1.96}S$ modify the S sites' electronic structures and significantly increase the energy barrier of H* formation. At the same time, the Cu vacancies generate the appropriate binding energy for the *COOH intermediate while attenuating the adsorbate-metal interaction. These advantageous characteristics, when combined, result in the favoured formation of CO over formate. Furthermore, the Cu vacancies lower charge transfer resistance, enrich the electronic structure of active sites and increase CO_2 adsorption capacity, enhancing the $ERCO_2$ activity of SNC@$Cu_{1.96}S$.

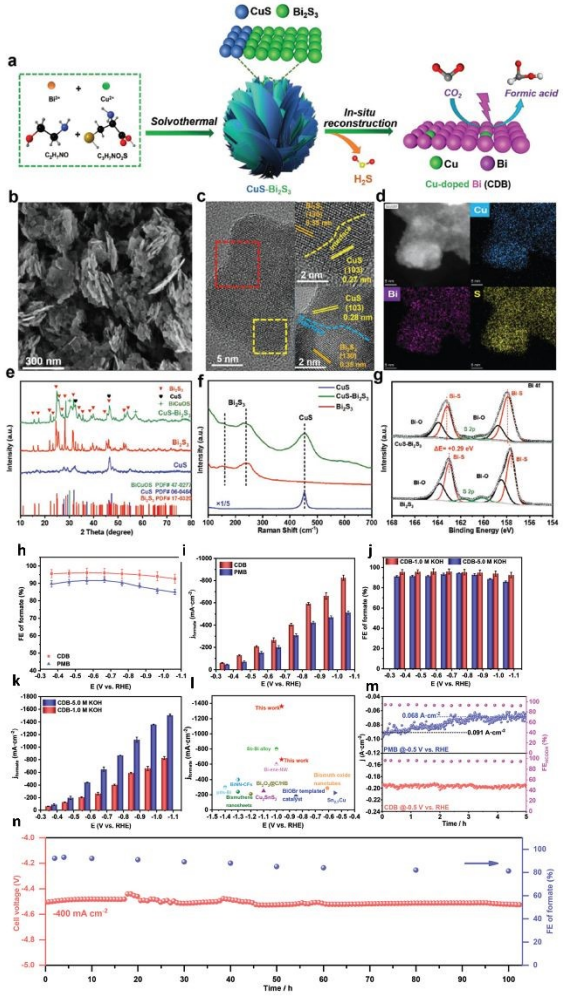

Fig. 23. a) Synthetic strategy of CuS-Bi_2S_3 nano-heterojunction precursor. b) SEM images of CuS-Bi_2S_3 nano-heterojunction precursor. c) HR-TEM images of CuS-Bi_2S_3 nano-heterojunction precursor. d) Corresponding elemental mapping images of S, Cu, and Bi elements. e) X-ray diffraction (XRD) patterns of CuS, Bi_2S_3, and CuS-Bi_2S_3. f) Raman spectrum of CuS, Bi_2S_3, and CuS-Bi_2S_3. g) The high-resolution XPS spectra of Bi 4f for Bi_2S_3 and CuS-Bi_2S_3. $ERCO_2$ measurements in the lab-made flow cell. h) FE of formate and i) formate partial current densities at different electrolytic potentials in 1M KOH electrolyte with CDB and PMB electrocatalysts. j) FE of formate and k) formate partial current densities of CDB electrocatalyst at different electrolytic potentials in 1M and 5M KOH electrolytes. l) Performance comparison of CDB electrocatalyst with the reported electrocatalysts towards $ERCO_2$ to formate in the flow cell. m) Stability test of PMB and CDB electrocatalysts at the potential of −0.5 V_{RHE} for 5 h. n) Continuous 100 h electrolysis in a 5 cm^2 MEA electrolyzer under a constant total current density of −400 mA/cm^2. The error bars in (f-h) represented the standard deviations of three independent measurements. (Reproduced on permission from [170]. Copyright, Wiley-VCH GmbH 2022).

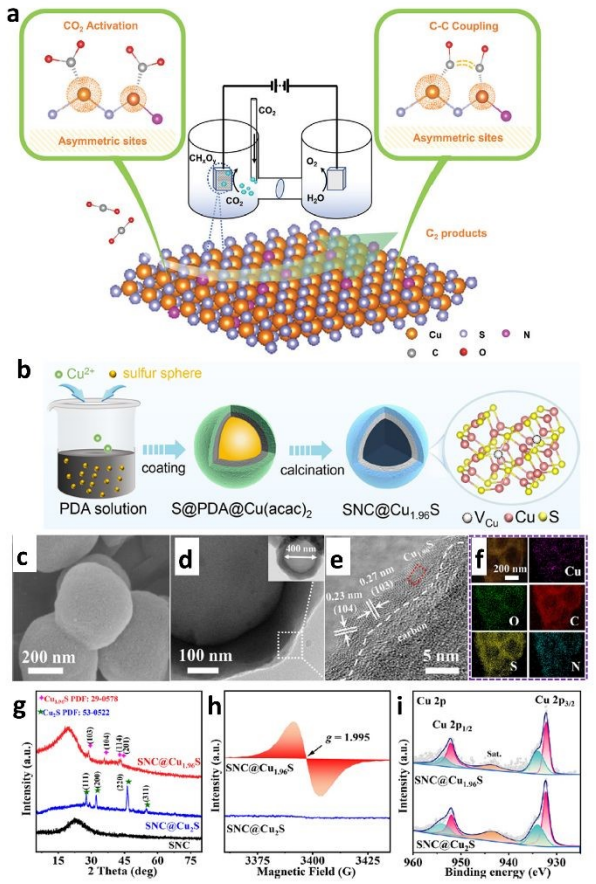

Fig. 24. (a) Illustration of the key hypothesis: The rate of C–C coupling by CO dimerization can be manipulated using structurally asymmetric Metal$^{\delta 1+}$- Metal$^{\delta 2+}$ pair sites ($0 < \delta_1^+ \neq \delta_2^+$). A well-ordered CuSx surface facet with surface Cu atoms adsorbs CO_2 molecules is shown. Dopant atoms introduce electronic asymmetries in Cu site pairs by adjusting electron-withdrawing/donating properties. Asymmetric CO chemisorption energies favor CO dimerization and hence $ERCO_2$ to C_2 products. By contrast, sites with even electronic distributions feature strong dipole-dipole repulsion forces during CO_2 activation, which seriously hinders CO dimerization. (Reproduced on permission from [171]. Copyright, Wiley-VCH GmbH 2022). (b) Schematic showing the synthetic process of SNC@$Cu_{1.96}$S. Characterization of Cu vacancies in SNC@$Cu_{1.96}$S. (c) SEM image, (d) TEM image, (e) HR-TEM image, and (f) the elemental mapping images of SNC@$Cu_{1.96}$S. (g) XRD patterns of SNC@$Cu_{1.96}$S, SNC@Cu_2S, and SNC. (h) EPR spectra and (i) Cu 2p XPS spectra of SNC@$Cu_{1.96}$S and SNC@Cu_2S. (Reproduced on permission from [172]. Copyright, ACS 2022)

Huang and his colleagues[173] synthesized Cu_2O-derived Cu catalysts doped with sulfur by immersing the Cu substrates in ammonium polysulfide solutions. Regarding cost, availability, longevity, and catalytic efficacy, the catalyst outperforms alternative materials for $ERCO_2$ to formate. Their XPS, ToF-SIMS, and μXRF analysis revealed a positive correlation between catalyst sulfur content and formate production. According to their findings, among all the prepared electrocatalysts, Cu-5000S with 2.7% atomic sulfur has satisfactory catalytic activity with a Faradaic Efficiency of 75% and current density of -13.9 mA/cm^2 at -0.9V_{RHE} for formate selectivity. Moreover, Cu-5000S exhibits outstanding stability for prolonged CO_2 reduction, as evidenced by its FE of formate maintained at approximately 75% for 12 hours. When sulfur doping was increased, formate production outpaced HER activity, as demonstrated by comparing the SRF-normalized $j_{formate}$ and j_{H2}. According to investigations of mechanisms, sulfur-doped Cu reduces the binding energy of *COOH intermediates for CO generation, facilitating the synthesis of HCOOH. This work demonstrates that sulfur doping is an effective strategy for enhancing the catalytic selectivity of Cu towards formate and expands the material choice for producing this commercially valuable fuel and chemical.

Li et al.[174] examined the influence of doping strategy in the $ERCO_2$ to ethylene of S-doped spherical coral-like CuO catalysts. With a current density of 15.5 mA/cm^2, the as-synthesized 5% S-CuO observed a good FE_{C2H4} of 48.4% at -1.3V_{RHE} compared to pure CuO. The 5% S-CuO also kept a consistent FE for C_2H_4 in long-term stability testing, with no appreciable drop in current density. The superior performance of 5% S-CuO was derived from the improved dynamic barriers of *CO intermediate dimerization at the Cu active site caused by S-doping, according to the experimental analysis and contact angle measurements. In addition, the hydrophobicity of the 5% S-CuO surface prevented accessible H_2O molecules from interacting, thereby preventing competitive HER.

Wang et al.[175] discovered various beginning morphologies of Cu_2S-X materials reduced to S-Cu_2O-X during $ERCO_2$ in 2022. The researchers found that the optimized electronic structure, aided by the S dopant and microstructure reconstruction, resulted in a large surface area, critical in improving the $ERCO_2$ performance and formate selectivity of the S-Cu_2O-X catalysts. In addition, as compared to $Cu(OH)_2$ and desulfurized Cu_2O materials, S-Cu_2O-X (X = 6, 10, and 14) catalysts showed significantly higher catalytic activity in the formation of formate (60%-70%). S-Cu_2O-14 catalyst demonstrated a partial current density of 16 mA/cm^2 at 1.0 V_{RHE} and FE of 67.2% for formate selectivity with a stability of 20 h among all evaluated electrocatalysts. DFT studies demonstrated that S-doped Cu(111) and S-vacancy (V_s) species promoted COOH* or OCHO* intermediates, which accelerated selectivity towards HCOOH pathways.

Recently, Zhang et al.[176] showed that S-doped Cu derived from hierarchical hollow-liked CuS polyhedron (CuS-HP) nanostructures synthesised from MOF significantly improve $ERCO_2$ performance in neutral pH water environments (Fig. 25a-j). According to their findings, during electrolysis, the CuS-HP was gradually transformed into an S-doped Cu as the reduction process went on. The in-situ formed electrocatalyst was performed with a stability of 36 hours at a $j_{formate}$ of 16 mA/cm^2 at -0.6 V_{RHE} with a FE of >90%. DFT study indicates that the Cu (111) facet in S-doped Cu lowers formate activation energy barriers while inhibiting HER while the reaction intermediates remain unchanged. This work comprehensively explains the mechanisms for improving formate selectivity in CuS electrode materials. Deng et al.[177] have experimentally and theoretically demonstrated that Sulfur-doped Cu catalyzes the $ERCO_2$ to formate. They synthesized an Active CuS_x (AC-CuS_x) catalyst, which exhibited a high FE of 75% and a partial current density of 9 mA/cm^2 at -0.9 V_{RHE} toward formate production (Fig. 25k-m). It was discovered that sulfur dopants were the key to the increased formate production on the AC-CuS_x surfaces. Operando Raman spectroscopy found that S dopants on the catalyst inhibited the CO intermediates formation during $ERCO_2$, which elucidates the lower FE for other products (i.e., CO, hydrocarbons, and alcohol formation). DFT calculations validated the Raman band assignments. They observed that the adsorption strengths of adsorbed HCOO* were modified by the presence of sulfur on the copper surface, which supported the formation of formate while inhibiting the formation of *COOH, the CO intermediate.

View Article Online
DOI: 10.1039/D4YA00302K

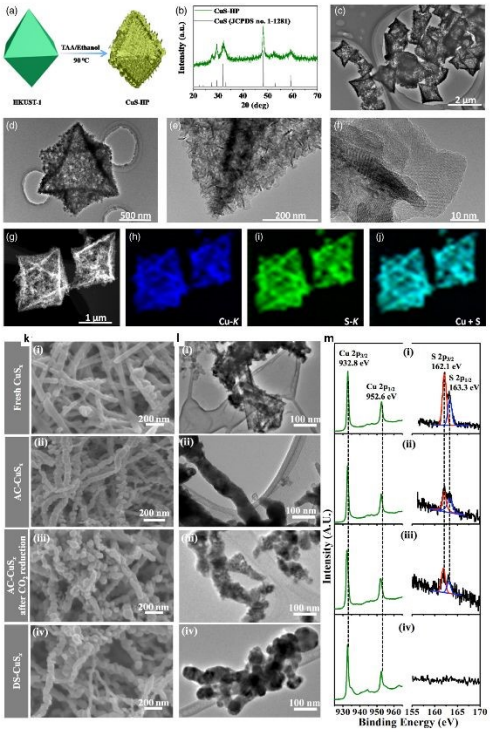

Fig. 25. Structural characterization of CuS-HP. (a) Schematic illustration of the synthetic process. (b) XRD pattern. (c–f) TEM images. (g–j) HAADF-STEM image and corresponding EDS elemental mapping images. (Reproduced on permission from [176]. Copyright, Chinese Chemical Society 2021). (k) SEM images, (l) TEM images, and (m) XPS spectra of (i) fresh CuS_x sample, (ii) AC-CuS_x sample, (iii) AC-CuS_x samples after 40 min of $ERCO_2$ in 0.1 M $KHCO_3$ at −0.85 V_{RHE}, and (iv) DS-CuS_x sample. (Reproduced on permission from [177]. Copyright, ACS 2018)

3.7 Catalyst support material for improving electrocatalytic performance

Supporting materials significantly impact the catalytic performance of electrocatalytic materials. In particular, TMD NSs show promise as a supporting material.[178,179] Composite catalysts have high catalytic performance due to the synergistic interaction of TMDs, supporting materials, and electrocatalysts.[180,181] Kahsay et al.[182] successfully deposited copper sulfide nanoparticles onto thermally synthesized copper oxide using a simple and facile SILAR method and examined its catalytic activity for $ERCO_2$ (Scheme 1 in Fig. 26). The modified nanocomposites exhibited high selectivity for formate formation at low overpotential. Remarkably, maximum faradaic efficiency of 84% and enhanced partial current density of −20 mA/cm² were obtained at an overpotential of -0.7V_{RHE}. It was observed that Copper sulfides undergo phase changes during $ERCO_2$, which can contribute to the enhanced electrocatalytic activity. As a result, together with copper oxides, a catalytic synergy is created in the composite, and more favourable adsorption sites are generated to facilitate the $ERCO_2$. This study paves the way to controlling the composition-selectivity relationship using a facile and scalable catalyst synthesis approach. Also, Li et al.[183] produced extremely porous Cu_2O/CuS nanocomposites, as evidenced by X-ray diffraction (XRD), Raman spectra and scanning electron microscope (SEM) from the Fig. 26a-i, observed better formate generation FE of 67.6% at a j_{HCOOH} value of 15.3 mA/cm² at -0.5V_{RHE} in $ERCO_2$. More significantly, with the same applied potential, the current density remained unchanged for at least 30 hours with an average FE of 62.9%. DFT modelling showed that CuS (110) facets favour HCOOH over CO, with substitutional surface O_S or vacancy V_S species expected to result in lower onset potentials and increased catalytic activity, with both COOH*- and OCHO*-mediated $ERCO_2$ routes predicted to be involved. As a result, it increases the yield of HCOOH formation with a better current density than the Cu, CuS, and Cu_2O electrocatalysts.

View Article Online
DOI: 10.1039/D4YA00302K

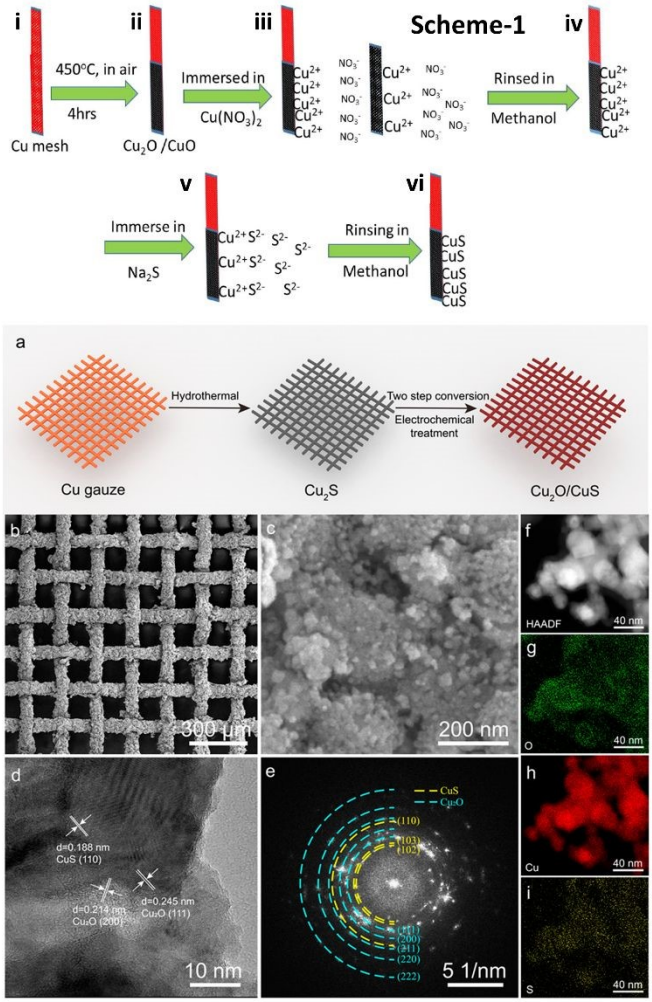

Fig. 26. Scheme 1: Illustration of thermal oxidation and SILAR growth: (i) Copper mesh before thermal oxidation, (ii) Cu_2O/CuO grown on copper mesh, (iii) adsorption of Cu^{2+} and NO^{-3} and the formation of an electrical double layer, (iv) rinsing (I) removes excess unabsorbed Cu^{2+} and NO^{3-}, (v) reaction of S^{2-} with pre-adsorbed Cu^{2+} ions to form CuS, and (vi) rinsing (II) to remove excess and unreacted species and form the solid solution CuS on surface of the Cu mesh/Cu_2O/CuO. (Reproduced on permission from [182]. Copyright, Springer 2019). (a) Schematic illustration of the synthesis of Cu2O/CuS nanocomposites. (b, c) SEM images of Cu_2O/CuS nanocomposites grown on a copper gauze collected at different magnifications. (d) HR-TEM image collected from a representative Cu_2O/CuS particle. (e) Corresponding FFT image of (d). Blue and yellow dashed lines highlight the diffraction rings of polycrystalline Cu_2O and CuS particles, respectively. (f–i) HAADF-TEM image of Cu_2O/CuS nanocomposites and the corresponding mapping images of elements O, Cu, and S. (Reproduced on permission from [183]. Copyright, ACS 2021).

Table 1 A current overview of Cu/S-associated catalysts for $ERCO_2$

Products	Electrocatalysts	Method of Synthesis	Potential (V_{RHE})	Electrolyte used	Cell	Partial Current density (mA/cm^2)	Faradaic Efficiency (%)	Stability (h)	Ref.
HCOOH	**Sulfur-modified Cu_2O**	Wet chemistry approach	-0.9	0.1 M $KHCO_3$	H-type Cell	260 ± 16	≈90%	80	99
C_2H_4	**Cu-s**	Electrochemical Reduction	-1.2	0.1 M $KHCO_3$	H-type Cell	40.8	68.6	8	100
HCOOH	**PTFE-coated CuS/BM**	one-step chemical bath process	-0.7	0.5 $mol \cdot L^{-1}$ $KHCO_3$	H-type Cell	50	70	1.5	101
CO	**Hollow-shaped CuS Microcubes**	Galvanic replacement technique	-0.16	0.5 M $KHCO_3$	H-type Cell	-	32.7	10	104

View Article Online
DOI: 10.1039/D4YA00302K

HCOOH	**Hollow ordered porous copper sulfide cuboctahedra**	Hard templating strategy	-1.1	0.1 M $KHCO_3$	H-type Cell	7.8	70.3	26	108
C_2H_4	**Copper sulfide film consisting of nanoparticles**	Thermal decomposition	-0.13	1 M $KHCO_3$	H-type Cell	≈0.08 (total)	-	-	109
HCOOH	**Cu_2S over Copper foam**	Electrochemical deposition	–2.0 V (vs Ag/Ag+).	0.5 mol L^{-1} $BmimBF_4$	H-type Cell	5.3	85	6	110
CH_4	**CuS/Ni foam**	Hydrothermal method	-1.1	0.1 M $KHCO_3$	H-type Cell	7.32 (total)	73.5±5	60	111
HCOOH	**CuS nanoflowers**	Ethylene glycol solvothermal method	-0.8 to ~ -1.0	0.1 M $KHCO_3$	H-type Cell	≈6.5	~52	2	117
HCOOH	**$Cu_{1.81}S$@MWCNT-600-OD**	Two-step coupling approach	-0.67	0.5 M $KHCO_3$	H-type Cell	3.75 (total)	82	20	119
HCOOH	**Cu_2S@C**	Liquid phase sulfidation	-0.78 ± 0.02	0.5 M KCl +0.5 M $KHCO_3$	H-type Cell	1.5 (Total)	12	5	120
CO	**CuS catalyst thiourea precursors**	Hydrothermal synthesis	-0.51	0.1 M $KHCO_3$	H-type Cell	-	72.67	5	
HCOOH	**Cu_2S Nanocrystals**	Electrochemically driven cation exchange method (ED-CE)	-0.9	0.1 M $NaHCO_3$	H-type Cell	19	87.3	9	122
HCOOH	**Cu_2S**	ED-CE	-0.2	0.05 M K_2CO_3	H-type Cell	-	≈70	16	
CO	**S-derived Cu-Sb**	Heat-up colloidal nanoparticle route	-1.0	1 M $KHCO_3$	Flow Cell	37.6	80.5	24	124
HCOOH	**S-CNWs**	Chemical oxidation followed by Solvothermal reaction	−0.59	0.25 M $KHCO_3$	H-type Cell	≈10	~60	2	125
HCOOH	**Submicron-sized Cu−S**	Solvothermal approach	-0.8	0.1 M $KHCO_3$	H-type Cell	≈10 (total)	80	12	128
HCOOH	**CuS_x nanoparticles**	Dipping	-0.6	0.1 M $KHCO_3$	H-type Cell	2.5	72	72	129
HCOOH	**S-Cu_2O/Cu**	Hydrothermal reduction followed by in situ reconstruction	−1.0	0.1 M $KHCO_3$	H-type Cell	5	70	6	134
HCOOH	**CuS 811 derived S-doped Cu_2O**	Surfactant-free double-replacement reaction		0.1 M $KHCO_3$	Flow cell	321	80	33	135
Alcohols (Ethanol+ Propanol)	**CSVE-Cu**	Solution-phase growth	–0.95	1.0 M KOH	Flow Cell	126	31.6	16	142
propanol	**DSV-engineered CuS_x**	Lithium tuning approach	−1.05	0.1 M $KHCO_3$	H-type Cell	9.9	15.4 ± 1	10	143
HCOOH	**SnO_2@C onto Snowflake-like Cu_2S**	Hydrothermal method	−1.0	0.1 M $KHCO_3$	H-type Cell	15.6	88	50	146
HCOOH	**CuS/SnO_2-S derived Cu/Sn/$Cu_{6.26}Sn_5$ catalysts**	Redox reaction	−0.8	0.5 M $KHCO_3$	H-type Cell	≈18.8	84.9	10	147
CO	**SnO_2 confined on CuS nanosheets**	One-pot precipitation synthesis	-1.0	0.1 M $KHCO_3$	H-type Cell	15.24	>85	24	150
HCOOH	**Cu_2SnS_3 nanoplates**	Step-growth approach	−1.2	1 M $KHCO_3$	Flow Cell	181	72.4	3	151
CO	**$CuInS_2$ hollow nanostructures**	Template-free approach	−0.7 & −1.0	0.1 M $KHCO_3$	H-type Cell	≈13 (Total)	82.3	4	152
HCOOH	**Graphdiyne/copper sulfide**	Hydrothermal followed by in-situ growth	−0.9	0.1 M $KHCO_3$	H-type Cell	65.6 (total)	70	4	153
C_2H_4	**S-HKUST-1**	Local sulfur doping strategy	-1.94	1.0 M KOH	Flow Cell	228	57.2	8	154
Ethanol	**Cu_2S Nanocrystal-Decorated Cu Nanosheets**	Hydrothermal followed by self-assembly	-1.2	0.1 M $KHCO_3$	H-type Cell	j_{C2H5OH} = 20.7	46	20	155
CH_4	**Cu_xZn_yS nanoparticles**	Seed-mediated growth method	−0.98 V_{RHE}	0.1 M $KHCO_3$	H-type Cell	$j_{methane}$ = 4.58	76	5	156
Ethanol	**SD – $CuCd_2$**	Co-precipitation	-0.8	0.1 M $KHCO_3$	H-type Cell	0.6	32	6	157
C_{2+} Products	**CeO_2-modified CuS nanoplates**	Self-assembly method	-0.9	1M KOH	Flow Cell	J_{C2+} = 75.3	75	180	158
HCOOH	**Bi/CeO_2/CuS**	Solvothermal process	-0.9	0.5 M $KHCO_3$	H-type Cell	17 (total)	88	6	159

View Article Online
DOI: 10.1039/D4YA00302K

HCOOH	**Heterostructure Bi–Cu_2S nanocrystals**	One-pot solution-phase approach	−1.0	0.1 M $KHCO_3$	H-type Cell	~17	>98	10	160
HCOOH	**CuS@1T-N-WS_2/WO_3**	A facile solvothermal process followed by a reflux strategy	-1.3	0.5 M $KHCO_3$	H-type Cell	125.05	~55.6	2	161
CO	**MoS_2-CuS**	Hydrothermal approach	-0.6	0.1 M $KHCO_3$	H-type Cell	3.6	83.2%	5.55	162
Ethanol	**Mo^{4+}-doped CuS nanosheet-assembled hollow spheres**	one-step solution-phase approach	-0.6	1.0 M KOH	Flow Cell	$J_{ethanol}$ = 186.5	67.5	14	169
HCOOH	**Cu-doped Bi derived from CuS-Bi_2S_3**	Solvothermal followed by in-situ reconstruction	−0.86	1 M KOH	MEA Cell	1132	90	100	170
C_2H_4	**N-doped Cu_2S thin layers**	Annealing process	-0.98	0.1 M $KHCO_3$	H-type Cell	~2.6	14.72	0.25	171
CO	**SNC@$Cu_{1.96}S$**	Surface coating and calcination	−0.84 V_{RHE}	0.5 M $KHCO_3$	H-type Cell	37.2	85.2	13	172
HCOOH	**Cu-5000S**	Electrochemical deposition	-0.8	0.1 M $KHCO_3$	H-type Cell	13.9	≈75	12	[illegible]
C_2H_4	**sulfur-doped spherical coral-like CuO**	Local sulfur doping strategy	-1.3	0.1 M $KHCO_3$	H-type Cell	15	48.4	20	[illegible]
HCOOH	**S-Cu_2O-14**	Hydrothermal sulfurization method followed by electrochemical reduction process	−1.0	0.1 M $KHCO_3$	H-type Cell	16.3	67.2	20	175
HCOOH	**CuS hollow polyhedron derived from MOF**	MOF self-sacrificial template method	-0.6	0.5 M K_2SO_4 aqueous solution	H-type Cell	≈16	>90	36	[illegible]
HCOOH	**AC-CuS_x**	Pulsed electrochemical deposition	-0.9	0.1 M $KHCO_3$	H-type Cell	9	75	3	[illegible]
HCOOH	**CuS deposited onto thermally prepared Cu_2O/CuO heterostructure**	Thermal oxidation followed by SILAR	-0.7	0.1 M $KHCO_3$	H-type Cell	20	84	2.5	182
HCOOH	**Cu_2S/Cu_2O nanocomposites**	Hydrothermal approach and electrochemical treatment	-0.9	0.1 M $KHCO_3$	H-type Cell	12.3	67.6	30	183

4. Theoretical studies of Cu/s-associated $ERCO_2$ Catalysts

As their knowledge of electrocatalysis grows, scientists are no longer satisfied with investigating macroscopic phenomena in experimentation; instead, they are exploring the complex microscopic world to gain insight into the mechanism underlying electrocatalytic reactions. This effort is significant for the design and evaluation of highly efficient electrocatalysts. The rapid development of supercomputers has resulted in significantly greater computational speed and performance, enhancing theoretical calculations. In addition, modelling and simulated environments are now closely consistent with the experimental surroundings, resulting in accurate results. [184–186] Nowadays, computational models are used not only to shed light on experimental phenomena but also to direct research strategies and the development of efficient electrocatalysts.[184–186]

Inspired by this, Henrique et al. discuss theoretically how the tuning ratio of the Cu/S on 2D CuS_x nanomaterials influenced the $ERCO_2$ performances.[187] Their findings demonstrate that the adsorption modes and strength of $ERCO_2$ intermediate on CuS_x monolayers vary considerably based on the Cu/S ratio, resulting in different catalytic activity. For instance, $CuS_{0.5}$ catalytic systems showed high onset potential values even though the system was slightly more favourable for reduction toward HCOOH than CO. The CuS system's minimal onset potential for CO or HCOOH suggests that the system could potentially act as a catalyst to form $2e^-$ products. In comparison, $CuS_{1.5}$ revealed minimal onset potential values for the generation of CO, HCOOH, CH_4, and CH_3OH, that are, respectively, 0.19, 0.19, 0.53, and 0.53 (V_{RHE}) less than the values determined for Cu(111). The simulation also revealed that, on $CuS_{1.5}$, the reaction toward CH_4/CH_3OH was limited by the *CO → *COH formation, while on both the $CuS_{1.5}$ and CuS surfaces, the CO_2 → *COOH generation was the potential determining step for CO and HCOOH formation. According to the calculation, the facile *CO desorption on CuS surfaces could restrict the formation of CH_4/CH_3OH. Therefore, methods for breaking the *CO and *COOH or *CHO/*COH interactions' linear scaling could be investigated as well in order to enhance most of these systems, while CuS's performance as a catalyst for the production of CH_4 and CH_3OH could be improved by simply increasing the CO adsorption strength. In summary, their DFT calculation discovered that increasing the sulfur content in 2D copper sulfide materials promotes CO and HCOOH formation at lower applied potentials and facilitates methane and methanol production. Although these outcomes seem promising from a thermodynamic standpoint, more research into the processes' kinetic behaviour via the most promising systems, considering defect creation under operating conditions, and more research examining additional reaction pathways are essential in strengthening the concept of these systems as potential electrocatalysts.

Another group proposed experimentally supported theoretical simulation to investigate the mechanism of $ERCO_2$ on S-modified Cu electrocatalysts for HCOOH selectivity.[188] They discovered that the surrounding environment and symmetry of the remaining sulfur atoms greatly influence their stability. Most sulfur exists in somewhat unstable

forms that satisfy the strong CO* surface-enhanced infrared absorption spectroscopy signal and the experimentally confirmed negative XPS shift. From the $ERCO_2$ energy graphics, it was revealed that these types of S cannot immediately promote formic acid generation; instead, they produce a highly dominant CO* and have a large CO* adsorption capacity. However, the study discovered that the sulfur atoms' strong CO* adsorption improves the CO* coverage to an almost four times higher level than on a bare Cu. With such a dense CO* coverage, specific surface reactive sites are restricted, resulting in a solution-phase CO_2 reduction pathway leading to the formation of highly selective HCOOH. Also, it has been found that CO* can considerably stabilize residual S, and their adsorption and associated electronic structure modulation studies have revealed the source of CO* adsorption improvement. Lastly, the group proposed a synergy between residual S and CO* dominating the HCOOH formation in $ERCO_2$ using experimental findings from published research and their DFT calculations.[118,177] These findings offer novel insights into the fundamental role of atomic sulfur in the selective formation of $ERCO_2$ products and intermediates on metallic Cu electrodes. Advanced characterization techniques, i.e., in situ/operando studies[189] and computational approach,[190,191] must be correlated to better understand the structure-stability-efficiency connections of electrocatalysts. This connection is also essential because of the high selectivity of these catalysts regarding particular catalytic processes and product generation.

5. Perspectives of Cu/s-associated $ERCO_2$ Catalysts

The catalyst's nanostructure, porosity, morphology, stability, surface area, and particle size influence $ERCO_2$ by affecting the adsorption and desorption of CO_2 molecules. These changes in adsorption and desorption processes lead to different products. In addition to the several modification strategies, the performance of Cu/S-associated nanomaterials towards $ERCO_2$ is strongly connected with several other factors. This section highlighted the novelty aspects related to Cu/S-associated nanomaterials.

Controlled morphology is critical for understanding the structure-activity relationships of Cu/S-associated nanomaterials in $ERCO_2$ catalysis. For example, Cu/S-associated nanomaterials have been developed with various nanoscale morphologies, including nanoarrays,[110] cubes,[104] ultrathin nanosheets,[150] hollow polyhedrons,[176] and hierarchical structures.[150] Also, it is to be noted that the morphology and $ERCO_2$ performance varies among Cu/S-associated nanomaterials due to the precursor effect.[121] The morphology-related characterization studies showed that different sulfur source precursor materials have different solubility and rates of release during hydrothermal synthesis, resulting in diverse surface morphologies at the end.[121] Several of these catalysts also have highly porous frameworks,[108] aiding electrolyte permeability. Moreover, a greater surface area might offer more multi-active sites, which is also advantageous in producing an optimal nanostructure for improved $ERCO_2$ activity.[151153]

Notably, the phase engineering approach also has a vital role in $ERCO_2$. For example, phase changes in Cu/S-associated nanomaterials are observed due to S leaching during $ERCO_2$. For instance, during the reduction process, XPS and HRTEM analysis observed that thermodynamically unstable CuS undergoes phase changes to metallic Cu, CuO, or Cu_2O.[117] For example, Shinagawa et al. employed XPS with SAED studies for the post-electrolysis sample. The group observed that during $ERCO_2$, S-modified materials lose excess sulfur irrespective of initial sulfur concentration due to the cathodic environment, resulting in modification of particle size and the co-existence of Cu_2S and Cu metal, significantly interfering with the electrocatalyst's activity.[128] Zhao and group[111] performed XPS and HRTEM to demonstrate CuS nanosheets undergo partial reduction to metallic Cu, and the metallic Cu phase is partially oxidized to CuO after $ERCO_2$. Zhang et al.[176] also did XPS and revealed that the CuS-HP synthesized from HKUST-1 was transformed to Cu(S) with a minimal $S^{\delta-}$ ($0 \le \delta \le 2$) and metallic Cu. This study revealed that although Cu(S) has minimal S concentrations, the polyhedron structures offer high activity and stability during the $ERCO_2$. As a result, in situ reconstruction of CuS in $ERCO_2$ promotes the $ERCO_2$ activity and product selectivity.

Utilizing highly conducting substrates to load the copper sulfides, such as copper oxide,[182] carbon-based materials,[119] and highly porous 3D foams,[110] improves electron conduction and gives more electrocatalytic active sites. Notably, forming copper sulfides-conducting substrate bonds improves catalyst stability, resulting in a longer lifetime. [119]

Other techniques for increasing catalytic activity include the compositional changes of bi-metallic sulfides in comparison to mono-metallic sulfides to generate a heterostructure capable of providing synergistic coupling,[160] interfacial phenomena,[161] and defect-rich structures[142] to maximize the benefits of metal and sulfide. The number of exposed active sites can be increased, and $ERCO_2$ performance can be improved through heterostructure engineering strategies by doping highly functional single-metal nanoparticles[169] and non-metal[171] on metal sulfides. Also, constructing heterostructures can improve $ERCO_2$ efficiency by adjusting the interfaces and electrical states and offering more active sites. So, lower onset potential, increased cathodic current, higher TOF, and lower Tafel slope values can be obtained during the $ERCO_2$ process. [187]

Furthermore, the $ERCO_2$ performance varies across Cu/S-associated nanomaterials based on their S content or S-vacancy concentration. Vacancy creation through defect engineering techniques, i.e., S-vacancy[162] and Cu-vacancy[172], can shift the product selectivity of $ERCO_2$ to C_{2+} products by modifying the electronic structure of S and Cu sites in Cu/S-associated nanomaterials.

Table 2 A overview of other Cu-associated $ERCO_2$ catalysts

Electrocatalysts	Main Products	Potential (V_{RHE})	Electrolyte used	Cell	Current density (mA/cm^2)	Faradaic Efficiency (%)	Stability (h)	Ref.
Single Cu atom	**Acetone**	-0.76	0.1 M $KHCO_3$	H-type Cell	1.0	36.7	5	192
TS-Cu	**Ethylene**	3.5	1M KOH	Flow Cell	800	72	200	193
dCu_2O/Ag2.3%	**Ethanol**	-0.87	1M KOH	H-type Cell	326.4	40.8	12	194
Cu-NC	**Ethanol**	-1.01	0.1 M $KHCO_3$	H-type Cell	-	18.4	8	195
Cu_2O/NCS	**Ethylene**	-1.3	0.1 M $KHCO_3$	H-type Cell	-	24.7	4	196

View Article Online
DOI: 10.1039/D4YA00302K

CuN_4	**Ethanol**	-1.2	0.1 M $KHCO_3$	Flow Cell	16.2	55	1	197
Cu_1Ni_2@N-MWCNT	**Formate**	-0.53	0.1 M $KHCO_3$	H-type Cell	3.0	90	10	198
Cu-doped carbon xerogel	**Methane**		0.1 M $KHCO_3$	H-type Cell	-		5	199
Cu-nanoparticles	**Formate**	-1.0	0.1 M $KHCO_3$	H-type Cell	6.53	54	12	200
GO-VB6-Cu-2	**Ethanol**	-0.250	0.1 M $KHCO_3$	H-type Cell	7.452	56.3	24	201
Cu–N–C	**Carbon mono oxide**	-0.7	0.1 M $KHCO_3$	H-type Cell	3.61	92	60	202
Cu_2O@Cu-MOF	**Methane**	-1.71	0.1 M $KHCO_3$	H-type Cell	8.4	79.4	1	203
PcCu–Cu–O	**Ethylene**	-1.2	0.1 M $KHCO_3$	H-type Cell	7.3	50	4	204
$Cu_{90}In_{10}$/C	**Carbon mono oxide**	-0.75	0.1 M $KHCO_3$	H-type Cell	9.85	85	4	205
CuO/CuTCPP	**Formic Acid**	-1.65	0.5 m $EMIMBF_4$	H-type Cell	4.5	85.2	5	206
Cu(111)@Cu-THQ	**Ethylene**	-1.4	0.1 M $KHCO_3$	H-type Cell	14.3	42	8	207
CuZn	**C_{2+}**	-1.0	0.1 M $KHCO_3$	H-type Cell	1.5	25	7	208
Cu@Cu_xO	**C_{2+}**	-1.78	0.1 M $KHCO_3$	H-type Cell	150	70	20	209
Cu–Sn	**Carbon monoxide**	-0.7	0.1 M $KHCO_3$	H-type Cell	4.5	90	12	210
Cu_3N-derived Cu nanowires	**C_2**	-1.0	0.1 M $KHCO_3$	H-type Cell	-50.6	86	28	211
CuO-derived Cu	**C_{2+}**	-0.48	KH_2PO_4	H-type Cell	-210	9.6	1	212
Cu_v–Cu_2O	**Ethylene**	-0.76	0.1 M $KHCO_3$	H-type Cell	15.7	51	10	213
Cu–Zn	**Carbon monoxide**	-1.1	0.1 M $KHCO_3$	H-type Cell	4.3	74	4	214
Cu@$Cu_2(OH)_3NO$	**Ethylene**	-1.2	0.1 M $KHCO_3$	H-type Cell	80	31.8	20	215
Cu_2O-derived Cu/$PdCl_2$	**Ethylene**	-1.0	0.1 M $KHCO_3$	Flow cell	-	30.1	8	216
Cu_2O films	**C_2**	-0.99	0.1 M $KHCO_3$	H-type Cell	-52	39	1	217
Cu_2O-derived Cu particles	**Ethylene**	-0.98	0.1 M $KHCO_3$	H-type Cell	-13.3	43	1	218
Branched CuO nanoparticles	**Ethylene**	-1.0	0.1 M $KHCO_3$	H-type Cell	-22.0	53	12	219
Cu–Pd Alloy	**Carbon monoxide**	-0.9	0.1 M $KHCO_3$	H-type Cell	-	87	5	220
Cu–Pt Alloy	**Methane**	-1.6	0.1 M $KHCO_3$	H-type Cell	0.598	21	0.5	221
CuMgAl LDH	**Acetic Acid**	-0.4	0.1 M $KHCO_3$	Flow Cell	-		24	222
PD-CuO_x/C	**Ethylene**	-1.4	0.1 M $KHCO_3$	MEA Cell	26.0	45	48	223
$CuCo_2Se_4$	**Acetate**	-0.25	0.3 m NaHCO3	H-type Cell	26	100	100	224
Cu(salophen)-coated GDE	**C_{2+}**	-1.2	1 m KOH	H-type Cell	121	37	2	225
Ag–Cu_2O	**Acetic Acid**	-0.9	1 m KOH	H-type Cell	310	70	20	226
Hydroxo-bridged phenanthroline Cu (II) molecule	**Ethylene**	-1.25	0.1 m $CsHCO_3$	H-type Cell	-5.5	42	15	227
Cu NC spheres	**Ethylene**	-1.1	0.1 M $KHCO_3$	H-type Cell	-9	41	1	228
Copper electrodes	**Methane**	-1.2	0.1 M $KHCO_3$	H-type Cell	5	45	8	229
Oxygen-bearing copper	**Ethylene**	-0.95	0.3 m $NaHCO_3$	H-type Cell	44.7	45	1	230

Nano defective Cu nanosheets	**Ethylene**	-1.0	0.1 m K_2SO_4	Flow Cell	66.5	83.2	1	[231]

View Article Online
DOI: 10.1039/D4YA00302K

6. Comparative analysis of Cu/S-associated $ERCO_2$ Catalysts with other best-performing Cu-based and metal-sulfide-based $ERCO_2$ Catalysts

The performance data and recent research of earlier studies for different Cu/S-associated nanomaterials are summarized in Table 1. Table 2 and Table 3 present the best-performing Cu-based and metal-sulfide-based nanomaterials (MS-based nanomaterials) for $ERCO_2$ catalysts (other than copper-sulfide-based) to compare the catalytic efficacy of Cu/S-associated nanomaterials (summarized in Table 1) with an emphasis on partial current density and faradaic efficiency. Table 1 indicates that many Cu/S-associated nanomaterials have demonstrated acceptable levels of stability during the $ERCO_2$ as well as good partial current density and faradaic efficiency for mainly formate/HCOOH production. However, for C_1 and C_{2+} products, the performance of Cu/S-associated nanomaterials is unsatisfactory in terms of Faradaic efficiency and product selectivity. Other than HCOOH/formate, several Cu/S-associated nanomaterials such as N-doped Cu_2S thin layers,[171] Polycrystalline Cu (Cu-s),[100] S-doped spherical coral-like CuO,[174] CSVE-Cu,[142] DSV-engineered CuS,[143] S-HKUST-1,[154] CeO_2-modified CuS nanoplates,[158] and Cu_2S nanocrystal-decorated Cu nanosheets,[155] have been yielded to C_{2+} products. However, their selectivities are much lower compared to that of best-performing Cu-associated, i.e., dCu_2O/Ag2.3%,[194] Ag–Cu_2O,[226] Cu_3N-derived Cu nanowires,[211] CuO-derived Cu,[212] Cu(salophen)-coated GDE,[225] Cu@$Cu_2(OH)_3NO$,[215] Cu_2O films,[217] Oxygen-bearing copper,[230] Nano defective Cu nanosheets[231]. In conclusion, combining Cu/S-associated nanomaterials with other nanomaterials, i.e., metal oxide, single-atom metals, metal selenide and metal phosphide, through various engineering/modifications strategies could be effective for higher C_{2+} product selectivity. In addition, cadmium-based sulfide, molybdenum-based sulfide and zinc-based sulfide, as summarized in Table 3, electrocatalysts exhibited better current density and faradaic efficiency performance than Cu/S-associated and Cu-based catalysts for CO production. Furthermore, for CH_4 production, CuS/Ni foam[111] electrocatalyst offered better performance than Cu/MoS_2[262] and $Fe_{4.5}Ni_{4.5}S_8$ [282] regarding partial current density and Faradaic efficiency.

Table 3 A overview of other metal-sulfide-associated $ERCO_2$ catalysts

Metal-sulfides	Electrocatalysts	Potential (V_{RHE})	Electrolyte Used	Main Products	Cell	Partial Current density (mA/cm²)	Faradaic Efficiency (%)	Stability (h)	Ref.
Cadmium-associated sulfide	**Ag-CdS_{1-x}**	-1.1	1M $KHCO_3$	CO	H-type cell	53.7	87.1	-	[232]
	P–Cd|S	-0.8	0.5 M $KHCO_3$	CO	H-type cell	89.8	88	10	[233]
	Nanoneedle-shaped CdS	-1.2	0.1 M $KHCO_3$	CO	Flow-Cell	212	95.5±4.0	24	[234]
	CdS nanorods	-1.2	0.1 M $KHCO_3$	CO	H-type cell	~22	81	10	[235]
	CdS with S-vacancy	-0.8 to -1.1	0.5 M $KHCO_3$	CO	H-type cell	~1.3	95	40	[236]
	S vacancy engineered CdS nanorods	-1.1	0.5 M $KHCO_3$	CO	H-type cell	20.5	100±0.5	10	[237]
	CdS supported CNTs	-1.2	0.1 M $KHCO_3$	CO	H-type cell	~13 (total)	~95	10	[238]
	CdS/MXene	-1.0	0.1 M $KHCO_3$	CO	H-type cell	~6	94	8	[239]
	Ag_2S/CdS	-1.1	0.5 M $KHCO_3$	CO	Flow-Cell	10.6	95	20	[240]
Tin-associated sulfide	**Hybridized composite of defective SnS_2 nanosheets and Ag nanowires**	-0.1	0.5 M $KHCO_3$	HCOOH	H-type cell	23.3	60	10	[241]
	5 % Ni-doped SnS_2 nanosheets	-0.9	0.1 M $KHCO_3$	CO & HCOOH	H-type cell	19.6 (total)	93	8	[242]
	Sn(S)/Au	-0.75	0.1 M $KHCO_3$	HCOOH	H-type cell	51	93.3	40	[243]
	Stannous Sulfide by Amino-Functionalized Carbon	-0.9	0.5 M $KHCO_3$	HCOOH	H-type cell	41.1	92.6	15	[244]
	SnS_2 nanosheets supported on rGO	-1.4	0.5 M $NaHCO_3$	HCOOH	H-type cell	11.75	84.5	2	[245]
	Tin(IV) sulfide monolayers	-0.8	0.1 M $KHCO_3$	HCOOH	H-type cell	~45 (total)	94 ± 5	80	[246]
	N-Sn(S) nanosheets	-0.7	0.1 M $KHCO_3$	HCOOH	Flow-cell	25 (total)	93.3	20	[247]
	Semimetal phased 1H-SnS_2	-0.8	0.1 M $KHCO_3$	CO	H-type cell	10.9	98.2	15	[248]
Bismuth-associated sulfide	**S doped-Bi_2O_3-CNT**	-0.9	0.5 M $KHCO_3$	HCOOH	H-type cell	48.64	97.06	10	[249]
	S-derived Bi	-0.75	0.5 M $NaHCO_3$	HCOOH	H-type cell	5 (total)	84	24	[250]
	Bi_2S_3–Bi_2O_3/rGO	-0.9	0.1 M $KHCO_3$	HCOOH	H-type cell	~3.8	90	24	[251]
	Bi-Bi_2S_3	-1.0	0.1 M $KHCO_3$	HCOOH	H-type cell	~14	85	12	[252]
	S-doped two-dimensional (2D) bismuth subcarbonate (S-BiOC)	-0.9	0.5 M $KHCO_3$	HCOOH	H-type cell	29	>90	20	[253]

View Article Online
DOI: 10.1039/D4YA00302K

	Bi_2S_3–PPy	-0.9	0.5 M $KHCO_3$	HCOOH	H-type cell	56.95 (total)	91.18	>110 h	254
	2D defective Bi_2S_3 NSs	-0.93	0.5 M $KHCO_3$	HCOOH	H-type cell	~30	>90%	200	255
Molybdenum-associated sulfide	**Bulk MoS_2**	-0.764	4 mol% EMIM-BF_4 solution	CO	H-type cell	65	98	10	256
	rGO–PEI–MoS_x	-0.65	0.5 M $NaHCO_3$	CO	H-type cell	55 (total)	85.1	-	257
	N-MoS_2@NCDs-180	-0.9	6 mol% EMIM-BF_4 solution	CO	H-type cell	36.2	90.2	10	258
	Cu-g-C_3N_4/MoS_2	-0.67	0.5 M $KHCO_3$	CH_3OH	H-type cell	78	19.7	30	259
	CuO–ZnO–MoS_2	-0.6 & -0.9	0.5 M $KHCO_3$	Methanol & Ethanol	H-type cell	121 (total)	24.6 & 11.1	3	260
	NCMSH	-0.7	4 mol% EMIM-BF_4 solution	CO	H-type cell	34.31	92.68	24	261
	Cu/MoS_2	-1.4V_{SCE}	0.1 M $KHCO_3$	CH_4	H-type cell	~3.2	17.08	48	262
	VA-$Mo_{0.95}Nb_{0.05}S_2$	-0.8	50 vol % EMIM−BF_4	CO	H-type cell	237 (total)	80	-	263
	Cu_2O@MoS_2 nanosheets	−1.3 and −1.1	0.5 M $KHCO_3$	Methanol & Ethanol	H-type cell	113 (total)	12.3 & 7.9	2	264
	H-E-MoS_2 with decoration of fluorosilane	-0.9	6 mol% EMIM-BF_4 solution	CO	H-type cell	-	81	10	265
	Monolayers of MoSeS alloys	-0.15	4 mol% EMIM-BF_4 solution	CO	H-type cell	43	45.2	10	266
Indium-associated sulfide	**In Nanoparticles on In_2S_3 nanosheets**	-1.0	1 M $KHCO_3$	HCOOH	H-type cell	40.3	76	8	267
	Mn-In_2S_3	-0.9	0.1 M $KHCO_3$	HCOOH	H-type cell	20.1 (total)	90	8	268
	$ZnIn_2S_4$	-1.18	1 M $KHCO_3$	HCOOH	Flow cell	~298	99.3	60	269
	Flower-shaped In_2S_3	-2.3	$BmimPF_6$/ MeCN−H_2O solution	HCOOH & CO	H-type cell	25.6	86	10	270
	S-In	-0.98	0.1 M $KHCO_3$	HCOOH	H-type cell	84 (total)	93	10	271
	ZnO NW/CIGS/InS	−0.24	0.1 M $KHCO_3$	HCOOH	H-type cell	0.35	77.2	10	272
	ZnO NF/CIGS/InS	−0.24	0.1 M $KHCO_3$	HCOOH	H-type cell	-	68.1	-	272
Lead-associated sulfide	**Wafer-structured sulfur-derived Pb**	-1.08	0.1 M $KHCO_3$	HCOOH	H-type cell	12	88	-	273
	PbS nanocrystals	-1.2	0.1 M $KHCO_3$	HCOOH	H-type cell	-	97.6±5.3	10	274
Zinc-associated sulfide	**ZnS@Zn**	-2.4 $V_{Fc/Fc+}$	Propylene carbonate/ $(CH_3CH_2CH_2CH_2)_4N(ClO_4)$	CO	H-type cell	6.4	92	4	275
	S–Zn–S nanosheets	-0.8	0.1 M $KHCO_3$	CO	H-type cell	~11	94.2	15	276
	ZnS@ZnO	-0.56	1 M KOH	CO	H-type cell	~109	97.2±0.5	40	277
	TA-ZnS	−1.9 $V_{Ag\|AgCl}$	0.1 M $KHCO_3$	CO	H-type cell	~7	~ 83	20	278

View Article Online
DOI: 10.1039/D4YA00302K

Titanium-associated sulfide	**Semi-metallic titanium disulfide (TiS_2)**	-0.5	0.1 M NBu_4–PF_6	CO	H-type cell	5	83	16	[279]
Other Bimetallic-sulfide	**Ni_2FeS_4 nanosheets**	−0.7	0.1 M $KHCO_3$	CO	H-type cell	-	5.9	1	[280]
	FeS_2/NiS nanocomposite	−0.6	0.5 M $KHCO_3$	CH_3OH	H-type cell	3.1 (total)	64	4	[281]
	Bulk Fe/Ni sulfides ($Fe_{4.5}Ni_{4.5}S_8$ pentlandite)	−1.80 V_{NHE}	0.1 M $TBAPF_6$	CO & methane	H-type cell	3 (total)	87 & 13	15	[282]
	$Fe_3Ni_6S_8$	−1.80 V_{NHE}	0.1 M $TBAPF_6$/aceto nitrile solution	CO	H-type cell	15 (total)	3.6	8	[283]
	$Fe_{4.5}Ni_{4.5}S_4Se_4$	−1.80 V_{NHE}	Acetonitrile	CO	H-type cell	11	84	2	[284]

7. Practical applications of Cu/s-associated $ERCO_2$ Catalysts

The execution of $ERCO_2$ on Cu/s-associated catalysts on a practical level is still in its initial stages due to several difficulties. The primary challenges to the commercialization of Cu/S-based $ERCO_2$ catalysts are (1) considerable CO_2 extraction and purification costs, as $ERCO_2$ needs highly pure (99.999%) CO_2, (2) consumes high energy, (3) low yield of energy-dense C_{2+} products and (3) a restricted marketplace that is less attractive to investors.[285,286] In addition, there are multiple technical obstacles related to $ERCO_2$, such as low catalytic performance, poor product selectivity, unsatisfactory catalytic stability, and non-optimization of cell design for use in practice.[287,288] While Cu/S-based materials yielded several products during $ERCO_2$, producing formate/HCOOH was observed as the main product. However some catalysts can produce hydrocarbons, but their selectivities are much lower than those of copper nanoparticles or oxide-derived copper. This section discusses the possibilities of scaling up $ERCO_2$ technology to the industrial level, focusing on the practical applications of formate/HCOOH production.

Indeed, scaling up an $ERCO_2$ cell for formate/HCOOH production is complex because various factors and constraints must be investigated and carefully evaluated to maintain stable cell efficiency.[289] A study revealed that the cell must maintain consistent operation for at least 8000 hours for commercial applications. Additionally, it should exhibit an overpotential beneath $1.0V_{RHE}$, a partial current density between 200-1000 mA/cm^2, and formate/HCOOH faradaic efficiency above 90% during stable operation.[290] Another research stated that the electrolyzer should be stable for a minimum of 20,000 hours to be financially viable.[291] In this context, the proton exchange membrane and electrode framework also play a vital role in stabilizing the cell. Among the various membranes reported, bipolar membranes have received much attention for large-scale use because they can maintain p^H gradient, decrease liquid crossover, and promote water separation at the membrane electrolyte interface.[292,293] Operating variables such as electrolyte, flow rate, p^H, and CO_2 feed type can all be optimized to improve cell efficiency.[294] Nowadays, there are only a few huge-scale CO_2 electrolyzers for methane, CO, C_1, C_{2+}, and formic acid generation.[295,296] Few academic institutions executed large-scale manufacture of formate/formic acid using $ERCO_2$. For example, in 2008, a pilot plant was constructed with a maximum output of 146 kg CO_2/day, leading to approximately 110 kg formic acid/day at an operating pressure of around 10 bar.[297] A different approach to the current scale-up investigation revealed a pre-pilot facility output of 55 kg CO_2/day, resulting in approximately 12 kg of formate/day at ambient pressure.[298]

While the aforementioned studies demonstrated the practicality of this approach for scaling up, several obstacles must be addressed to maximize plant functionality. One of the primary challenging tasks is maintaining a higher constant current density (recommended > 200 mA/cm^2) during the $ERCO_2$ process. The higher current density value denotes a high electrochemical reaction rate, which raises the rate at which different products are produced. Notably, the electrode's properties and structure, as well as that of both the catalyst and the support material, significantly impact the current density. The lower energy efficiency presents another difficulty. The system demonstrated 28% and 33% energy efficiency in a lab-scale three-compartment set-up over a 1000-hour operation at current densities >100 mA/cm^2.[299] But, during 450 minutes of operation on a pilot scale, the energy efficiency exceeds 50%.[297] However, data on the energy efficiency of various product formations on a large/pilot scale is scarce. Notably, the FE should be higher and the overpotential lower to maintain high cell energy efficiency. The support material on the working electrode, electrocatalytic properties, and anode material primarily determines these parameters. In addition, the choice of the membrane is crucial because it may substantially decrease the IR drop between the compartments, i.e., cathodic and anodic, lowering the cell overpotential and increasing energy efficiency. It is advised that the potential is between 2.5 and 3 V and that the FE is more excellent than 90% for industrial-scale implementation.[300–302]

The cell construction for $ERCO_2$ to formate/formic acid remains to be developed for industrial use. Every design has pros and cons of its own. However, the PEM cell layout appears to be a viable strategy for scaling up.[303] The PEM design demonstrated a reasonably higher FE for formic acid generation for Cu/S-associated electrocatalysts with a stable cell procedure of more than 100 hours.[170] However, multiple challenges restrict the use of PEM in commercial for $ERCO_2$ to formate/formic acid and other (i.e., C_1 and C_{2+} products), including declination of membrane performance over time and GDE flooding. When the cell is operated at high pressure, the mechanical strength of the membrane becomes a significant issue, leading to a higher crossover rate of formic acid and membrane damage. Also, further research must be carried out on enhancing cell stability and efficiency. Although the PEM cell demonstrated FE of 90% and steady performance for 100 hours,[170] an industrial application necessitates cell procedure for a minimum of 8000 hours with FE greater than 90%.[290] Design aspects and operational variables should be considered when designing a cell assembly that can sustain long-term operation, encounter commercial operation demands, and be cost-effective. However, membranes are costly and need periodic replacement. According to researchers, membrane-lees $ERCO_2$ cells require more care to prevent frequent maintenance or membrane damage. Another significant problem is the overflow of GDE with electrolytes, which could harm the

electrode structure and lower CO_2 conversion. Gas-phase $ERCO_2$ cells may avoid such issues, so more research into these cells is needed to develop efficient, stable, and long-lasting $ERCO_2$ cells.

7. Summary and outlook

This review discusses several strategies for modifying Cu/S-associated nanomaterials, which are recognized as highly promising electrocatalysts for $ERCO_2$. These strategies include adjustments to morphologies, structures, nanosize effects, and heterointerfaces, which all contribute to triggering electronic modulation effects within the nanomaterials. This modulation leads to the discovery of multiple active sites and facilitates charge redistribution, ultimately boosting the adsorption energy of intermediates and enhancing electrocatalytic activity. Additionally, recent advancements in engineered Cu/S-associated nanomaterials for $ERCO_2$ are summarized, shedding light on the interplay between engineering strategies, reaction mechanisms, and electrocatalytic performance. The article provides insights into the formation mechanisms, synthetic strategy, and the diverse morphological and compositional variations observed in Cu/S-associated nanomaterials.

Despite the progress achieved for the engineered Cu/S-associated nanomaterials, there are still some challenges and opportunities that should be addressed in the following aspects:

(1) Regarding the design and development of Cu/S-associated nanomaterials, novel synthesis procedures are required to develop copper sulfide materials with various unique morphologies (i.e., nano-tips, nanoparticles, two-dimensional layered structures, and so on). and crystal and phase structures (i.e., $Cu_{1.97}S$, $Cu_{1.80}S$, and so on), to increase the catalyst's performance. Also, combining different phases and components of low-cost $Cu_{2-x}S$ templates to create versatile and multifunctional nanocomposite heterostructures promotes $ERCO_2$ catalysis with multi-active sites and synergistic effects.

(2) Investigating the actual role of phase changing CuS in during the electrolysis process without converting it to CuO, Cu_2O and metallic Cu. It is also conceivable to examine the approach of stabilizing S vacancies from a different angle. Therefore, a long-term stability analysis is advised to evaluate the poisoning or degradation of the catalyst, which is vital for the catalyst's design and development.

(3) Improving C_{2+} product selectivity and catalysts stability of Cu/S-associated nanomaterials for CO_2 reduction. Maximum Cu/S-associated nanomaterials have relatively high $ERCO_2$ catalytic selectivity and high Faradaic efficiency towards CO and HCOOH (as summarised in Table 1), and other C_1 products and high-energy-dense C_2 products are challenging to generate. Thus, obtaining high-energy-dense C_2 products is crucial for commercial electrochemical CO_2 conversion.

(4) Implementation of sophisticated characterization technology. For heterogenous electrocatalysis, the catalyst's surface is an essential active site for the catalytic reaction. The interaction between the surface-active sites and the reaction intermediates is the primary factor influencing the catalytic activity. As a result, more cutting-edge in situ characterization techniques, such as in situ Raman, Fourier transform infrared spectroscopy (FTIR), and X-ray absorption spectroscopy (XAS), must be used to identify the nature of active sites and binding/adsorption energies between active sites and intermediates during $ERCO_2$ on Cu/S-associated electrocatalysts.

(5) Execution of comprehensive and advanced theoretical techniques Theoretical modelling and simulation are mandatory to understand the reaction process and establish the structure-activity relationship. Several studies have shown that DFT is a practical approach for determining the energy values of chemical intermediates. Also, many reported theoretically expected processes may differ between DFT models. Also, several computational outcomes may be theoretically possible but not experimentally viable. Thus, DFT analysis is closely linked with experimental outcomes, especially in situ technique results, confirming its viability for understanding reaction processes.

Closing the gap between lab-scale research and industrial applications. Momentous improvements have been observed in the study and in the lab-scale use of Cu/S-associated nanomaterials for $ERCO_2$. However, implementing Cu/S-associated electrocatalysts on a large scale in real-world uses remains a significant challenge. Smaller batch preparation and controlled laboratory conditions make academic research much more straightforward, while industrial manufacturing requires additional factors like instrument stability, process consistency, and scaling up experiments. Although Cu/S-associated electrocatalysts have advanced significantly in practical uses, there is still more work to be done before vast commercial applications. Therefore, reducing the gap between lab-scale research and industrial applications is crucial for Cu/S-associated electrocatalysts.

Acknowledgements

The authors gratefully acknowledge Birla Institute of Technology, Mesra, for providing the institute research fellowship and I-STEM/catalytic grant/acad_18/2022-2023 for financial support.

Conflict of Interest

The authors declare no conflict of interest.

Author Contributions

A.M. conducted the literature search, wrote the final manuscript, and created figures and tables. MA, SSM, and BCR, supervised and revised the manuscript. All authors were involved in the discussion and critical revision, and the final version of the manuscript was approved.

References

1 N. Patel and D. Mehta, *Int. J. Thermofluids*, 2023, **20**, 100397.
2 B. Doğan, M. Shahbaz, M. F. Bashir, S. Abbas and S. Ghosh, *Renew. Sustain. Energy Rev.*, 2023, **184**, 113551.
3 Y. Huang, Z. Kuldasheva, S. Bobojanov, B. Djalilov, R. Salahodjaev and S. Abbas, *Environ. Sci. Pollut. Res.*, 2023, **30**, 10854–10866.
4 L. J. R. Nunes, *Environ. 2023, Vol. 10, Page 66*, 2023, **10**, 66.
5 E. Liu, X. Lu and D. Wang, *Energies*, 2023, **16**, 2865.
6 B. Dziejarski, R. Krzyżyńska and K. Andersson, *Fuel*, 2023, **342**, 127776.
7 N. Yusuf, F. Almomani and H. Qiblawey, *Fuel*, 2023, **345**, 128178.

8 W. Chung, W. Jeong, J. Lee, J. Kim, K. Roh and J. H. Lee, *Comput. Chem. Eng.*, 2023, **170**, 108106.
9 J.-Y. Chen, M. Li and R.-Z. Liao, *Inorg. Chem.*, 2023, **62**, 9400–9417.
10 M. Li, K. Yang, M. Abdinejad, C. Zhao and T. Burdyny, *Nanoscale*, 2022, **14**, 11892–11908.
11 G. Bhattacharya, R. Manna, P. Sardar, S. Rahut and A. N. Samanta, *Ind. Eng. Chem. Res.*, , DOI:10.1021/ACS.IECR.4C00246/SUPPL_FILE/IE4C00246_SI_001.PDF.
12 Y. Fang, Y. Liu, L. Qi, Y. Xue and Y. Li, *Chem. Soc. Rev.*, 2022, **51**, 2681–2709.
13 S. Bierbaumer, M. Nattermann, L. Schulz, R. Zschoche, T. J. Erb, C. K. Winkler, M. Tinzl and S. M. Glueck, *Chem. Rev.*, 2023, **123**, 5702–5754.
14 S. Wei, W. Liu, C. Yang, P. Bai, X. Kong, W. Sun and L. Xu, *Mater. Chem. Front.*, 2023, **7**, 4723–4743.
15 M. Abdinejad, A. Seifitokaldani, C. Dao, E. H. Sargent, X. A. Zhang and H. B. Kraatz, *ACS Appl. Energy Mater.*, 2019, **2**, 1330–1335.
16 S. Kaur, M. Kumar, D. Gupta, P. P. Mohanty, T. Das, S. Chakraborty, R. Ahuja and T. C. Nagaiah, *Nano Energy*, 2023, **109**, 108242.
17 M. Abdinejad, M. N. Hossain and H. B. Kraatz, *RSC Adv.*, 2020, **10**, 38013–38023.
18 C. He, Y. Gong, S. Li, J. Wu, Z. Lu, Q. Li, L. Wang, S. Wu and J. Zhang, *Adv. Mater.*, 2024, 2311628.
19 M. Abdinejad, T. Yuan, K. Tang, S. Duangdangchote, A. Farzi, H. P. Iglesias van Montfort, M. Li, J. Middelkoop, M. Wolff, A. Seifitokaldani, O. Voznyy and T. Burdyny, *Chem. – A Eur. J.*, 2023, **29**, e202203977.
20 I. Masood ul Hasan, L. Peng, J. Mao, R. He, Y. Wang, J. Fu, N. Xu and J. Qiao, *Carbon Energy*, 2021, **3**, 24–49.
21 M. Abdinejad, I. Santos da Silva and H. B. Kraatz, *J. Mater. Chem. A*, 2021, **9**, 9791–9797.
22 M. Abdinejad, E. Irtem, A. Farzi, M. Sassenburg, S. Subramanian, H. P. Iglesias Van Montfort, D. Ripepi, M. Li, J. Middelkoop, A. Seifitokaldani and T. Burdyny, *ACS Catal.*, 2022, **12**, 7862–7876.
23 Z. Masood and Q. Ge, *Catal. Today*, 2023, **409**, 53–62.
24 Q. Cheng, M. Huang, L. Xiao, S. Mou, X. Zhao, Y. Xie, G. Jiang, X. Jiang and F. Dong, *ACS Catal.*, 2023, **13**, 4021–4029.
25 A. Mukherjee, M. Abdinejad, S. S. Mahapatra and B. C. Ruidas, *J. Mater. Chem. A*, 2023, **11**, 9300–9332.
26 M. Isegawa, *Chem. Phys.*, 2023, **565**, 111758.
27 K. Kim, P. Wagner, K. Wagner and A. J. Mozer, *Molecules*, 2023, **28**, 5179.
28 X. Song, L. Xu, X. Sun and B. Han, *Sci. China Chem.*, 2023, **66**, 315–323.
29 M. Todoroki, K. Hara, A. Kudo and T. Sakata, *J. Electroanal. Chem.*, 1995, **394**, 199–203.
30 J. W. Jang, S. Cho, G. Magesh, Y. J. Jang, J. Y. Kim, W. Y. Kim, J. K. Seo, S. Kim, K. H. Lee and J. S. Lee, *Angew. Chemie - Int. Ed.*, 2014, **53**, 5852–5857.
31 G. O. Larrazábal, A. J. Martín, S. Mitchell, R. Hauert and J. Pérez-Ramírez, *ACS Catal.*, 2016, **6**, 6265–6274.
32 B. Ávila-Bolívar, L. García-Cruz, V. Montiel and J. Solla-Gullón, *Mol. 2019, Vol. 24, Page 2032*, 2019, **24**, 2032.
33 Q. Li, J. Fu, W. Zhu, Z. Chen, B. Shen, L. Wu, Z. Xi, T. Wang, G. Lu, J. J. Zhu and S. Sun, *J. Am. Chem. Soc.*, 2017, **139**, 4290–4293.
34 S. Santra, V. Streibel, L. I. Wagner, N. Cheng, P. Ding, G. Zhou, E. Sirotti, R. Kisslinger, T. Rieth, S. Zhang and I. D. Sharp, *ChemSusChem*, 2024, **17**, e202301452.
35 W. Zhu, R. Michalsky, Ö. Metin, H. Lv, S. Guo, C. J. Wright, X. Sun, A. A. Peterson and S. Sun, *J. Am. Chem. Soc.*, 2013, **135**, 16833–16836.
36 W. Zhu, Y. J. Zhang, H. Zhang, H. Lv, Q. Li, R. Michalsky, A. A. Peterson and S. Sun, *J. Am. Chem. Soc.*, 2014, **136**, 16132–16135.
37 K. Sun, L. Wu, W. Qin, J. Zhou, Y. Hu, Z. Jiang, B. Shen and Z. Wang, *J. Mater. Chem. A*, 2016, **4**, 12616–12623.
38 R. Wang, H. Haspel, A. Pustovarenko, A. Dikhtiarenko, A. Russkikh, G. Shterk, D. Osadchii, S. Ould-Chikh, M. Ma, W. A. Smith, K. Takanabe, F. Kapteijn and J. Gascon, *ACS Energy Lett.*, 2019, **4**, 2024–2031.
39 D. H. Won, H. Shin, J. Koh, J. Chung, H. S. Lee, H. Kim and S. I. Woo, *Angew. Chemie*, 2016, **128**, 9443–9446.
40 W. Luo, J. Zhang, M. Li and A. Züttel, *ACS Catal.*, 2019, **9**, 3783–3791.
41 A. Klinkova, P. De Luna, C. T. Dinh, O. Voznyy, E. M. Larin, E. Kumacheva and E. H. Sargent, *ACS Catal.*, 2016, **6**, 8115–8120.
42 J. Zeng, W. Zhang, Y. Yang, D. Li, X. Yu and Q. Gao, *ACS Appl. Mater. Interfaces*, 2019, **11**, 33074–33081.
43 F. A. Hanc-Scherer, M. A. Montiel, V. Montiel, E. Herrero and C. M. Sánchez-Sánchez, *Phys. Chem. Chem. Phys.*, 2015, **17**, 23909–23916.
44 M. Umeda, Y. Niitsuma, T. Horikawa, S. Matsuda and M. Osawa, *ACS Appl. Energy Mater.*, 2020, **3**, 1119–1127.
45 J. Yin, J. Jin, Z. Yin, L. Zhu, X. Du, Y. Peng, P. Xi, C. H. Yan and S. Sun, *Nat. Commun. 2023 141*, 2023, **14**, 1–10.
46 S. Pérez-Rodríguez, G. García, L. Calvillo, V. Celorrio, E. Pastor and M. J. Lázaro, *Int. J. Electrochem.*, 2011, **2011**, 1–13.
47 H. Bin Yang, S. F. Hung, S. Liu, K. Yuan, S. Miao, L. Zhang, X. Huang, H. Y. Wang, W. Cai, R. Chen, J. Gao, X. Yang, W. Chen, Y. Huang, H. M. Chen, C. M. Li, T. Zhang and B. Liu, *Nat. Energy 2018 32*, 2018, **3**, 140–147.
48 J. Han, B. Tu, P. An, J. Zhang, Z. Yan, X. Zhang, C. Long, Y. Zhu, Y. Yuan, X. Qiu, Z. Yang, X. Huang, S. Yan and Z. Tang, *Adv. Mater.*, 2024, **36**, 2313926.
49 R. Chen, X. Zu, J. Zhu, Y. Zhao, Y. Li, Z. Hu, S. Wang, M. Fan, S. Zhu, H. Zhang, B. Ye, Y. Sun and Y. Xie, *Adv. Mater.*, 2024, **36**, 2314209.
50 Y. Hori, *Mod. Asp. Electrochem.*, 2008, 89–189.
51 C. Kong, G. Jiang, Y. Sheng, Y. H. Liu, F. Gao, F. Liu and X. Duan, *Chem. Eng. J.*, 2023, **460**, 141803.
52 M. Li and J. N. Zhang, *Sci. China Chem.*, 2023, **66**, 1288–1317.
53 J. Yan, H. Ma, J. Ni, J. Ma, J. Xu, J. Qi, S. Zhu and L. Lu, *J. Colloid Interface Sci.*, 2023, **648**, 558–566.
54 A. Alherz, C. Musgrave, O. Luca, R. Sundararaman, W. Smith and J. Cha, .

55 J. Zhang, C. Guo, S. Fang, X. Zhao, L. Li, H. Jiang, Z. Liu, Z. Fan, W. Xu, J. Xiao and M. Zhong, *Nat. Commun. 2023 141*, 2023, **14**, 1–11.

56 M. Ding, Z. Chen, C. Liu, Y. Wang, C. Li, X. Li, T. Zheng, Q. Jiang and C. Xia, *Mater. Reports Energy*, 2023, **3**, 100175.

57 D. Song, Y. Lian, M. Wang, Y. Su, F. Lyu, Z. Deng and Y. Peng, *eScience*, 2023, **3**, 100097.

58 M. Abdinejad, S. Subramanian, K. Motlagh, M. Noroozifar, S. Duangdangchote, I. Neporozhnii, D. Ripepi, D. Pinto, M. Li, K. Tang, J. Middelkoop, A. Urakawa, O. Voznyy, H.-B. Kraatz, T. Burdyny, M. Abdinejad, S. Subramanian, D. Ripepi, D. Pinto, M. Li, J. Middelkoop, A. Urakawa, T. Burdyny, M. K. Motlagh, M. Noroozifar, S. Duangdangchote, I. Neporozhnii, K. Tang, O. Voznyy and H.-B. Kraatz, *Adv. Energy Mater.*, 2023, **13**, 2300402.

59 S. Nitopi, E. Bertheussen, S. B. Scott, X. Liu, A. K. Engstfeld, S. Horch, B. Seger, I. E. L. Stephens, K. Chan, C. Hahn, J. K. Nørskov, T. F. Jaramillo and I. Chorkendorff, *Chem. Rev.*, 2019, **119**, 7610–7672.

60 M. Li, Y. Hu, T. Wu, A. Sumboja and D. Geng, *Mater. Today*, , DOI:10.1016/J.MATTOD.2023.05.028.

61 K. Yang, Y. Sun, S. Chen, M. Li, M. Zheng, L. Ma, W. Fan, Y. Zheng, Q. Li and J. Duan, *Small*, 2023, **19**, 2301536.

62 Y. Hori, H. Wakebe, T. Tsukamoto and O. Koga, *Surf. Sci.*, 1995, **335**, 258–263.

63 Y. Hori, I. Takahashi, O. Koga and N. Hoshi, *J. Mol. Catal. A Chem.*, 2003, **199**, 39–47.

64 R. Reske, H. Mistry, F. Behafarid, B. Roldan Cuenya and P. Strasser, *J. Am. Chem. Soc.*, 2014, **136**, 6978–6986.

65 J. Chen, S. K. Iyemperumal, T. Fenton, A. Carl, R. Grimm, G. Li and N. A. Deskins, *ACS Catal.*, 2018, **8**, 10464–10478.

66 W. Tang, A. A. Peterson, A. S. Varela, Z. P. Jovanov, L. Bech, W. J. Durand, S. Dahl, J. K. Nørskov and I. Chorkendorff, *Phys. Chem. Chem. Phys.*, 2011, **14**, 76–81.

67 Z. Lyu, S. Zhu, M. Xie, Y. Zhang, Z. Chen, R. Chen, M. Tian, M. Chi, M. Shao and Y. Xia, *Angew. Chemie Int. Ed.*, 2021, **60**, 1909–1915.

68 Y. Wang, C. Niu, Y. Zhu, D. He and W. Huang, *ACS Appl. Energy Mater.*, 2020, **3**, 9841–9847.

69 T. T. H. Hoang, S. Ma, J. I. Gold, P. J. A. Kenis and A. A. Gewirth, *ACS Catal.*, 2017, **7**, 3313–3321.

70 K. Banjac, T. H. Phan, F. P. Cometto, P. Alexa, Y. Liang, R. Gutzler and M. Lingenfelder, , DOI:10.26434/CHEMRXIV-2021-XWLT8.

71 R. M. Arán-Ais, R. Rizo, P. Grosse, G. Algara-Siller, K. Dembélé, M. Plodinec, T. Lunkenbein, S. W. Chee and B. Roldan Cuenya, *Nat. Commun. 2020 111*, 2020, **11**, 1–8.

72 J. Shen, L. Wang, X. He, S. Wang, J. Chen, J. Wang and H. Jin, *ChemSusChem*, 2022, **15**, e202201350.

73 L. Wan, X. Zhang, J. Cheng, R. Chen, L. Wu, J. Shi and J. Luo, *ACS Catal.*, 2022, **12**, 2741–2748.

74 D. Majumdar, *J. Electroanal. Chem.*, 2021, **880**, 114825.

75 K. Samdhyan, P. Chand, H. Anand and S. Saini, *J. Energy Storage*, 2022, **46**, 103886.

76 Y. Xie, A. Riedinger, M. Prato, A. Casu, A. Genovese, P. Guardia, S. Sottini, C. Sangregorio, K. Miszta, S. Ghosh, T. Pellegrino and L. Manna, *J. Am. Chem. Soc.*, 2013, **135**, 17630–17637.

77 R. J. Goble, *Can. Mineral.*, 1985, **23**, 61–76.

78 G. Kalimuldina, A. Nurpeissova, A. Adylkhanova, D. Adair, I. Taniguchi and Z. Bakenov, *ACS Appl. Energy Mater.*, 2020, **3**, 11480–11499.

79 P. Roy and S. K. Srivastava, *CrystEngComm*, 2015, **17**, 7801–7815.

80 F. DI BENEDETTO, M. BORGHERESI, A. CANESCHI, G. CHASTANET, C. CIPRIANI, D. GATTESCHI, G. PRATESI, M. ROMANELLI and R. SESSOLI, *Eur. J. Mineral.*, 2006, **18**, 283–287.

81 R. Zeinodin, F. Jamali-Sheini and M. Cheraghizade, *Mater. Sci. Semicond. Process.*, 2021, **123**, 105501.

82 Z. Song, Y. Liu, B. Zhang, S. Song, Z. Zhou, Y. Huang and Z. Zhao, *New J. Chem.*, 2023, **47**, 2286–2295.

83 J. Tirado, C. Roldán-Carmona, F. A. Muñoz-Guerrero, G. Bonilla-Arboleda, M. Ralaiarisoa, G. Grancini, V. I. E. Queloz, N. Koch, M. K. Nazeeruddin and F. Jaramillo, *Appl. Surf. Sci.*, 2019, **478**, 607–614.

84 P. Tetyana, N. Mphuthi, A. N. Jijana, N. Moloto, P. M. Shumbula, A. Skepu, L. S. Vilakazi and L. Sikhwivhilu, *Nanomaterials*, 2023, **13**, 481.

85 E. M. Mkawi, M. W. Iqbal, Y. Al-Hadeethi, H. Hassan, B. Arkook, F. G. ALmehmadi and J. O. Dennis, *J. Energy Storage*, 2023, **67**, 107656.

86 J. He, K. Ramachandraiah, T. Huang, T. Yuan, X. Liu, H. Zhang and F. Ke, *Biochem. Biophys. Res. Commun.*, 2023, **638**, 51–57.

87 S. Chandrasekaran, L. Yao, L. Deng, C. Bowen, Y. Zhang, S. Chen, Z. Lin, F. Peng and P. Zhang, *Chem. Soc. Rev.*, 2019, **48**, 4178–4280.

88 O. C. Pore, A. V. Fulari, C. D. Chavare, D. S. Sawant, S. S. Patil, R. V. Shejwal, V. J. Fulari and G. M. Lohar, *Chem. Phys. Lett.*, 2023, **824**, 140551.

89 S. K. Godlaveeti, A. R. Somala and R. R. Nagireddy, *Appl. Phys. A Mater. Sci. Process.*, 2023, **129**, 1–12.

90 N. Badar, H. M. Yusoff, K. Elong and N. Kamarulzaman, *Adv. Powder Technol.*, 2023, **34**, 104102.

91 H. Bian, R. Wang, K. Zhang, H. Zheng, M. Wen, Z. Li, Z. Li, G. Wang, G. Xie, X. Liu and L. Jiang, *Surf. Coatings Technol.*, 2023, **459**, 129407.

92 E. Aboobakri, T. Heidari and M. Jahani, *Carbon Lett.*, 2023, **33**, 1629–1638.

93 M. H. Patel, T. K. Chaudhuri and V. K. Patel, *J. Mater. Sci. Mater. Electron.*, 2023, **34**, 1–9.

94 E. Gribov, E. Koshevoy, I. Chikunova and V. Parmon, *Catalysts*, 2023, **13**, 168.

95 T. Singh and V. Mutreja, *AIP Conf. Proc.*, , DOI:10.1063/5.0138167/2892379.

96 Y. Chen, K. Chen, J. Fu, A. Yamaguchi, H. Li, H. Pan, J. Hu, M. Miyauchi and M. Liu, *Nano Mater. Sci.*, 2020, **2**, 235–247.

97 Y. Tian, B. Li, J. Wang, Y. Ge, W. Gao, L. Yu, L. Ma, Y. Li, L. Wang, Z. Liu and J. Chen, *Chem. Eng. J.*, 2024, **490**, 151704.

98 C. Ye, B. Liu, Q. Li, M. Yu, Y. Liu, Z. Tai, Z. Pan and Y. Qiu, *Small*, 2024, **20**, 2309856.

99 X. Ma, Y. Zhang, T. Fan, D. Wei, Z. Huang, Z. Zhang, Z. Zhang, Y. Dong, Q. Hong, Z. Chen and X. Yi, *Adv. Funct. Mater.*,

2023, **33**, 2213145.
100 C. He, D. Duan, J. Low, Y. Bai, Y. Jiang, X. Wang, S. Chen, R. Long, L. Song and Y. Xiong, *Nano Res.*, 2023, **16**, 4494–4498.
101 T. Dou, Y. Qin, F. Zhang and X. Lei, *ACS Appl. Energy Mater.*, 2021, **4**, 4376–4384.
102 G. Janani, S. Surendran, D. K. Lee, S. Shanmugapriya, H. Lee, Y. Subramanian and U. Sim, *Aggregate*, 2024, **5**, e430.
103 C. Zhou, Y. Wu, X. Zhang, C. Ye, G. Peng and W. Yuan, *J. Nanoparticle Res.*, 2024, **26**, 1–11.
104 P. Shao, S. Ci, L. Yi, P. Cai, P. Huang, C. Cao and Z. Wen, *ChemElectroChem*, 2017, **4**, 2593–2598.
105 L. Zhang, X. Shi, A. Xu, W. Zhong, J. Zhang and S. Shen, *Nano Res.*, 2024, **17**, 3693–3699.
106 M. Ravipati and S. Badhulika, *ACS Appl. Nano Mater.*, 2024, **7**, 7277–7288.
107 L. Meng, C. W. Kao, Z. Wang, J. Ma, P. Huang, N. Zhao, X. Zheng, M. Peng, Y. R. Lu and Y. Tan, *Nat. Commun. 2024 151*, 2024, **15**, 1–10.
108 W. Zhu, L. Fan, Q. Geng, C. Wang, X. Fan, Y. Zhang and C. Li, *Chem. Eng. J.*, 2024, **489**, 151316.
109 A. Yabuki, Y. Iwamura, T. Tachibana and J. H. Lee, *New J. Chem.*, 2022, **46**, 19633–19637.
110 Q. G. Zhu, X. F. Sun, X. C. Kang, J. MA, Q. L. Qian and B. X. Han, *Wuli Huaxue Xuebao/ Acta Phys. - Chim. Sin.*, 2016, **32**, 261–266.
111 Z. Zhao, X. Peng, X. Liu, X. Sun, J. Shi, L. Han, G. Li and J. Luo, *J. Mater. Chem. A*, 2017, **5**, 20239–20243.
112 Z. Kou, X. Li, L. Zhang, W. Zang, X. Gao and J. Wang, *Small Sci.*, 2021, **1**, 2100011.
113 C. Yan, J. Huang, C. Wu, Y. Li, Y. Tan, L. Zhang, Y. Sun, X. Huang and J. Xiong, *J. Mater. Sci. Technol.*, 2020, **42**, 10–16.
114 C. Kim, S. H. Kim, S. Lee, I. Kwon, S. Kim, C. Seok, Y. S. Park and Y. Kim, *J. Energy Chem.*, 2022, **64**, 364–371.
115 K. Fan, H. Zou, Y. Lu, H. Chen, F. Li, J. Liu, L. Sun, L. Tong, M. F. Toney, M. Sui and J. Yu, *ACS Nano*, 2018, **12**, 12369–12379.
116 T. X. Nguyen, Y. H. Su, C. C. Lin and J. M. Ting, *Adv. Funct. Mater.*, 2021, **31**, 2106229.
117 J. Chen, Y. Tu, Y. Zou, X. Li and J. Jiang, *Mater. Lett.*, 2021, **284**, 128919.
118 K. R. Phillips, Y. Katayama, J. Hwang and Y. Shao-Horn, *J. Phys. Chem. Lett.*, 2018, **9**, 4407–4412.
119 B. Zhang, M. Wang, J. Ding, Y. Li, G. Cao, M. T. Bernards, Y. He and Y. Shi, *J. CO2 Util.*, 2020, **39**, 101169.
120 C. H. M. van Oversteeg, M. Tapia Rosales, K. H. Helfferich, M. Ghiasi, J. D. Meeldijk, N. J. Firet, P. Ngene, C. de Mello Donegá and P. E. de Jongh, *Catal. Today*, 2021, **377**, 157–165.
121 Y. Gao, Y. Guo, Y. Zou, W. Liu, Y. Luo, B. Liu and C. Zhao, *ACS Appl. Energy Mater.*, 2023, **6**, 1340–1354.
122 W. He, I. Liberman, I. Rozenberg, R. Ifraemov and I. Hod, *Angew. Chemie Int. Ed.*, 2020, **59**, 8262–8269.
123 J. Li, J. Li, C. Dun, W. Chen, D. Zhang, J. Gu, J. J. Urban and J. W. Ager, *RSC Adv.*, 2021, **11**, 23948–23959.
124 D. Y. Y. Goh, K. M. Yam, L. Rekhi, A. D. Handoko, Y. C. Tan, Y. Wang, J. M. R. Tan, T. S. Choksi, Y. Lum and L. H. Wong, *J. Mater. Chem. A*, 2024, **12**, 1840–1851.
125 E. Cui, W. Zhang, X. Zhou, L. Lv, W. Chen, L. Zhou and L. Mai, *ACS Appl. Nano Mater.*, 2023, **6**, 9361–9368.
126 X. Zhang, Y. Zhang, X. Wei, C. Wei and Y. Song, *Nanoscale Adv.*, 2021, **3**, 5777–5784.
127 T. Wu, M. Y. Han and Z. J. Xu, *ACS Nano*, 2022, **16**, 8531–8539.
128 T. Shinagawa, G. O. Larrazábal, A. J. Martín, F. Krumeich and J. Pérez-Ramírez, *ACS Catal.*, 2018, **8**, 837–844.
129 J. W. Lim, W. J. Dong, J. Y. Park, D. M. Hong and J. L. Lee, *ACS Appl. Mater. Interfaces*, 2020, **12**, 22891–22900.
130 H. K. Park, H. Ahn, T. H. Lee, J. Y. Lee, M. G. Lee, S. A. Lee, J. W. Yang, S. J. Kim, S. H. Ahn, S. Y. Kim, C. H. Lee, E. S. Park and H. W. Jang, *Small Methods*, 2021, **5**, 2000755.
131 X. Zhong, E. Yuan, F. Yang, Y. Liu, H. Lu, J. Yang, F. Gao, Y. Zhou, J. Pan, J. Zhu, C. Yu, C. Zhu, A. Yuan and E. H. Ang, *Proc. Natl. Acad. Sci. U. S. A.*, 2023, **120**, e2306673120.
132 X. Xu, Y. Zhong, M. Wajrak, T. Bhatelia, S. P. Jiang and Z. Shao, *InfoMat*, 2024, e12608.
133 R. Zhang, L. Wang, Y. H. Ma, L. Pan, R. Gao, K. Li, X. Zhang and J. J. Zou, *J. Mater. Chem. A*, 2019, **7**, 10010–10018.
134 R. Yang, X. Zheng, H. Fu, X. Cao, Y. Hu and Y. Huang, *ChemSusChem*, 2024, **17**, e202301771.
135 Y. Wang, H. Xu, Y. Liu, J. Jang, X. Qiu, E. P. Delmo, Q. Zhao, P. Gao and M. Shao, *Angew. Chemie Int. Ed.*, 2024, **63**, e202313858.
136 K. Wu, C. Lyu, J. Cheng, W. Ding, J. Wu, Q. Wang, W. M. Lau and J. Zheng, *Carbon Energy*, 2024, **6**, e485.
137 Y. Wang, Z. Lu, S. Wu, Z. Zou, X. Zhang and Y. Wang, *J. Environ. Chem. Eng.*, 2024, **12**, 112839.
138 Y. Liu, Z. Yang, Y. Zou, S. Wang and J. He, *Energy Environ. Mater.*, 2024, **7**, e12576.
139 J. Liang, S. Li, F. Li, L. Zhang, Y. Jiang, H. Ma, K. Cheng and L. Qing, *J. Colloid Interface Sci.*, 2024, **655**, 296–306.
140 L. Hong, B. Li, C. Jing, Z. Zhuang, Y. Zhang, H. Huang, Q. Jiang and J. Tang, *J. Environ. Chem. Eng.*, 2024, **12**, 111946.
141 Z. Guo, M. Bi, H. He, Z. Liu, Y. Duan and W. Cao, *J. Colloid Interface Sci.*, 2024, **654**, 785–794.
142 T. T. Zhuang, Z. Q. Liang, A. Seifitokaldani, Y. Li, P. De Luna, T. Burdyny, F. Che, F. Meng, Y. Min, R. Quintero-Bermudez, C. T. Dinh, Y. Pang, M. Zhong, B. Zhang, J. Li, P. N. Chen, X. L. Zheng, H. Liang, W. N. Ge, B. J. Ye, D. Sinton, S. H. Yu and E. H. Sargent, *Nat. Catal. 2018 16*, 2018, **1**, 421–428.
143 C. Peng, G. Luo, J. Zhang, M. Chen, Z. Wang, T. K. Sham, L. Zhang, Y. Li and G. Zheng, *Nat. Commun. 2021 121*, 2021, **12**, 1–8.
144 R. He, X. Huang and L. Feng, *Energy and Fuels*, 2022, **36**, 6675–6694.
145 M. Li and L. Feng, *Chinese J. Struct. Chem.*, 2022, **41**, 2201019–2201024.
146 H. Liu, D. Zhao, P. Hu, K. Chen, X. Wu and D. Xue, *Mater. Today Phys.*, 2020, **13**, 100197.
147 S. Zhang, C. Tan, R. Yan, X. Zou, F. L. Hu, Y. Mi, C. Yan and S. Zhao, *Angew. Chemie Int. Ed.*, 2023, **62**, e202302795.
148 H. Tao, T. Jia, L. Zhang, X. Li, P. Li, Y. Zhou and C. Zhai, *J. Colloid Interface Sci.*, 2024, **655**, 909–919.
149 T. Dou, J. He, S. Diao, Y. Wang, X. Zhao, F. Zhang and X. Lei, *J. Energy Chem.*, 2023, **82**, 497–506.

150 X. Wang, J. Lv, J. Zhang, X. L. Wang, C. Xue, G. Bian, D. Li, Y. Wang and T. Wu, *Nanoscale*, 2020, **12**, 772–784.

151 Y. Liu, Z. Jiang, C. Huang, S. Jeong, A. L. Coughlin, S. Zhang, Y. Liu and X. Ye, *Nano Lett.*, 2023, **23**, 5911–5918.

152 C. He, S. Chen, R. Long, L. Song and Y. Xiong, *Sci. China Chem.*, 2020, **63**, 1721–1726.

153 S. Cao, Y. Xue, X. Chen, C. Zhang, Y. Gao and Y. Li, *Mater. Chem. Front.*, 2023, **7**, 2620–2627.

154 C. F. Wen, M. Zhou, P. F. Liu, Y. Liu, X. Wu, F. Mao, S. Dai, B. Xu, X. L. Wang, Z. Jiang, P. Hu, S. Yang, H. F. Wang and H. G. Yang, *Angew. Chemie*, 2022, **134**, e202111700.

155 Y. Li, Y. Chen, T. Chen, G. Shi, L. Zhu, Y. Sun and M. Yu, *ACS Appl. Mater. Interfaces*, 2023, **15**, 18857–18866.

156 V. S. S. Mosali, G. Puxty, M. D. Horne, A. M. Bond and J. Zhang, *Electrochim. Acta*, 2024, **475**, 143628.

157 V. S. S. Mosali, X. Zhang, Y. Liang, L. Li, G. Puxty, M. D. Horne, A. Brajter-Toth, A. M. Bond and J. Zhang, *ChemSusChem*, 2021, **14**, 2924–2934.

158 Z. Yang, D. Ji, Z. Li, Z. He, Y. Hu, J. Yin, Y. Hou, P. Xi and C. H. Yan, *Small*, 2023, **19**, 2303099.

159 Q. Wang, T. Bao, X. Zhao, Y. Cao, J. Cao, Q. Li and W. Si, *Molecules*, 2024, **29**, 2948.

160 X. Han, T. Mou, S. Liu, M. Ji, Q. Gao, Q. He, H. Xin and H. Zhu, *Nanoscale Horiz*, 2022, **7**, 508–514.

161 M. Prasanna, N. Logeshwaran, S. Ramakrishnan and D. J. Yoo, *Small*, 2024, **20**, 2306165.

162 Y. Guo, Y. Gao, B. Guo, Y. Luo, G. Zhao, J. Sun, W. Li, R. Wang and C. Zhao, *Carbon Neutrality 2024 31*, 2024, **3**, 1–20.

163 Y. Wang, Y. Wang, J. Zhao, T. Tang, B. Lv, Y. Chang, T. Hu, J. Zhang, E. Luo and J. Jia, *ACS Sustain. Chem. Eng.*, 2024, **12**, 6982–6989.

164 Y. Zhang, Y. Dong, X. Yan, H. Peng, S. Xu, M. Zhu, Z. Jin, L. Han and J. Zhang, *J. Energy Storage*, 2024, **84**, 111023.

165 X. Cheng, D. Wu, H. Xu and W. Zhang, *J. Phys. Chem. C*, 2024, **128**, 12101–12108.

166 W. Cheng, H. Yang, T. Wang, X. He, L. Tian and Z. Li, *Chem. Rec.*, 2024, **24**, e202300088.

167 Y. Jia, Y. Zhang, H. Xu, J. Li, M. Gao and X. Yang, *ACS Catal.* , 2024, **14**, 4601–4637.

168 P. Xu, Z. Bao, Y. Zhao, L. Zheng, Z. Lv, X. Shi, H. E. Wang, X. Fang and H. Zheng, *Adv. Energy Mater.*, 2024, **14**, 2303557.

169 Y. Hu, J. Zhu, X. Wang, X. Zheng, X. Zhang, C. Wu, J. Zhang, C. Fu, T. Sheng and Z. Wu, *Inorg. Chem.*, 2024, **63**, 9983–9991.

170 H. Shen, Y. Zhao, L. Zhang, Y. He, S. Yang, T. Wang, Y. Cao, Y. Guo, Q. Zhang and H. Zhang, *Adv. Energy Mater.*, 2023, **13**, 2202818.

171 L. Liang, L. Yang, T. Heine, A. Arinchtein, X. Wang, J. Hübner, J. Schmidt, A. Thomas and P. Strasser, *Adv. Energy Mater.*, 2024, **14**, 2304224.

172 S. Li, H. Duan, J. Yu, C. Qiu, R. Yu, Y. Chen, Y. Fang, X. Cai and S. Yang, *ACS Catal.*, 2022, **12**, 9074–9082.

173 Y. Huang, Y. Deng, A. D. Handoko, G. K. L. Goh and B. S. Yeo, *ChemSusChem*, 2018, **11**, 320–326.

174 T. Jia, L. Wang, L. Zhang, Z. Zhu, K. Zhang, B. Zhu, X. Li, C. Zhai, S. Li, Y. Zhou and H. Tao, *Surfaces and Interfaces*, 2023, **38**, 102841.

175 H. Yuan, Z. Liu, S. Sang and X. Wang, *Appl. Surf. Sci.*, 2023, **613**, 156130.

176 X. Zhang, R. Sa, F. Zhou, Y. Rui, R. Liu, Z. Wen and R. Wang, *CCS Chem.*, 2021, **3**, 199–207.

177 Y. Deng, Y. Huang, D. Ren, A. D. Handoko, Z. W. Seh, P. Hirunsit and B. S. Yeo, *ACS Appl. Mater. Interfaces*, 2018, **10**, 28572–28581.

178 E. Meza, R. E. Diaz and C. W. Li, *ACS Nano*, 2020, **14**, 2238–2247.

179 P. Vancsó, Z. I. Popov, J. Petö, T. Ollár, G. Dobrik, J. S. Pap, C. Hwang, P. B. Sorokin and L. Tapasztó, *ACS Energy Lett.*, 2019, **4**, 1947–1953.

180 Y. Liu, Y. Guo, Y. Liu, Z. Wei, K. Wang and Z. Shi, *Energy and Fuels*, 2023, **37**, 2608–2630.

181 H. Wang, T. Yang, J. Wang, Z. Zhou, Z. Pei and S. Zhao, *Chem*, 2024, **10**, 48–85.

182 A. W. Kahsay, K. B. Ibrahim, M. C. Tsai, M. K. Birhanu, S. A. Chala, W. N. Su and B. J. Hwang, *Catal. Letters*, 2019, **149**, 860–869.

183 S. Wang, T. Kou, J. B. Varley, S. A. Akhade, S. E. Weitzner, S. E. Baker, E. B. Duoss and Y. Li, *ACS Mater. Lett.*, 2021, **3**, 100–109.

184 J. Wang, M. G. Sandoval, M. Couillard, E. A. González, P. V. Jasen, A. Juan, A. Weck and E. A. Baranova, *ACS Sustain. Chem. Eng.*, , DOI:10.1021/ACSSUSCHEMENG.4C04086.

185 N. K. Singh, P. Kumar, A. Yadav and V. C. Srivastava, *J. Colloid Interface Sci.*, 2024, **654**, 895–905.

186 X. Li, L. Jiang, Y. Zhou and Q. Yu, *Langmuir*, , DOI:10.1021/ACS.LANGMUIR.4C01246.

187 H. A. B. Fonseca, L. G. Verga and J. L. F. Da Silva, *J. Phys. Chem. C*, 2023, **127**, 24118–24128.

188 D. Liu, Y. Liu and M. Li, *J. Phys. Chem. C*, 2020, **124**, 6145–6153.

189 C. L. Dong and L. Vayssieres, *Chem. – A Eur. J.*, 2018, **24**, 18356–18373.

190 K. T. Butler, D. W. Davies, H. Cartwright, O. Isayev and A. Walsh, *Nat. 2018 5597715*, 2018, **559**, 547–555.

191 A. Chandrasekaran, D. Kamal, R. Batra, C. Kim, L. Chen and R. Ramprasad, *npj Comput. Mater. 2019 51*, 2019, **5**, 1–7.

192 K. Zhao, X. Nie, H. Wang, S. Chen, X. Quan, H. Yu, W. Choi, G. Zhang, B. Kim and J. G. Chen, *Nat. Commun. 2020 111*, 2020, **11**, 1–10.

193 W. Fang, R. Lu, F. M. Li, C. He, D. Wu, K. Yue, Y. Mao, W. Guo, B. You, F. Song, T. Yao, Z. Wang and B. Y. Xia, *Angew. Chemie Int. Ed.*, 2024, **63**, e202319936.

194 P. Wang, H. Yang, C. Tang, Y. Wu, Y. Zheng, T. Cheng, K. Davey, X. Huang and S. Z. Qiao, *Nat. Commun. 2022 131*, 2022, **13**, 1–11.

195 Y. S. Cheng, X. P. Chu, M. Ling, N. Li, K. L. Wu, F. H. Wu, H. Li, G. Yuan and X. W. Wei, *Catal. Sci. Technol.*, 2019, **9**, 5668–5675.

196 H. Ning, X. Wang, W. Wang, Q. Mao, Z. Yang, Q. Zhao, Y. Song and M. Wu, *Carbon N. Y.*, 2019, **146**, 218–223.

197 D. Karapinar, N. T. Huan, N. Ranjbar Sahraie, J. Li, D. Wakerley, N. Touati, S. Zanna, D. Taverna, L. H. Galvão Tizei, A. Zitolo, F. Jaouen, V. Mougel and M. Fontecave, *Angew. Chemie Int. Ed.*, 2019, **58**, 15098–15103.

198 M. Wang, Z. Cai, B. Zhang, K. Yang, T. Shou, M. T. Bernards, P. Xie, Y. He and Y. Shi, *Energy and Fuels*, 2022, **36**, 5833–5842.
199 A. F. Pérez-Cadenas, C. H. Ros, S. Morales-Torres, M. Pérez-Cadenas, P. J. Kooyman, C. Moreno-Castilla and F. Kapteijn, *Carbon N. Y.*, 2013, **56**, 324–331.
200 S. Dongare, N. Singh and H. Bhunia, *J. CO2 Util.*, 2021, **44**, 101382.
201 J. Yuan, W. Y. Zhi, L. Liu, M. P. Yang, H. Wang and J. X. Lu, *Electrochim. Acta*, 2018, **282**, 694–701.
202 F. Yang, X. Mao, M. Ma, C. Jiang, P. Zhang, J. Wang, Q. Deng, Z. Zeng and S. Deng, *Carbon N. Y.*, 2020, **168**, 528–535.
203 X. Tan, C. Yu, C. Zhao, H. Huang, X. Yao, X. Han, W. Guo, S. Cui, H. Huang and J. Qiu, *ACS Appl. Mater. Interfaces*, 2019, **11**, 9904–9910.
204 X. F. Qiu, H. L. Zhu, J. R. Huang, P. Q. Liao and X. M. Chen, *J. Am. Chem. Soc.*, 2021, **143**, 7242–7246.
205 X. Ma, J. Tian, M. Wang, X. Jin, M. Shen and L. Zhang, *Catal. Sci. Technol.*, 2021, **11**, 6096–6102.
206 J. X. Wu, S. Z. Hou, X. Da Zhang, M. Xu, H. F. Yang, P. S. Cao and Z. Y. Gu, *Chem. Sci.*, 2019, **10**, 2199–2205.
207 Z. H. Zhao, K. Zheng, N. Y. Huang, H. L. Zhu, J. R. Huang, P. Q. Liao and X. M. Chen, *Chem. Commun.*, 2021, **57**, 12764–12767.
208 S. Juntrapirom, J. Santatiwongchai, A. Watwiangkham, S. Suthirakun, T. Butburee, K. Faungnawakij, P. Chakthranont, P. Hirunsit and B. Rungtaweevoranit, *Catal. Sci. Technol.*, 2021, **11**, 8065–8078.
209 K. Yao, Y. Xia, J. Li, N. Wang, J. Han, C. Gao, M. Han, G. Shen, Y. Liu, A. Seifitokaldani, X. Sun and H. Liang, *J. Mater. Chem. A*, 2020, **8**, 11117–11123.
210 Y. Zhao, C. Wang and G. G. Wallace, *J. Mater. Chem. A*, 2016, **4**, 10710–10718.
211 Y. Mi, S. Shen, X. Peng, H. Bao, X. Liu and J. Luo, *ChemElectroChem*, 2019, **6**, 2393–2397.
212 L. R. L. Ting, R. García-Muelas, A. J. Martín, F. L. P. Veenstra, S. T.-J. Chen, Y. Peng, E. Y. X. Per, S. Pablo-García, N. López, J. Pérez-Ramírez and B. S. Yeo, *Angew. Chemie*, 2020, **132**, 21258–21265.
213 X. Ren, X. Zhang, X. Cao and Q. Wang, *J. CO2 Util.*, 2020, **38**, 125–131.
214 J. Zeng, T. Rino, K. Bejtka, M. Castellino, A. Sacco, M. A. Farkhondehfal, A. Chiodoni, F. Drago and C. F. Pirri, *ChemSusChem*, 2020, **13**, 4128–4139.
215 M. Wang, Q. Zhang, Q. Xie, L. Wan, Y. Zhao, X. Zhang and J. Luo, *Nanoscale*, 2020, **12**, 17013–17019.
216 C. S. Chen, J. H. Wan and B. S. Yeo, *J. Phys. Chem. C*, 2015, **119**, 26875–26882.
217 D. Ren, Y. Deng, A. D. Handoko, C. S. Chen, S. Malkhandi and B. S. Yeo, *ACS Catal.*, 2015, **5**, 2814–2821.
218 A. D. Handoko, C. W. Ong, Y. Huang, Z. G. Lee, L. Lin, G. B. Panetti and B. S. Yeo, *J. Phys. Chem. C*, 2016, **120**, 20058–20067.
219 J. Kim, W. Choi, J. W. Park, C. Kim, M. Kim and H. Song, *J. Am. Chem. Soc.*, 2019, **141**, 6986–6994.
220 Y. Mun, S. Lee, A. Cho, S. Kim, J. W. Han and J. Lee, *Appl. Catal. B Environ.*, 2019, **246**, 82–88.
221 X. Guo, Y. Zhang, C. Deng, X. Li, Y. Xue, Y. M. Yan and K. Sun, *Chem. Commun.*, 2014, **51**, 1345–1348.
222 M. Serafini, F. Mariani, A. Fasolini, E. T. Brandi, E. Scavetta, F. Basile and D. Tonelli, *Adv. Funct. Mater.*, 2023, **33**, 2300345.
223 T. Gao, Y. Gu, M. Wu, Y. Liu, L. Yang, T. Han, S. Zhang, S. Li, W. Wei, W. Chen and X. Dong, *Energy and Fuels*, 2023, **37**, 19053–19062.
224 A. Saxena, S. Kapila, J. E. Medvedeva and M. Nath, *ACS Appl. Mater. Interfaces*, , DOI:10.1021/ACSAMI.3C00488/SUPPL_FILE/AM3C00488_SI_001.PDF.
225 L. J. Zhu, D. H. Si, F. X. Ma, M. J. Sun, T. Zhang and R. Cao, *ACS Catal.*, 2023, **13**, 5114–5121.
226 R. Dorakhan, I. Grigioni, B. H. Lee, P. Ou, J. Abed, C. O'Brien, A. Sedighian Rasouli, M. Plodinec, R. K. Miao, E. Shirzadi, J. Wicks, S. Park, G. Lee, J. Zhang, D. Sinton and E. H. Sargent, *Nat. Synth. 2023 25*, 2023, **2**, 448–457.
227 N. Liu, S. Bartling, A. Springer, C. Kubis, O. S. Bokareva, E. Salaya, J. Sun, Z. Zhang, S. Wohlrab, A. M. Abdel-Mageed, H. Q. Liang and R. Francke, *Adv. Mater.*, 2024, **36**, 2309526.
228 A. Loiudice, P. Lobaccaro, E. A. Kamali, T. Thao, B. H. Huang, J. W. Ager and R. Buonsanti, *Angew. Chemie Int. Ed.*, 2016, **55**, 5789–5792.
229 Y. Hori, A. Murata and R. Takahashi, *J. Chem. Soc. Faraday Trans. 1 Phys. Chem. Condens. Phases*, 1989, **85**, 2309–2326.
230 W. Zhang, C. Huang, Q. Xiao, L. Yu, L. Shuai, P. An, J. Zhang, M. Qiu, Z. Ren and Y. Yu, *J. Am. Chem. Soc.*, 2020, **142**, 11417–11427.
231 P. De Luna, R. Quintero-Bermudez, C.-T. Dinh, M. B. Ross, O. S. Bushuyev, P. Todorović, T. Regier, S. O. Kelley, P. Yang and E. H. Sargent, *Nat. Catal. 2018 12*, 2018, **1**, 103–110.
232 C. Dong, L. Cui, Y. Kong, C. Chen, H. Liu, Y. Zhang, W. Zhu and R. He, *J. Phys. Chem. C*, 2022, **126**, 102–109.
233 Y. Wu, P. Zhai, S. Cao, Z. Li, B. Zhang, Y. Zhang, X. Nie, L. Sun and J. Hou, *Adv. Energy Mater.*, 2020, **10**, 2002499.
234 F. Gao, S. Hu, X. Zhang, Y. Zheng, H. Wang, Z. Niu, P. Yang, R. Bao, T. Ma, Z. Dang, Y. Guan, X. Zheng, X. Zheng, J. Zhu, M. Gao and S. Yu, *Angew. Chemie*, 2020, **132**, 8784–8790.
235 R. He, A. Zhang, Y. Ding, T. Kong, Q. Xiao, H. Li, Y. Liu and J. Zeng, *Adv. Mater.*, 2018, **30**, 1705872.
236 Y. H. Li, L. Cheng, P. F. Liu, L. Zhang, M. Y. Zu, C. W. Wang, Y. H. Jin, X. M. Cao, H. G. Yang and C. Li, *ChemSusChem*, 2018, **11**, 1421–1425.
237 L. Cheng, Y. Li, A. Chen, Y. Zhu and C. Li, *Chem. Commun.*, 2020, **56**, 563–566.
238 B. Qin, Y. Li, H. Wang, G. Yang, Y. Cao, H. Yu, Q. Zhang, H. Liang and F. Peng, *Nano Energy*, 2019, **60**, 43–51.
239 Y. Wang, R. Du, Z. Li, H. Song, Z. Chao, D. Zu, D. Chong, N. Gao and C. Li, *Ceram. Int.*, 2021, **47**, 28321–28327.
240 L. Cheng, Y. Wang, Y. Li, Y. Shen, Y. Zhen, Z. Xing, L. Lin, A. Chen, Y. Zhu and C. Li, *ChemCatChem*, 2021, **13**, 1161–1164.
241 R. He, X. Yuan, P. Shao, T. Duan and W. Zhu, *Small*, 2019, **15**, 1904882.
242 A. Zhang, R. He, H. Li, Y. Chen, T. Kong, K. Li, H. Ju, J. Zhu, W. Zhu and J. Zeng, *Angew. Chemie - Int. Ed.*, 2018, **57**, 10954–

10958.

243 X. Zheng, P. De Luna, F. Pelayo García De Arquer, X. Du, P. Yang, E. H. Sargent, B. Zhang, N. Becknell, M. B. Ross, Y. Li, M. N. Banis, Y. Li, M. Liu, O. Voznyy, C. T. Dinh, T. Zhuang, P. Stadler and Y. Cui, *Joule*, 2017, **1**, 794–805.

244 Z. Chen, X. Zhang, M. Jiao, K. Mou, X. Zhang and L. Liu, *Adv. Energy Mater.*, 2020, **10**, 1903664.

245 F. Li, L. Chen, M. Xue, T. Williams, Y. Zhang, D. R. MacFarlane and J. Zhang, *Nano Energy*, 2017, **31**, 270–277.

246 J. He, X. Liu, H. Liu, Z. Zhao, Y. Ding and J. Luo, *J. Catal.*, 2018, **364**, 125–130.

247 H. Cheng, S. Liu, J. Zhang, T. Zhou, N. Zhang, X. S. Zheng, W. Chu, Z. Hu, C. Wu and Y. Xie, *Nano Lett.*, 2020, **20**, 6097–6103.

248 J. Xu, S. Lai, M. Hu, S. Ge, R. Xie, F. Li, D. Hua, H. Xu, H. Zhou, R. Wu, J. Fu, Y. Qiu, J. He, C. Li, H. Liu, Y. Liu, J. Sun, X. Liu and J. Luo, *Small Methods*, 2020, **4**, 2000567.

249 S. Q. Liu, M. R. Gao, R. F. Feng, L. Gong, H. Zeng and J. L. Luo, *ACS Catal.*, 2021, **11**, 7604–7612.

250 Y. Zhang, F. Li, X. Zhang, T. Williams, C. D. Easton, A. M. Bond and J. Zhang, *J. Mater. Chem. A*, 2018, **6**, 4714–4720.

251 X. Yang, P. Deng, D. Liu, S. Zhao, D. Li, H. Wu, Y. Ma, B. Y. Xia, M. Li, C. Xiao and S. Ding, *J. Mater. Chem. A*, 2020, **8**, 2472–2480.

252 X. Shao and Y. Liu, *J. Electrochem. Soc.*, 2022, **169**, 026505.

253 J. Wang, J. Mao, X. Zheng, Y. Zhou and Q. Xu, *Appl. Surf. Sci.*, 2021, **562**, 150197.

254 C. Li, Z. Liu, X. Zhou, L. Zhang, Z. Fu, Y. Wu, X. M. Lv, G. Zheng and H. Chen, *Energy Environ. Sci.*, 2023, **16**, 3885–3898.

255 Y. Li, J. Chen, S. Chen, T. Lu, X. Liao, T. Zhao, F. Cheng and H. Wang, *Appl. Catal. B Environ. Energy*, 2024, **349**, 123874.

256 M. Asadi, B. Kumar, A. Behranginia, B. A. Rosen, A. Baskin, N. Repnin, D. Pisasale, P. Phillips, W. Zhu, R. Haasch, R. F. Klie, P. Král, J. Abiade and A. Salehi-Khojin, *Nat. Commun. 2014 51*, 2014, **5**, 1–8.

257 F. Li, S. F. Zhao, L. Chen, A. Khan, D. R. MacFarlane and J. Zhang, *Energy Environ. Sci.*, 2016, **9**, 216–223.

258 K. Lv, W. Suo, M. Shao, Y. Zhu, X. Wang, J. Feng and M. Fang, *Nano Energy*, 2019, **63**, 103834.

259 N. Hussain, M. A. Abdelkareem, H. Alawadhi, K. Elsaid and A. G. Olabi, *Chem. Eng. Sci.*, 2022, **258**, 117757.

260 N. Hussain, M. A. Abdelkareem, H. Alawadhi, S. Begum, K. Elsaid and A. G. Olabi, *J. Power Sources*, 2022, **549**, 232128.

261 H. Li, X. Liu, S. Chen, D. Yang, Q. Zhang, L. Song, H. Xiao, Q. Zhang, L. Gu and X. Wang, *Adv. Energy Mater.*, 2019, **9**, 1900072.

262 G. Shi, L. Yu, X. Ba, X. Zhang, J. Zhou and Y. Yu, *Dalt. Trans.*, 2017, **46**, 10569–10577.

263 P. Abbasi, M. Asadi, C. Liu, S. Sharifi-Asl, B. Sayahpour, A. Behranginia, P. Zapol, R. Shahbazian-Yassar, L. A. Curtiss and A. Salehi-Khojin, *ACS Nano*, 2017, **11**, 453–460.

264 N. Hussain, M. A. Abdelkareem, H. Alawadhi, A. H. Alami and K. Elsaid, *Appl. Phys. A Mater. Sci. Process.*, 2022, **128**, 1–11.

265 K. Lv, C. Teng, M. Shi, Y. Yuan, Y. Zhu, J. Wang, Z. Kong, X. Lu and Y. Zhu, *Adv. Funct. Mater.*, 2018, **28**, 1802339.

266 J. Xu, X. Li, W. Liu, Y. Sun, Z. Ju, T. Yao, C. Wang, H. Ju, J. Zhu, S. Wei and Y. Xie, *Angew. Chemie Int. Ed.*, 2017, **56**, 9121–9125.

267 X. Yuan, Y. Luo, B. Zhang, C. Dong, J. Lei, F. Yi, T. Duan, W. Zhu and R. He, *Chem. Commun.*, 2020, **56**, 4212–4215.

268 A. Zhang, Y. Liang, H. Li, X. Zhao, Y. Chen, B. Zhang, W. Zhu and J. Zeng, *Nano Lett.*, 2019, **19**, 6547–6553.

269 L. P. Chi, Z. Z. Niu, X. L. Zhang, P. P. Yang, J. Liao, F. Y. Gao, Z. Z. Wu, K. Bin Tang and M. R. Gao, *Nat. Commun. 2021 121*, 2021, **12**, 1–9.

270 J. Feng, H. Gao, J. Feng, L. Liu, S. Zeng, H. Dong, Y. Bai, L. Liu and X. Zhang, *ChemCatChem*, 2020, **12**, 926–931.

271 W. Ma, S. Xie, X. G. Zhang, F. Sun, J. Kang, Z. Jiang, Q. Zhang, D. Y. Wu and Y. Wang, *Nat. Commun. 2019 101*, 2019, **10**, 1–10.

272 C. T. Altaf, T. O. Colak, E. Karagoz, J. Wang, Y. Liu, Y. Chen, M. Liu, U. Unal, N. D. Sankir and M. Sankir, *ACS Omega*, , DOI:10.1021/ACSOMEGA.4C00018.

273 J. E. Pander, J. W. J. Lum and B. S. Yeo, *J. Mater. Chem. A*, 2019, **7**, 4093–4101.

274 Z. Zhang, C. Liu, J. T. Brosnahan, H. Zhou, W. Xu and S. Zhang, *J. Mater. Chem. A*, 2019, **7**, 23775–23780.

275 J. Z. Zhen, J. X. Liu, T. Y. Chen, F. Shi, Y. N. Dai, B. Yang, Y. F. Li, X. Wang, T. G. Nong, Y. Q. Hu and J. Shi, *J. Alloys Compd.*, 2019, **771**, 994–999.

276 C. Li, G. Shen, R. Zhang, D. Wu, C. Zou, T. Ling, H. Liu, C. Dong and X. W. Du, *J. Mater. Chem. A*, 2019, **7**, 1418–1423.

277 Y. Song, Y. Wang, J. Shao, K. Ye, Q. Wang and G. Wang, *ACS Appl. Mater. Interfaces*, , DOI:10.1021/ACSAMI.1C15669/SUPPL_FILE/AM1C15669_SI_001.PDF.

278 H. il Nam, K. Ryeol Park, Y. W. Choi, H. ji Sim, K. Yong Sohn and D. H. Lim, *Appl. Surf. Sci.*, 2023, **612**, 155646.

279 A. Aljabour, H. Coskun, X. Zheng, M. G. Kibria, M. Strobel, S. Hild, M. Kehrer, D. Stifter, E. H. Sargent and P. Stadler, *ACS Catal.*, 2020, **10**, 66–72.

280 C. Simon, J. Zander, T. Kottakkat, M. Weiss, J. Timm, C. Roth and R. Marschall, *ACS Appl. Energy Mater.*, 2021, **4**, 8702–8708.

281 S. Zhao, S. Guo, C. Zhu, J. Gao, H. Li, H. Huang, Y. Liu and Z. Kang, *RSC Adv.*, 2017, **7**, 1376–1381.

282 S. Piontek, K. Junge Puring, D. Siegmund, M. Smialkowski, I. Sinev, D. Tetzlaff, B. Roldan Cuenya and U. P. Apfel, *Chem. Sci.*, 2019, **10**, 1075–1081.

283 D. Tetzlaff, K. Pellumbi, K. junge Puring, D. Siegmund, W. S. K. Polet, M. P. Checinski and U. P. Apfel, *ChemElectroChem*, 2021, **8**, 3161–3167.

284 K. Pellumbi, M. Smialkowski, D. Siegmund and U. P. Apfel, *Chem. – A Eur. J.*, 2020, **26**, 9938–9944.

285 T. J. Wang, W. S. Fang, Y. M. Liu, F. M. Li, P. Chen and Y. Chen, *J. Energy Chem.*, 2022, **70**, 407–413.

286 C. Xia, X. Wang, C. He, R. Qi, D. Zhu, R. Lu, F. M. Li, Y. Chen, S. Chen, B. You, T. Yao, W. Guo, F. Song, Z. Wang and B. Y. Xia, *J. Am. Chem. Soc.*, 2024, 146 (29), 20530–20538

287 J. Qiao, Y. Liu, F. Hong and J. Zhang, *Chem. Soc. Rev.*, 2013, **43**, 631–675.

288 D. Du, R. Lan, J. Humphreys and S. Tao, *J. Appl. Electrochem. 2017 476*, 2017, **47**, 661–678.

289 B.-Q. Miao, W.-S. Fang, B. Sun, F.-M. Li, X.-C. Wang, B.-Y. Xia

View Article Online
DOI: 10.1039/D4YA00302K

and Y. Chen, *Chinese J. Struct. Chem.*, 2023, **42**, 100095.

290 S. Verma, B. Kim, H. R. M. Jhong, S. Ma and P. J. A. Kenis, *ChemSusChem*, 2016, **9**, 1972–1979.

291 R. Lin, J. Guo, X. Li, P. Patel and A. Seifitokaldani, *Catal. 2020, Vol. 10, Page 473*, 2020, **10**, 473.

292 Y. C. Li, D. Zhou, Z. Yan, R. H. Gonçalves, D. A. Salvatore, C. P. Berlinguette and T. E. Mallouk, *ACS Energy Lett.*, 2016, **1**, 1149–1153.

293 S. A. Al-Tamreh, M. H. Ibrahim, M. H. El-Naas, J. Vaes, D. Pant, A. Benamor and A. Amhamed, *ChemElectroChem*, 2021, **8**, 3207–3220.

294 M. Zeng, W. Fang, Y. Cen, X. Zhang, Y. Hu and B. Y. Xia, *Angew. Chemie*, 2024, **136**, e202404574.

295 H. Veldhuizen, M. Abdinejad, P. J. Gilissen, J. Albertsma, T. Burdyny, F. D. Tichelaar, S. van der Zwaag and M. A. van der Veen, *ACS Appl. Mater. Interfaces* , 2024, **16**, 34010–34019.

296 O. G. Sánchez, Y. Y. Birdja, M. Bulut, J. Vaes, T. Breugelmans and D. Pant, *Curr. Opin. Green Sustain. Chem.*, 2019, **16**, 47–56.

297

298 D. Ewis, M. Arsalan, M. Khaled, D. Pant, M. M. Ba-Abbad, A. Amhamed and M. H. El-Naas, *Sep. Purif. Technol.*, 2023, **316**, 123811.

299 H. Yang, J. J. Kaczur, S. D. Sajjad and R. I. Masel, *J. CO2 Util.*, 2020, **42**, 101349.

300 M. Jouny, W. Luc and F. Jiao, *Ind. Eng. Chem. Res.*, 2018, **57**, 2165–2177.

301 A. J. Martín, G. O. Larrazábal and J. Pérez-Ramírez, *Green Chem.*, 2015, **17**, 5114–5130.

302 F. Proietto, U. Patel, A. Galia and O. Scialdone, *Electrochim. Acta*, 2021, **389**, 138753.

303 W. Fang, W. Guo, R. Lu, Y. Yan, X. Liu, D. Wu, F. M. Li, Y. Zhou, C. He, C. Xia, H. Niu, S. Wang, Y. Liu, Y. Mao, C. Zhang, B. You, Y. Pang, L. Duan, X. Yang, F. Song, T. Zhai, G. Wang, X. Guo, B. Tan, T. Yao, Z. Wang and B. Y. Xia, *Nat. 2024 6267997*, 2024, **626**, 86–91.

View Article Online
DOI: 10.1039/D4YA00302K

Data Availability Statement

No primary research results, software or code have been included and no new data were generated or analysed as part of this review.

Dr. Bidhan Chandra Ruidas
Department of Chemical Engineering
Birla Institute of Technology, Mesra
Ranchi-835215, India
+91-7589216760
bidhanruidas@gmail.com